2015

Application of acoustic emission monitoring to pipeline fracture tests

Turbadrakh Chuluunbat
University of Wollongong

APPLICATION OF ACOUSTIC EMISSION MONITORING TO PIPELINE FRACTURE TESTS

A thesis submitted in fulfilment of the requirement for the award of the degree of

DOCTOR OF PHILOSOPHY

From

UNIVERSITY OF WOLLONGONG

By

Turbadrakh Chuluunbat

B.Eng. (Mechanical Engineering)
M.Eng. (Engineering Science)

School of Mechanical, Materials and Mechatronic Engineering,
University of Wollongong, Australia

2015

Thesis certification

I, Turbadrakh Chuluunbat, declare that this thesis, submitted in fulfilment of the requirements for the award of Doctor of Philosophy, at the School of Mechanical, Materials and Mechatronic Engineering, University of Wollongong, is wholly my own work unless otherwise referenced or acknowledged. The document has not been submitted for qualification at any other academic institutions.

Turbadrakh Chuluunbat

August 2015

TABLE OF CONTENTS

ABSTRACT

Maximization of benefits in the oil and gas transportation industries requires an increase in the size and operating pressure of the pipeline, which in turn requires an increase in the strength of line pipe steel. To ensure reliable operation, public safety, and environmental protection, the design of pipelines must include strategies for controlling fractures. Identifying defect(s) where crack initiation is possible and predicting the crack propagation are of great importance when considering fracture control of pipelines.The current research is aimed at developing an improved method using the acoustic emission (AE) technique for determining fracture initiation and propagation in the line pipe steel during Charpy V-Notch (CVN) impact test and single edge-notched tension (SENT) test.

SENT tests on X70 and X80 line pipe steels were conducted, augmented with the AE measurements. It was found that the AE activity started before the yield point due to stress concentration at the crack tip and increased suddenly before the peak load was reached due to fracture initiation. Towards the end of the test, the AE hit density increased again. With an increase in the strain rate and a decrease in the test temperature, AE activity increased during the SENT test. It was found that the fracture initiation resulted in a ‘burst-type’ AE signal with a 65-75 dB amplitude and a 300-350 kHz average frequency, prior to the peak load point on the load-displacement curve. It was also found that the AE count rate increased as the crack growth rate increased and the AE average frequency decreased with the void size.

CVN tests on X70 line pipe steels were conducted at various temperatures. Tests with different specimen thicknesses were also performed at room temperature. The AE measurement technique

was applied to all tests. It was found that the temperature and sample thickness affected the fracture mode (ductile or brittle) and the relative magnitude of the AE signals. The AE average frequency increased as the temperature decreased, while the AE average frequency decreased as the specimen thickness was reduced.There was a strong burst-type AE signal in a short time span between the yield point and the peak load point on the load-displacement curve, which is believed to be responsible for fracture initiation.

Finite Element Modelling (FEM) simulations confirmed that the fracture was initiated within a relatively short time period between the yield point and the peak load point on the load-displacement curve for both CVN test and SENT test, which is in good agreement with the observations from the AE monitoring.

The distinction between fracture initiation energy and fracture propagation energy is crucial in pipeline fracture control research. From the present study, it was found that using the peak load point to separate the two energy components is not accurate. The AE analysis conducted in the present thesis showed strong evidence of AE hits before the peak load, corresponding to the fracture initiation. Therefore, this thesis recommends that AE measurement be used to identify the fracture initiation, rather than the peak load point, in future pipeline research.

ACKNOWLEDGEMENTS

I would like to thank all the people who have made this thesis possible. First and foremost, I would like to express my deepest sense of gratitude to my supervisors Associate Professor Cheng Lu and Professor Kiet Tieu. This investigation would not have been possible without their guidance and contribution.

My sincere and special thanks go to Dr. Andrii Kostryzhev for his unlimited support and valuable advice during the experimental work. Also, I would like to thank Dr. Ajit Godbole and Dr. Lihong Su for their suggestions in revising the manuscript.

This work was carried out at the School of Mechanical, Materials and Mechatronics School, Engineering, Faculty of Engineering, University of Wollongong. I would like to thank all my colleagues and fellow PhD students for their precious advice and help during the research.

The funding and in-kind support from the Energy Pipeline Cooperative Research Centre (EPCRC), Australia, is gratefully acknowledged. Sincere thanks to the Electron Microscopy Centre at the University of Wollongong for providing access to the JEOL JSM-6490LA scanning electron microscope.

Finally, my deepest regards to my Parents for their unconditional love and support, and to my wife S. Enkhzaya for her patience, support and understanding, and to my lovely kids, T. Bilegsaikhan and T. Bilegjargal. Without their support and love I could not have completed this research. I dedicate this thesis to them.

LIST OF FIGURES

LIST OF TABLES

1 INTRODUCTION

1.1 Overview

The maximization of benefits in the oil and gas transportation industries requires an increase in the size and operating pressure of the pipeline, which in turn requires an increase in the strength of the pipeline steel. A gas pipeline failure can have a catastrophic impact on the environment. It may cause public injury and lead to a high repair cost [1, 2] . Pipeline failure may result from a number of causes such as local defects in the pipe wall and plastic deformation damage due to ground movement. Pipelines can be subjected to severe deformation during installation and operation, from biaxial load originating from longitudinal strain and internal pressure. The problem can be potentially accentuated if conditions are such that the pipeline metal attains low temperature while it is subjected to high stress/strain. This calls for a study of the effect of the strain rate and low temperature on the properties of pipeline steel. Therefore, a better understanding of the modes of pipeline fracture (ductile or brittle) is needed to prevent or control fracture initiation and propagation. Laboratory-scale experiments carried out on specially designed specimens can potentially yield useful results in this respect.

One such example is a single-edge-notch specimen that can be subjected to a tension test. The notch in the specimen can ‘simulate’ a crack in a full-scale pipeline by creating a similar stress field in the vicinity of the crack tip. Another important example is a Charpy V-notch specimen that is used to measure fracture energy using the dynamic impact test. The pipeline steel should be able to dissipate enough energy to arrest a crack if it is initiated. This criterion can be assessed

by a CVN test. The main concern in fracture propagation control is the minimum value of pipeline steel toughness that would arrest ductile fracture [3]. This minimum toughness can be determined from a CVN test.

Predicting the presence of defects in the line pipe steel, and identifying crack initiation and propagation, are of great importance in fracture control of pipelines, especially if different failure modes (ductile or brittle) are involved [4]. To fully explain pipeline failure, research is needed to develop a better understanding of the mechanical properties and fracture behavior in line pipe steels. The current research is aimed at identifying fracture initiation points using CVN and SENT tests. Traditionally, it is assumed that fractures initiate at the point of maximum load during the tests [5]. However, FEM simulations have shown that fractures can initiate before or after the load has reached its maximum value [6] . To investigate this phenomenon, the ductile fracture initiation point must be detected within a relatively short time period between the yield of the sample during, and before or just after the maximum load point. This introduces new complications into the standard experimental procedure.

A method well suited to investigating the line pipe steel fracture initiation and propagation is the acoustic emission (AE) monitoring technique [7, 8]. Fracture phenomena such as crack initiation and propagation lead to the emission of high-frequency acoustic waves [9, 10] which can be detected and analysed by an AE monitoring system.

The word ‘acoustic’ is derived from the Greek word akoustikos, which has to do with ‘hearing’ [7]. Acoustic emission testing is recognized as a non-destructive testing (NDT) method, and is

commonly used to detect and locate the faults in mechanically loaded structures and components. 'Acoustic emission' refers to the generation of transient stress/ displacement waves, following rapid release of energy from localized sources such as crack initiation sites, and, fracture propagation and dislocation in metals [8, 11]. Elastic energy is transmitted through the material in the form of transient elastic waves that can be detected by sensors on the surface of the specimen. The sensor converts the elastic wave signal into an electrical signal which is then processed and analyzed by special hardware and software. The AE technique can provide comprehensive information on the initiation of a discontinuity (flaw) in a stressed specimen [12].

The AE method is an effective tool for detecting crack initiation during static and dynamic testing. However, most of the above studies report only qualitative analyses of the AE parameters and their correlation to the fracture parameters. To date, there is no general theory as to what frequency ranges could be attributed to a given fracture mechanism. This is due to the variation in fracture mechanisms with different material and test types. Usually, the AE technique is used to detect only the onset of fracture. This is not a trivial task because the AE signal can be adversely influenced by unwanted 'noise'. In addition, AE signal analysis can be significantly complicated by incorrect experimental settings. Although a substantial amount of qualitative research has been published, there is need for experimental validation. Also, quantitative dependences of the AE parameters on the fracture parameters (e.g. brittle or ductile mode of propagation, crack growth rate, etc.) are not completely understood. Consequently, no recommendation exists to relate the AE parameters to the fracture parameters.

1.1.1 Thesis aims and objectives

The primary objective of this project was to gain in–depth understanding of the mechanical properties and fracture behavior in line pipe steel. It is believed that this work will provide a more detailed understanding of the fracture characteristics of line pipe steel and in turn help develop a new pipeline fracture control model. Identifying defects where crack initiation is possible and predicting crack propagation are of great importance in pipeline fracture control. Therefore, the current research is aimed at developing a method for identifying fracture initiation and propagation in the line pipe steels. It is believed that a combination of FEM simulation and experimental work using the AE monitoring technique can lead to a better understanding of the properties and fracture mechanisms in the line pipe steel.

The main objectives of this study are:

- Establishing qualitative and quantitative relationships between the line pipe steel fracture and the AE parameters:
- Understanding the influence of loading conditions on the AE parameters;
- Investigation of the possibility to use the AE technique for the detection of fracture initiation;
- The development of dependence between the AE parameters and the crack growth parameters;
- Quantitative correlation of the AE parameters to fracture modes;
- Investigating fracture initiation and propagation using FEM simulations;

During mechanical testing, the fracture process was observed using a high-speed camera in conjunction with the digital image correlation (DIC) technique. Variations in AE parameters were analyzed using the 'Average Hit' feature and Wave Form and Power Spectrum methodologies. These were correlated to the load-displacement and load-time curves obtained during testing.

1.1.2 Thesis outline

This thesis consists of 7 chapters. Chapter 1 provides an introduction to the pipeline fracture mechanics and the AE technique. The thesis aims, objectives and outline are described.

Chapter 2 reviews the available literatures in six parts. The first part contains a review of the available literature on the pipeline fracture control. The second part contains an account of reported pipeline fracture tests such as the CVN and SENT tests. The principles of AE monitoring, AE wave modes, AE signal analysis, AE sources and the possible relationship between the AE parameters and the fracture parameters are presented in the next two parts. Part five reviews the AE monitoring of mechanical tests including the tension test and the impact test. An AE study on pipeline steel is also added. Part six is a summary of the literature review and the gaps in current knowledge.

Chapter 3 presents the experimental facilities/equipment used in this study: CVN test and SENT test machines, AE instrumentation, a high-speed camera, a scanning electron microscope and the

DIC technique. The finite element (FE) software used to investigate fracture phenomenon of line pipe steel is also introduced.

Chapter 4 describes the application of the AE monitoring technique to SENT tests carried out on the line pipe steel specimens. Information on the loading conditions, steel grade, specimen type and the effect of fracture mode on AE is presented. The identification of fracture initiation and the dependence of the AE parameters on crack growth are analyzed and discussed.

In Chapter 5, the application of AE monitoring to CVN impact testing is presented. The effects of temperature and specimen thickness on the fracture initiation and propagation are studied, using instrumented CVN testing of the line pipe steel. The load-time and load-deflection curves are correlated to AE signal characteristics and the effects of frequency distribution on fracture behavior of line pipe steel is analyzed and discussed.

In Chapter 6, FEM simulations of the CVN and SENT tests on X70 line pipe steel are described. Detailed information on the crack initiation and propagation is obtained from the FEM simulation results. Comparisons between the experimental results and the simulations are presented and analyzed.

Chapter 7 summarizes the main findings of this research. Important conclusions are presented, along with suggestions and recommendations for future research.

2 LITERATURE REVIEW

This chapter presents background information on the pipeline fracture, the principles of AE monitoring and the use of an acoustic emission to investigate fracture mechanics. This review also examines the difficulties related to the application of the AE technique to the pipeline fracture.

2.1 Pipeline fracture control

A gas pipeline failure can have a catastrophic impact on the environment in the vicinity of the failure. It may cause public injury and lead to a high repair cost. Pipeline failure may result from a number of causes such as local defects in the pipe wall and plastic deformation damage due to ground movement [1]. Failures of high-pressure fluid pipelines have been reported ever since natural gas transportation in long-distance pipelines began. The first cases of brittle running fracture were reported in North America and Europe in the 1950s [3]. Several long running fracture accidents resulted in the establishment of fundamental pipeline research in the 1960s and 1970s, aiming to investigate new tools to prevent fracture propagation. These investigations led to an increased understanding of fracture control.

Sustainable growth in the oil and gas transportation industries requires an increase in the diameter/ length and operating pressure of the pipeline, which in turn requires an increase in the strength of the line pipe steel. To ensure reliable operation, public safety, and environmental protection, the design of pipelines must include strategies for fracture control. In the pipeline

industry, prevention of pipeline steel fracture is a significant issue that is approached with a view to control fracture initiation and fracture propagation [13, 14]. The fracture initiation may occur due to a manufacturing defect, design error, or mechanical damage in the form of a notch, crack, dent, or gouge, or due to corrosion (e.g. hydrogen-induced cracks and sulfide stress corrosion cracks). Major factors that influence fracture initiation are: the size and orientation of flaws, pipe diameter and wall thickness, toughness, temperature, and fluid pressure [15].

When a defect reaches a critical length, or when a certain stress level is reached, the fracture will start to propagate. Once the fracture is initiated, it may propagate for long distances in either brittle or ductile modes. In theory, a brittle fracture could propagate indefinitely unless arrested by mechanical crack arrestors, while a ductile fracture could be self-arresting. Fig.2.1 shows typical patterns of the pipeline fracture propagation. Fracture propagation in pipelines can be divided into two types: brittle fracture for low-toughness steel and ductile fracture for high-toughness steel [16].

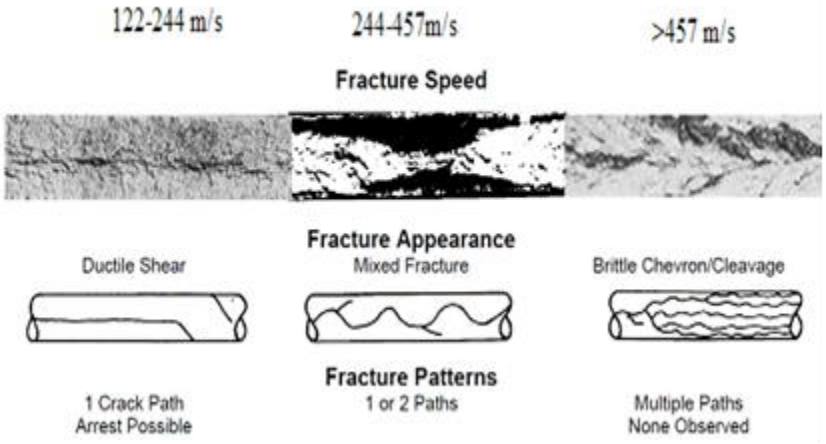

Fig.2.1 Fracture Patterns [16].

The fracture control philosophy of any pipelines conveying a pressurized gas considers two aspects [17] as shown in Fig.2.2: (1) Fracture initiation control and, (2) Fracture propagation control. The fracture initiation control can be achieved by providing sufficient fracture initiation resistance, while the fracture propagation control can be achieved by ensuring sufficient fracture propagation resistance such that a running fracture is arrested as quickly as possible, generally within one pipe length [3, 18]:

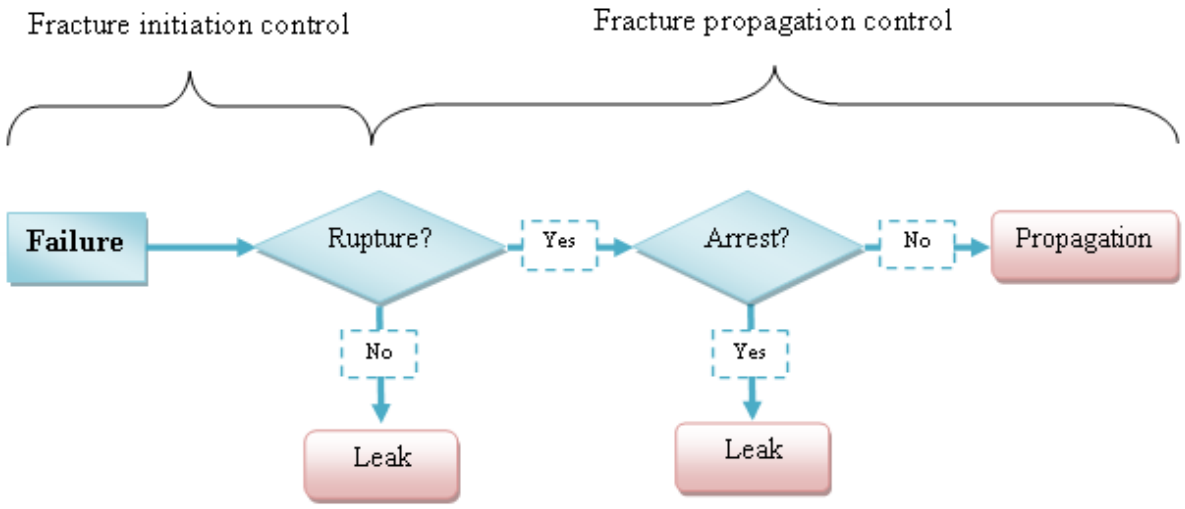

Fig.2.2 Fracture control plan of gas pipelines [17].

If the toughness required to arrest a running fracture cannot be attained, it may become necessary to use crack arrestors [19]. The crack arrestors in the form of clock springs or a thicker wall pipe section are usually installed to ensure that a propagating fracture will stop within three pipe spools. A Crack arrestor is schematically illustrated in Fig.2.3.

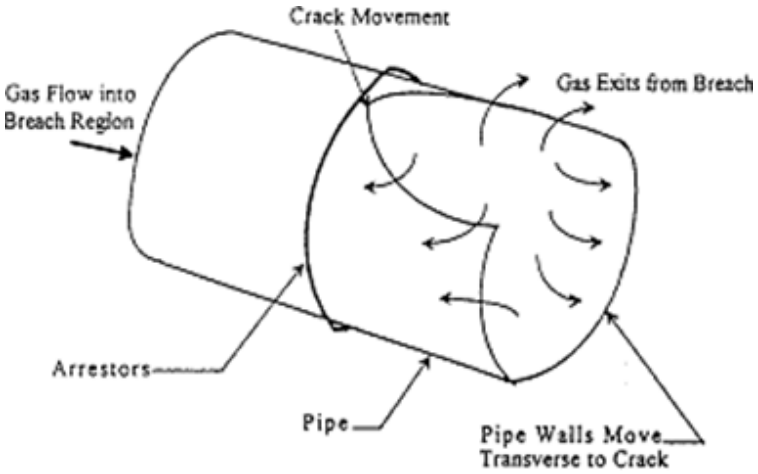

Fig.2.3 General scheme of crack arrestor [19].

2.1.1 Brittle fracture propagation

There have been several accidents due to long and unstable brittle fracture propagation reported in North America and Europe since the 1950s [20]. In 1953, an event involved a brittle fracture that propagated up to 16 km [21]. There is a large difference between the decompression wave velocity in natural gas (380–440 m/s) and the brittle fracture velocity in the pipe material (450–900 m/s). This means that once a brittle fracture is initiated, it will propagate indefinitely through the pipe material due to the unchanged pressure at the fracture tip [3, 4]. Fig.2.4 shows an example of brittle fracture propagation in a pipeline [22].

Fig.2.4 Brittle fracture propagation [22].

In 1958, the Pipeline Research Committee was formulated with a view to find ways to prevent brittle fracture failures in pipelines [3, 23].

Since the 1960s, extensive research has been carried out to prevent and control brittle fracture failures in pipelines. It was found that a sufficient condition for brittle fracture propagation control is controlling the ductile-to-brittle transition temperature (DBTT) of the pipeline material [24, 25]. DBTT is the temperature above which the fracture propagates in a brittle mode, while below the DBTT the fracture propagates in a ductile mode. If the pipeline operating temperature is below the DBTT, the brittle fracture occurs via the elastic mechanism (cleavage) with a high fracture propagation speed (~450-900 m/s) [16] . On the other hand, if the pipeline operating temperature is above the DBTT, the ductile fracture occurs via an elasto-plastic (shear) mechanism with a much slower fracture speed (~200 m/s) while also absorbing more energy [21, 26]. The drop weight tear test (DWTT) was developed in the 1960s and widely used to predict the DBTT of line pipe steel. The CVN impact test can also be used to determine the DBTT.

However, a correction factor must be applied to the DBTT predicted by a CVN test to estimate the DBTT of a full-scale pipe test. Since the 1970s, the pipeline industry has been generally successful in preventing brittle fracture propagation.

2.1.2 Ductile fracture propagation

A propagating ductile fracture is another possible cause of pipeline failures [27]. Although the propagation speed of a ductile fracture is relatively low (about 60-250 m/s) [2, 28], a ductile fracture can still travel for a long distance (several hundred meters) if the gas decompression wave speed drops below the ductile fracture propagation speed under the right operating conditions [1, 2].

Whether a ductile fracture can propagate or not is largely dependent on the relative magnitudes of the fracture speed of the pipe material and the speed of the decompression wave in the gas/fluid that is transported by the pipe. The speed of pipe material fracture is a function of the pipe geometry, material properties and the stress at the crack tip [16, 29]. Fig.2.5 shows the effect of ductile fracture propagation in a pipeline [30]. In order to prevent such fractures, the line pipe steel must have sufficient toughness and strength to ensure that the pipeline fracture speed is always lower than the gas decompression wave speed during the entire fracture propagation process. The crucial parameter in the ductile fracture propagation control is the toughness of the line pipe steel, which can be determined experimentally by a CVN test [18, 31].

Fig.2.5 A typical running ductile fracture [30].

The Battelle Two-Curve method (BTCM) is a semi-empirical analytical method that was devised to predict the minimum toughness required to arrest a running ductile fracture [20, 32]. The BTCM has been widely used for ductile fracture control in pipelines. The model consists of the superposition of two curves: the gas decompression wave speed curve and the fracture propagation speed curve [33, 34]. Each is plotted as a function of pressure. Fig.2.6 shows a single gas decompression wave speed curve, and three fracture speed curves corresponding to three values of pipeline material toughness. If the gas decompression wave speed curve intersects a fracture speed curve (as in the case of Curve 1), the fracture and the gas decompression wave that is driving the fracture propagation will travel together at the same speed. This implies that the fracture velocity will not decrease and the fracture cannot self-arrest. In principle, this fracture will propagate indefinitely. If, on the other hand, there is no intersection (as in the case of Curve 3), the decompression wave speed is higher than the fracture speed for all pressures. As the gas pressure wave outruns the fracture, it leaves a reduced pressure in its wake until the pressure at the crack tip finally falls sufficiently to cause the fracture to arrest.

The limiting condition between fracture arrest and fracture propagation is thus represented by the tangency between the gas decompression wave speed curve and the fracture propagation speed curve (Curve 2). Since the fracture curve is related to the toughness of the line pipe steel, the toughness corresponding to Curve 2 gives us the minimum material toughness required to arrest a running ductile fracture. According to this method, to prevent a running ductile fracture, the gas decompression wave speed must be greater than the fracture propagation speed.

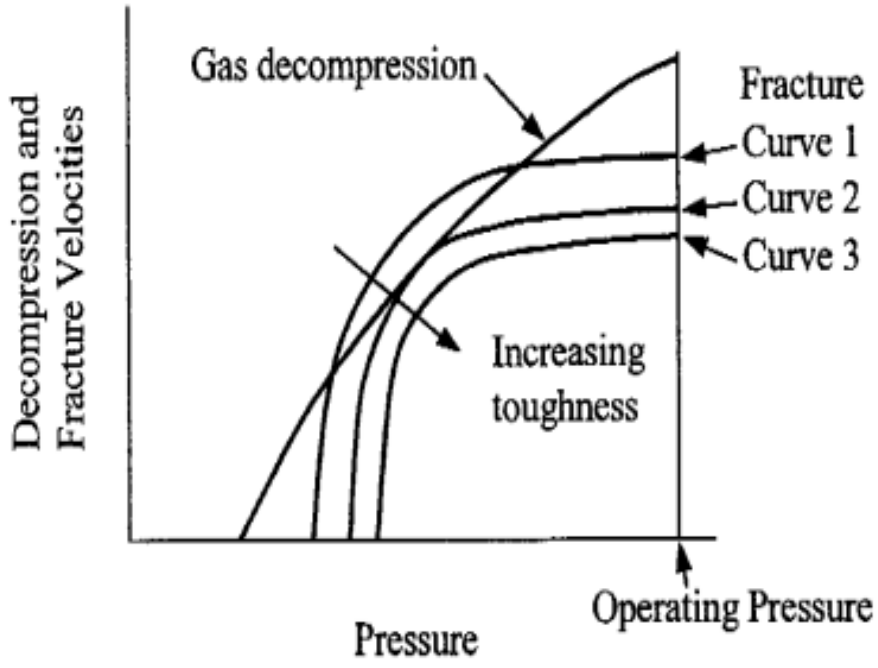

Fig.2.6 Schematic of Battelle Two Curve Method [33].

2.2 Pipeline fracture tests

2.2.1 Charpy V-notch impact test

The Charpy V-Notch (CVN) test is used to determine the toughness (i.e. the energy absorbed by the specimen during fracture) of the line pipe steel. Fig.2.7 shows a schematic representation of a CVN tester. The CVN test involves striking the specimen with a striker (hammer), mounted at the end of a pendulum.

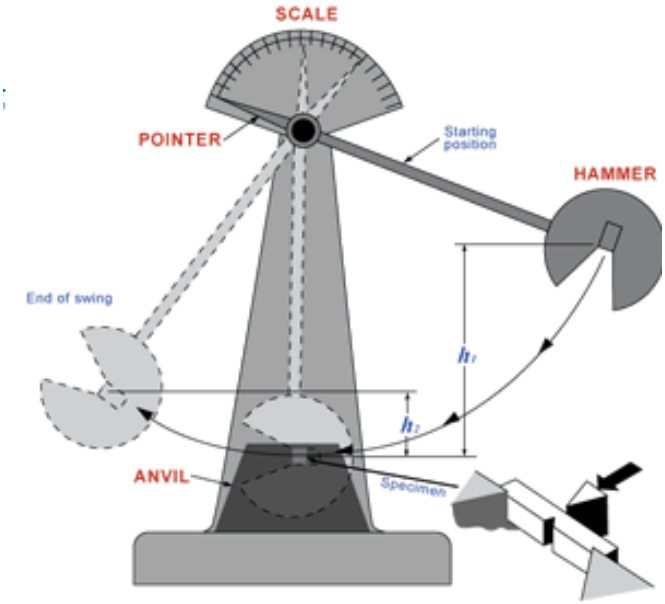

Fig.2.7 Schematic diagram of a CVN Impact tester.

The sample is fractured in a testing machine having a massive, pendulum-like hammer that swings in a vertical arc. The Charpy specimen is placed in the machine anvil using tongs such that the freely falling hammer strikes the specimen on the side opposite to the notch at the bottom of the vertical arc. The purpose of the notch is to promote failure of the specimen when

subjected to a high impact force (Fig.2.7). The value of toughness recorded indicates the energy imparted by the hammer to the specimen (or absorbed by the specimen) upon impact to fracture the specimen. This is based on the difference in hammer heights at the start of the test (h_1) and after the specimen fractures (h_2).

The CVN test procedure and the dimensions of the test specimens were as recommended in the Australian standard-1544.2 [35]. The arrangement of the supports (anvil), the striker and the specimen are shown in Fig.2.8.

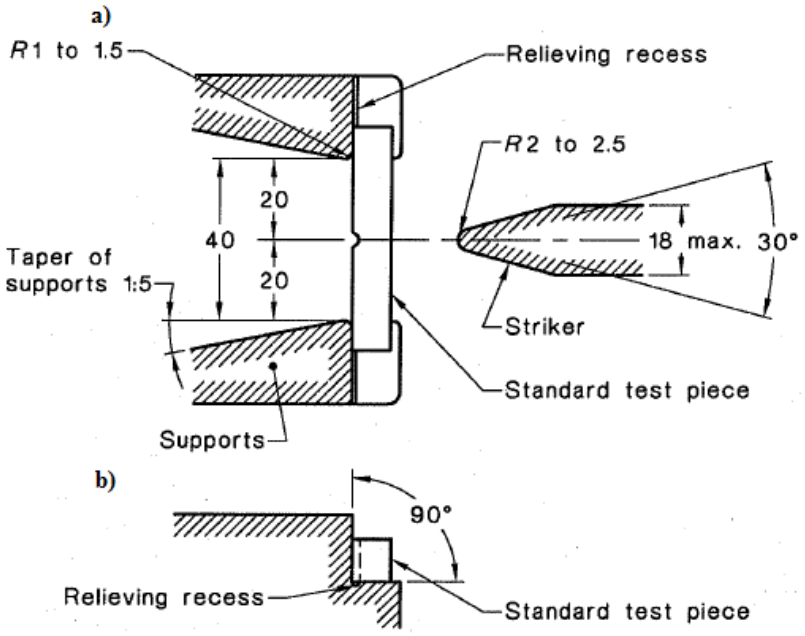

Fig.2.8 Anvil, CVN specimen and striker: (a) top view and (b) front view [35].

The specimen that fits in the Charpy impact tester is rectangular with a notch cut on one side. The notch represents a predetermined crack initiation location. Charpy specimens, in particular the notches, are carefully designed and prepared, since variations in notch dimensions will seriously affect the results of the tests. The specimens are smoothly machined and polished to a

smooth finish, and adhering to the tolerances given in Fig.2.9 is necessary to achieve accurate results.

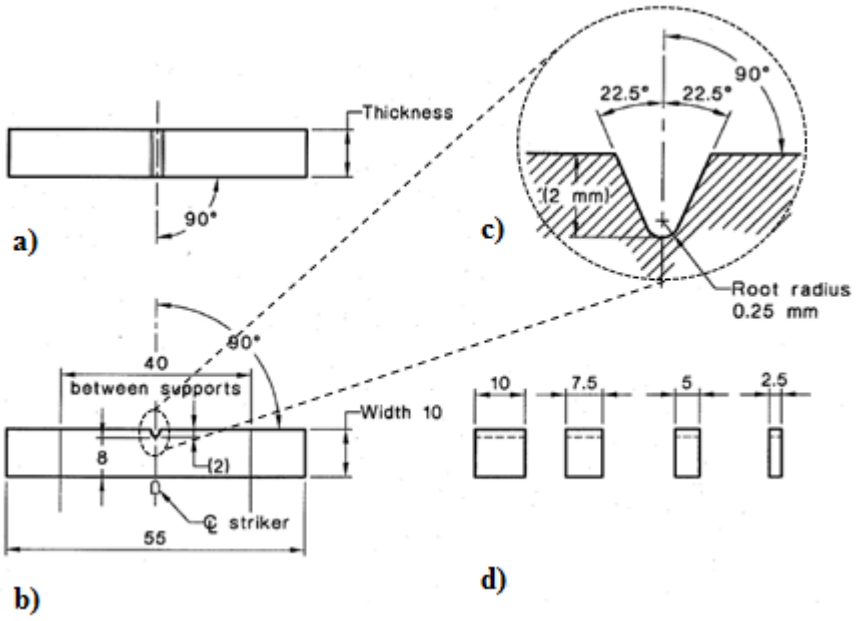

Fig.2.9 CVN specimen: (a) top view; (b) side view; (c) Notch detail; (d) Subsidiary specimens [35]

High energy readings indicate high material toughness. As the hammer strikes each specimen after falling from the same height, imparting the same high strain rate and stress to each specimen, and because the standard notch produces identical stress concentration conditions in the specimens, the CVN test can isolate the effect of temperature on toughness. To determine the effect of temperature, a series of samples are fractured over a wide range of temperatures. Their toughness values are recorded and a graph, of energy absorbed as a function of test temperature drawn. These tests are typically performed at low temperatures, or over a range of temperatures, to observe the dependence of toughness on temperatures. In the majority of cases, it is required

that the material fracture is in a ductile manner at all temperatures around the intended service temperature. Besides absorbing energy, the lateral expansion of the fractured samples and the percentage of shear area on the fracture faces, can also be determined and shown, as a function of test temperature. Such graphs yield several important pieces of information: the ductile-to-brittle transition temperature range separating ductile from brittle fracture behavior, the upper shelf energies (energy plateau) showing ductile fracture behavior and the lower shelf energies showing brittle fracture behavior. These energy values specify the properties of line pipe steel and safe operating temperatures to prevent fracture.

The fracture toughness of pipeline steel as obtained from the CVN impact test is one of the important critical factors in ensuring the structural integrity of pipelines. The pipeline steel is required to be able to dissipate enough energy to arrest a crack if it is initiated. This criterion can be assessed by a CVN test [36, 37].

The impact energy and shear area obtained from the CVN tests can be related to the structural behaviour full-scale testing of the line pipe. The shear area requirement from the CVN test is used to ensure that the line pipe steel is on the upper shelf at the minimum design temperature of the pipeline. The impact energy requirement is used to ensure that the toughness of the pipeline steel is sufficiently high to arrest a running ductile fracture.

CVN testing is also used to determine whether a line pipe steel specimen experiences a ductile-to-brittle transition with decreasing temperature. The ductile-to-brittle transition is related to the temperature dependence of the measured impact energy absorption [38].

Fig.2.10 shows the measured toughness of temperature. It is noticed that the transition process is not sudden and it can be so arranged that the fracture consists of both brittle and ductile modes [1]. At higher temperatures the absorbed energy is relatively large, corresponding to a ductile mode of fracture. As the temperature is lowered, the impact energy drops suddenly over a relatively narrow temperature range. Below this range, the energy has a constant but small value which implies that the mode of fracture is brittle. Toughness is largely affected by micro-structural factors, while the transition temperature is influenced by the effective grain size [22].

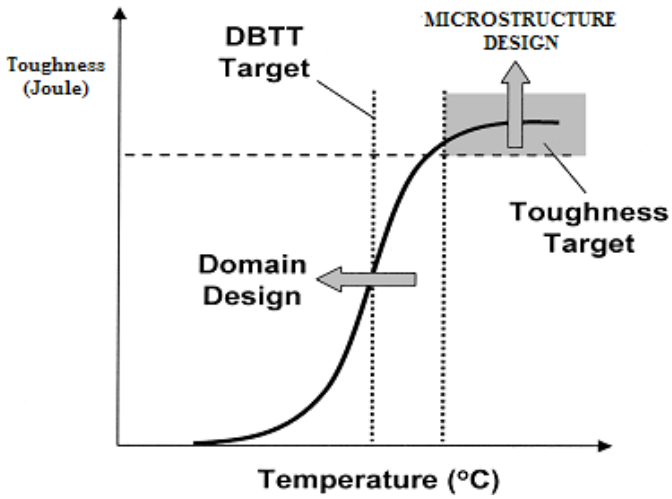

Fig.2.10 Toughness as a function of temperature [22].

The appearance of the failure surface is indicative of the nature of fracture, and may be used to determine the DBTT. For the ductile fracture, this surface appears fibrous or dull (or of 'shear' character). Conversely, totally brittle fracture surfaces have a granular (shiny) texture (or 'cleavage' character). Over the ductile-to-brittle transition, features of both types will coexist.

2.2.2 Single edge-notched tension test

Pipelines can be subjected to severe deformations and local defects resulting from bending generated by ground/soil movement or washout during installation and operation, and biaxial loading originating from longitudinal straining and internal pressure [1, 39, 40]. To fully explain pipeline failure, research is needed to develop a better understanding of the mechanical properties and fracture behavior (initiation and propagation) in both traditional and newly developed pipeline steels. Earlier, it was mentioned that the dynamic fracture toughness (Charpy energy) of pipeline steel can be determined by CVN impact testing. The static fracture toughness of pipeline steel can be obtained from a different type of fracture test, such as a single edge notched tension(SENT) test. Therefore, one of the representative specimens used to evaluate the fracture characteristics of the pipeline was designed to be compatible with a SENT test.

The fracture toughness data obtained from a SENT test can be more suitable for fracture predictions of pressurized pipelines and cylindrical vessels than data obtained from notched fracture specimens under bending and impact loading [41].

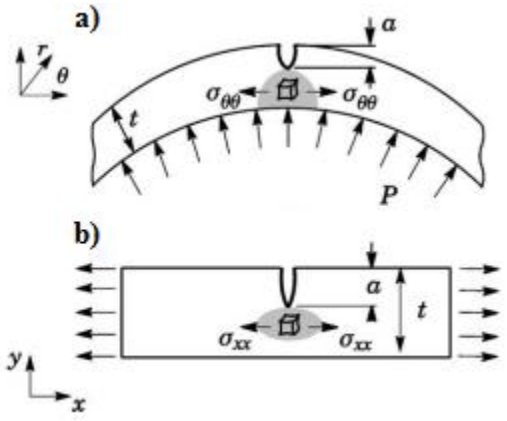

Fig.2.11 (a) Schematic loading condition for a pressured pipe; (b) SENT test specimen [41].

This is because a SENT test specimen notch resembles surface cracks in pipes more closely, and generates a similar stress field at the crack tip (Fig.2.11). The fracture toughness obtained using SENT specimens has been recommended by DNV-OS-F101 [42] and DNV-RP-F108 [43]. Recently, a British Standard for the SENT test method has been developed based on DNV-RP-F108. However, the toughness value obtained from the SENT test should be correctly applied to full-scale pipe components.

2.2.3 Finite element simulation of CVN and SENT tests

Three-dimensional fracture simulations of both CVN and SENT tests have been carried out using the commercial FEM software. These simulations provide a better understanding of the fracture and plastic deformation of the small scale specimen.

The ductile crack growth of the line pipe steels at ambient temperature proceeds via the nucleation, growth and coalescence of micro-voids. As the specimen is loaded, the local strain and stress at the crack tip become sufficient to cause nucleation of voids. These voids grow as the crack blunts, and link with the main crack [40] . The Gurson-Tvergaard-Needleman (GTN) constitutive model has recently become increasingly popular to simulate the growth of voids during deformation.

a) Gurson-Tveergard –Needleman (GTN) Constitutive model

The simulation of ductile fracture and plastic flow localization can be carried out using the GTN model. For a porous solid with voids volume fraction f (with the voids randomly distributed), the yield function can be expressed as follows [44]:

$$\phi(\sigma, f, \bar{\sigma}) = \frac{\sigma_e^2}{\bar{\sigma}^2} + 2q_1 f \cosh\left(\frac{3q_2\sigma_m}{2\bar{\sigma}}\right) - 1 - (q_1 f)^2 = 0 \quad (2.1)$$

where the constants q_1 and q_2 were introduced by Tvergaard [45] to bring the predictions of the model into closer agreement with the full numerical analyses using a periodic array of voids; σ_m and σ_e are the mean normal and effective parts of the average macroscopic Cauchy stress σ, and $\bar{\sigma}$ is the yield stress of the matrix material.

Ductile damage can be correlated to the void volume fraction, f, which is controlled by local strains. The evolution (time rate of change) of f can be expressed as the sum of two terms representing the evolution of void nucleation and growth:

$$\dot{f} = \dot{f}_{\text{growth}} + \dot{f}_{\text{nucl}} \quad (2.2)$$

As the material around the voids is considered to be volume-conservative (i.e the volume of the matrix does not depend on void number and size), the void growth rate can be related to the plastic volume dilatation rate as follows:

$$\dot{f}_{\text{growth}} = (1 - f) \cdot \dot{e}^p_{kk} \quad (2.3)$$

where $\dot{e}_{kk}^{p}$ are the components of the mesoscopic plastic strain rate tensor.

The void nucleation rate can be determined by:

$$\dot{f}_{nucl} = \dot{\varepsilon}^{p} \frac{f_n}{s_n\sqrt{2\pi}} exp\left(-\frac{1}{2}\left(\frac{\varepsilon^{p}-\varepsilon_n}{s_n}\right)^2\right) \tag{2.4}$$

whereε^{p} is the main effective plastic strain rate of the material; ε_n is the mean void nucleation strains: s_n is the corresponding standard deviation of the distribution; f_n is controls the amplitude of the nucleation rate.

Once the failure by void coalescence is initiated according to a specific criterion, numerically it is preferable to simulate the material separation gradually, rather than suddenly. Therefore, a modification using the parameter f* instead of f in Eq.(2.1) has been proposed by Tvergaard and Needleman [45, 46]:

$$f^{*} = \begin{cases} f\,, & \text{if } f \le f_c \\ f_c + \frac{f_u^{*}-f_c}{f_f-f_c}\cdot(f-f_c) & \text{if } f > f_c \end{cases} \tag{2.5}$$

where f_c is the critical void volume fraction at which the voids coalesce, f_f is the void volume fraction at failure of the material and f^{*}_u= 1/q_1 is the ultimate void volume fraction.

b) Simulation of CVN testing

Many researchers have developed both two-dimensional and three-dimensional explicit dynamic finite element simulations of the CVN test for structural materials with the GTN constitutive damage model.

A model of the ductile-to-brittle fracture transition of the pressure vessel steel was developed by Tanguy et al. [47]. The simulation included a detailed description of the material visco-plastic deformation over a wide temperature range. The ductile behaviour was modelled using a Gurson-type model. The CVN test was simulated using a full three-dimensional mesh while accounting for adiabatic heating and contacts between the specimen, the striker and the anvil. The developed model was well suited to simulating ductile tearing. It was shown that quasi-static and dynamic tests could be consistently modelled.

A methodology to correlate the upper shelf energy (USE) of the full-size and sub-size Charpy specimens of a nuclear reactor pressure vessel plate material was proposed by Schubert et al. [48]. It was found that the USE could be normalized using a factor involving the full-size dimension of the Charpy specimen, the elastic stress concentration factor, and the plastic constraint at the root of the notch. The normalized values of the USE were found to be invariant with the specimen size. Moreover, the ratios of the USE for un-irradiated material to that for irradiated materials were also found to be approximately the same for full-sized, half-sized, and one-third-size specimens.

Experiments and finite element simulations of Charpy tests on X70 line pipe steel were performed by Thibaux et al. [49]. Ductile fracture was simulated using the GTN damage model. It was observed that the ductile fracture did not break the sample into two parts. The crack was found to propagate for about 6 to 7 mm, after which it deviated and stopped growing when the crack reached the wider part of the sample due to bending. FE simulations showed that this resulted in a quasi-constant force during a ~10 mm displacement of the hammer. The consequence was that more than 25% of the energy was dissipated in a different fracture mode at the end of the test. FE simulations also showed that damage had already occurred when the load reached the maximum value, but that the damage had almost no influence on the load for two-thirds of the displacement at the maximum load. This implies that more than 27 J were dissipated by plastic bending before the initiation of the crack. From the findings of this study [49], it can be concluded that the results of the CVN test are very sensitive to crack initiation and that only a limited part of the test can lead to a meaningful description of crack propagation. Therefore, it is questionable if the CVN test is suitable for predicting the crack arrest capacity of steels with high crack initiation energy.

Thibaux [37] carried out instrumented CVN tests on X70 line pipe steel specimens along with FE simulations using the GTN model. The simulations provided a new insight into crack propagation during the impact test, via a detailed analysis of the crack length during each test. This method allowed a more accurate description of the crack propagation than those provided by traditional approaches using the impact energy criterion. The method is mainly based on the reduction in the slope of the load-deflection curve once the crack is initiated. The application of the CVN test as a measure of the crack arrest capacity of a material was discussed. FE

simulations showed that the maximum energy absorbed during an impact test ranges from 400 J to 500 J, which can be calculated as a case without crack initiation. Increasing the impact energy of the material led mainly to an increase in the resistance to crack initiation, but it did not guarantee an improved resistance to crack propagation.

c) Simulation of SENT testing

A number of researchers have carried out simulations of tensile tests to investigate ductile fracture [50-53]. Oh et al. [54] developed a phenomenological model of ductile fracture for API X65 steel using the GTN model. Experimental tests and FE damage simulations using the GTN model were performed for smooth and notched tensile bars, from which the parameters in the GTN model were calibrated. Comparison of experimental data of pre-strained notched tensile and fracture toughness tests with FE damage analyses showed good agreements, suggesting the validity of the calibration parameters. The developed GTN model was applied to predict the pre-strain effect on deformation and fracture and the results were compared with experimental data.

Chen et al. [52, 55] developed three-dimensional FE simulations of SENT tests were performed on the line pipe steel, using GTN constitutive model. Ductile fracture initiation and propagation were investigated. The main objective of this study was to develop a three-dimensional FE simulation of the fracture that allows investigation of the ductile fracture in a SENT specimen for the chosen line pipe steel. The load-displacement curve obtained from the numerical modelling was in good agreement with the experimental load curve. The simulation provided fracture

evaluation at any node and element of a structure and stress/strain and load/displacement are determined.

Nourpanah et al. [56] presented a fracture simulation of a SENT specimen with various notch lengths using the GTN model to predict ductile crack growth. Their results showed that half of the simulated SENT specimen demonstrated similar fracture behaviour of the pipe with various dimensions and internal pressure.

2.3 Acoustic Emission (AE) monitoring

The Acoustic emission (AE) testing technique has been recognized as an effective non-destructive testing (NDT) method that can be used to detect and locate faults in mechanically loaded structures and components. AE can provide comprehensive information on the initiation of a discontinuity (flaw) in a stressed material. The word “acoustic” is derived from the Greek word ‘akoustikos’, refers to hearing [7].

Acoustic emission is a phenomenon whereby transient stress waves or displacement waves are generated following the rapid release of energy from localized sources such as crack initiation sites, fracture propagation and dislocation motion in metals [8, 11]. Elastic energy is transmitted through the material in the form of transient elastic waves and can be detected by sensors on the surface of the specimen (Fig.2.12).

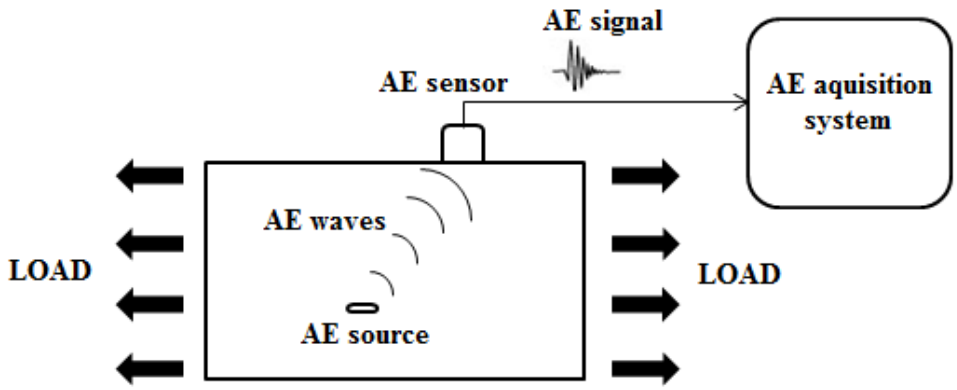

Fig.2.12 Schematic of AE monitoring technique.

The sensor used in the AE measurement converts elastic waves into electrical signals which are then processed and analyzed by special hardware and software. Useful AE signals need to be distinguished from the background noise generated from the surroundings [57, 58]. Fig.2.13 shows typical acoustic emission signal types. There are two main types of useful AE signal: 'burst' and 'continuous'. Burst AE signals correspond to individual events such as stages of crack growth, brittle fracture and impact. Continuous AE signals correspond to sustained signals generated by time-overlapping events such as plastic deformation, friction and liquid leaks [11, 59]. It has been demonstrated that continuous low-amplitude AE signals are generated from low-energy sources. Discrete high-amplitude AE signals are generated from high-energy sources [60].

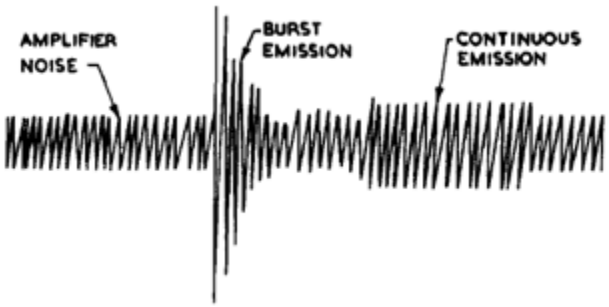

Fig.2.13 Typical AE types [61].

Studies of AE gained momentum in the late 19th century [62]. The characteristic sound of a material being bent was analyzed during the twinning of tin and zinc. Since then a number of studies have reported that audible sound could be received from plastic and shear deformation of an alloy of aluminum and manganese [63]. In the 1940s, the following attempts were made to correlate AE to material behavior: Robert Anderson carried out further scientific research on AE during tensile testing of an aluminum alloy beyond its yield point, Erich Scheil attempted to link the formation of martensite in steel to audible noise emission [64], and Friedrich Forster, in collaboration with Scheil, studied audible noise emission during the formation of martensite in high-nickel steel [64].

The most important experimental achievement was that of Kaiser [7, 8] in the 1950's, who wrote his PhD thesis entitled "Results and Conclusions from Measurements of Sound in Metallic Materials under Tensile Stress". Kaiser carried out a systematic study on AE using electronic instrumentation for the first time [65]. He used tensile tests to determine the characteristics of AE in engineering materials. The result from his investigation was the observation of the irreversibility phenomenon that now bears his name, the 'Kaiser Effect'. Fig.2.14 shows the Kaiser effect during mechanical testing, in which the cumulative emission is plotted against the applied load. As the load increases from Point A to Point B, AE is observed to increase but not upon unloading (line B→C). Upon reapplying the load (line C→B), no AE is observed until Point B is reached again. Further increasing in the load increases the AE (B→D). The absence of detectable AE at a fixed sensitivity level until the previously applied stress levels are exceeded was termed the 'Kaiser effect'.

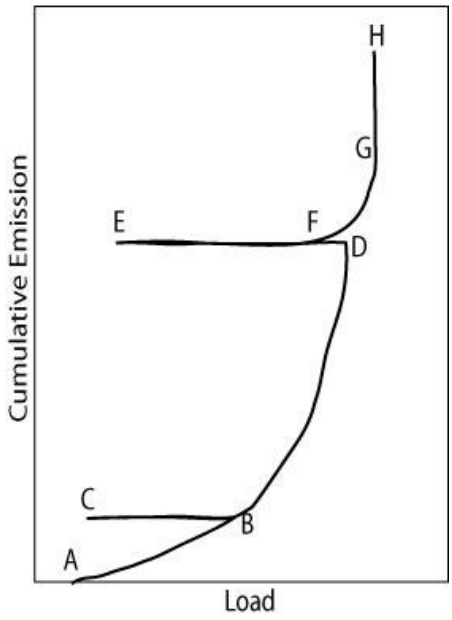

Fig.2.14 The Kaiser Effect during tensile test [65].

Since Kaiser's research, other researchers have continued to investigate AE during crack growth. In 1954, after becoming aware of Kaiser's research, Bradford Schofield [62] established the first research program on applications of AE to material engineering and on sources of AE, in the USA. He found that AE was mainly a 'volume effect' and not a 'surface effect'. This allowed the AE technique to be applied to investigate material characterization and to structural evaluation. In the late 1960s and 1970s, many scientists formed AE working groups for the exchange of ideas and information, paving the way to systematic research. The most significant research achievement during this period was the discovery that dislocations were the main source of AE [66]. Currently, the AE technique is used in many industries for different types of materials and structures as a non-destructive testing method.

A major advantage of AE measurement is that it can monitor in real time the development of defects occurring inside the material without further damaging the material [67, 68]. However,

for some applications, the operating environments are often very noisy, while the AE signals are usually very weak. This makes the detection of the AE signal a challenging task.

2.3.1 AE system

An AE acquisition system usually consists of a sensor, an amplifier, and data acquisition and analysis software as shown in Fig.2.15. An AE elastic wave is detected by the sensor and the signal is then amplified and digitalized [62, 69].

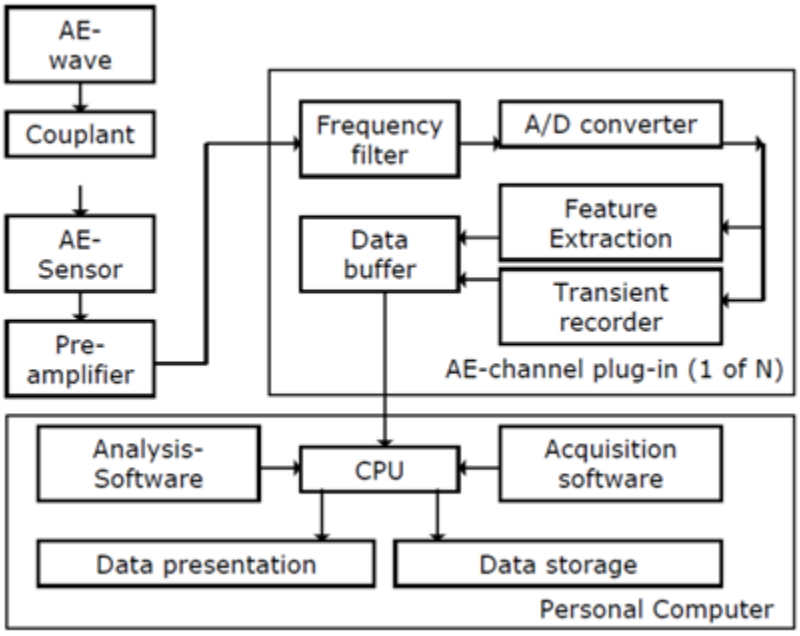

Fig.2.15 A schematic of AE acquisition system [69].

The transducer (sensor) is the most important element for the quality of AE wave acquisition. A good sensor should be highly sensitive, have a wide frequency range and be easily attached to the specimen surface [70]. Fig.2.16 presents a schematic diagram of a typical sensor. Wide band

sensors (with piezoelectric element) have been used in many applications. They are very useful where the frequency analysis of the AE signal is required. Fig.2.17 shows various AE wideband sensors.

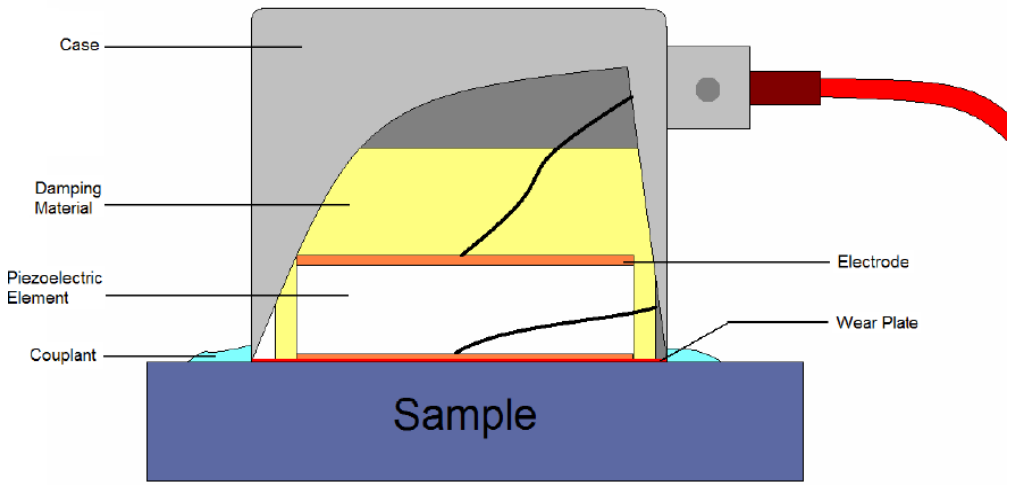

Fig.2.16 Schematic of an AE sensor.

Fig.2.17 Commercial AE sensors.

In order to improve the transmission of elastic wave signal, a proper coupling agent must be used to provide an effective contact between the sensor and the test material. There are several agents

commonly used, such as silicone grease (high vacuum grease), oil, glue and ultrasonic gel, and magnetic clamp [71].

The sensor is connected to a preamplifier by a cable. The amplifier is usually placed close to the sensor to minimize electromagnetic interference. The amplifier amplifies the AE signal to usable voltage and has plug-in frequency filters to eliminate mechanical noise and background noise [72].

The data acquisition system digitizes the AE waves and allows real-time processing of AE waveforms. AE software manages all data acquisition, graphing and analysis.

2.4 AE signal analysis

2.4.1 AE wave modes

Acoustic waves are created and propagated when an unbalanced force occurs due to internal changes in a stressed material. This unbalanced force appears when there is sudden plastic strain or sudden formation of a new surface in the material. For example, in a brittle material, a new surface is suddenly created and material near the new surfaces quickly migrates in the direction of the unbalanced tractive forces [73]. The wave equation is:

$$\rho\ddot{u} = F(x,t) + (\lambda + 2\mu)\nabla(\nabla \cdot u) - \mu\nabla X\ (\nabla\ X\ u) \tag{2.6}$$

where ρ is the material density, u is the particle displacement at the position (X) and time (t), F is the external driving force per unit volume (often zero), ∇- represents the force on unit volume resulting from the stress field gradients in all three directions X_(1,) X_(2,) X_(3,), $\boldsymbol{\lambda}$ is the elastic constants known as the Lamè constants, μ is the shear modulus and (λ+2μ) is the elastic modulus applicable to unidirectional tensile/ compressive strain.

The mechanical elastic waves propagate through solid materials in a number of modes such as longitudinal, transverse, and surface, as shown in Fig.2.18.

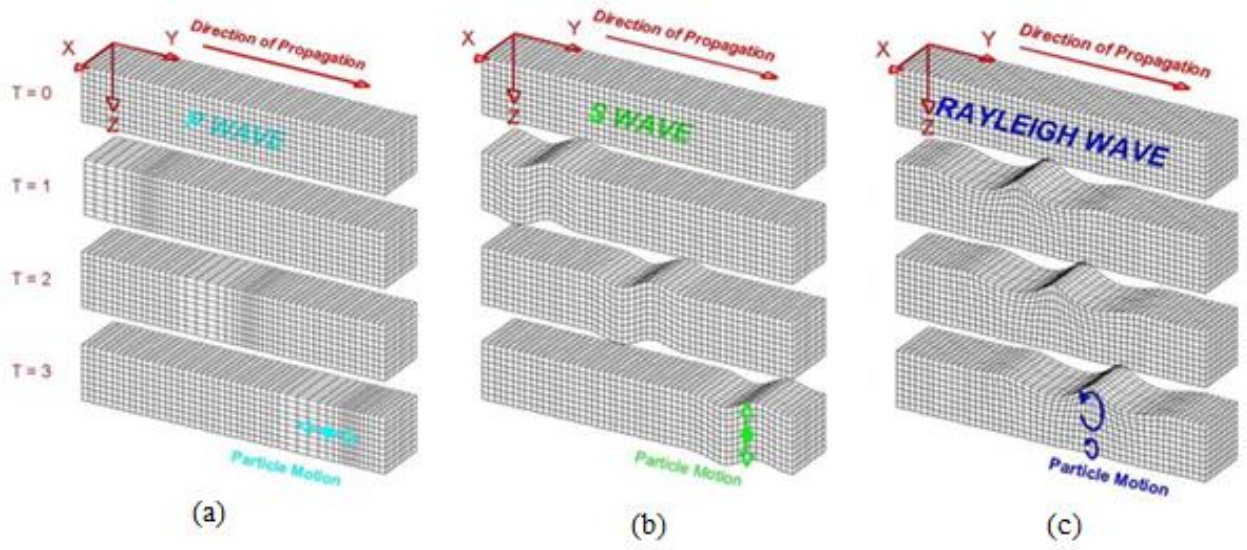

Fig.2.18 AE Wave modes: (a) longitudinal, (b) shear, (c) surface.

The longitudinal waves, body or bulk waves are called ‘primary’ or ‘P’ waves. In a P wave, particles oscillate parallel to wave propagation. In a shear (‘S’) wave the oscillations are perpendicular to the direction of wave propagation. A ‘Rayleigh’ wave, also called a ‘surface’

wave, is the wave in which the particle motion in planes normal to the surface and parallel to the direction of the wave propagation.

2.4.2 AE signal analysis

There are two approaches to analyze AE signals: '*Parameter-based'* and '*Waveform-based'* [8]. Several AE parameters, such as oscillation count, amplitude, energy, event duration and rise time, can be derived from the AE signal. The major parameters used in the parameter-based analysis of the AE signal are shown in Fig.2.19.

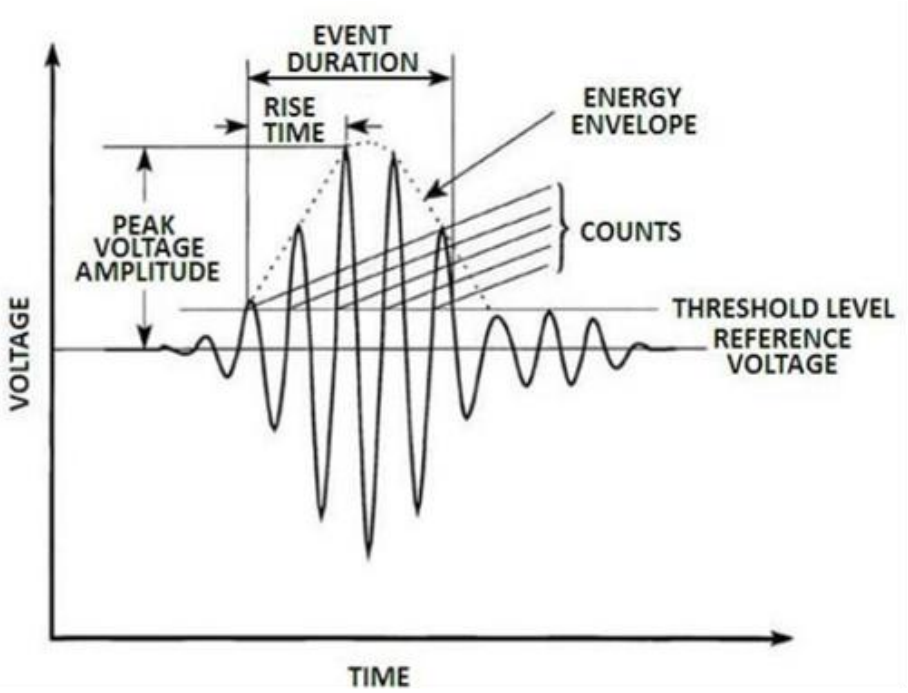

Fig.2.19 AE parameters.

These parameters are characterized as follows [74]:

Peak amplitude: Amplitude (A) is the highest peak voltage attained by an AE waveform. This is a significant parameter which is directly related to the magnitude of the AE event. The AE amplitude is measured in decibel (logarithmic) scale.

Threshold: Recording is triggered once the output signal reaches a set threshold value. This value is set to remove as much noise as possible, but care should be taken so that a weak AE signal does not escape detection by setting the threshold too high.

Hit: A signal that exceeds the threshold value and causes a system channel to accumulate data is known as hit, thereby describing an AE event. The Event Rate is the number of events/hits per unit time. AE hits are individual signal bursts produced by local changes in the material. The hit count is the number of times a signal crosses a preset threshold.

Energy: Integral of the rectified voltage signal over the duration of the AE hit (see Fig.2.19) Energy of the signal conveys information about the strength of the AE source.

$$\text{Energy}=A(db)+10\log(D) \tag{2.7}$$

Count (N): Number of AE hits that exceed the threshold value. Count rate is also used regularly and denotes the number of counts per unit time.

Average Frequency: Determines the average frequency in kHz over the entire AE event.

$$A.F = \frac{AE\ counts}{Duration}\ [kHz] \tag{2.8}$$

Rise time: The time it takes from the first threshold crossing to reach the maximum amplitude. Rise amplitude-rise time divided by Amplitude this can be used to arrange signals from tensile and shear crack.

Duration(D): The time spans from the first threshold to the end of the last threshold crossing.

The AE waveform and frequency analysis is usually carried out using Fast Fourier Transform and Wavelet Transform [9,10, 57]. Identification of the AE signal can be based on the type of AE waveform and its frequency range. Fig.2.20 shows two AE waveforms: 'burst' and 'continuous'. Burst-type AE signals are discrete signals corresponding to individual events such as stages of crack growth, brittle fracture or impact. On the other hand, continuous AE signals are sustained signals generated by events such as plastic deformation, friction and liquid leaks [11].

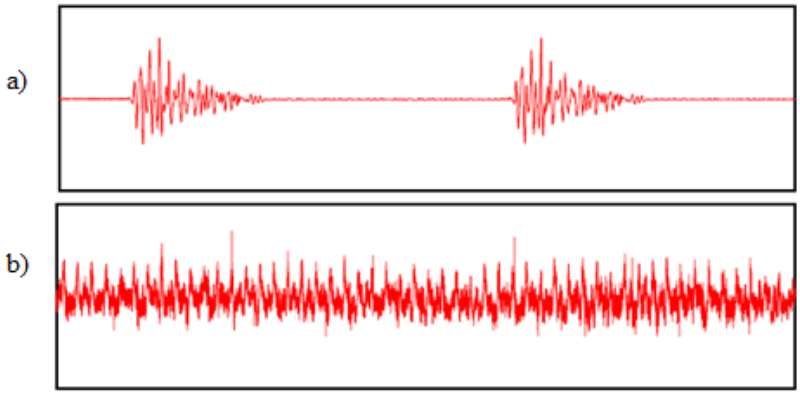

Fig.2.20 AE signals: (a) burst and (b) continuous [11].

The AE analysis during the fatigue cracking was investigated using waveform analysis with frequency spectrum [10]. There were three types of waveforms, each with corresponding frequency spectrum from micro-cracks. Fig.2.21 shows that waveform and its frequency spectrum from fatigue cracking (a) and (b); fretting (c) and (d); and noise (e) and (f). The micro-crack (a) and b) had strong high frequency components above 0.5 MHz in comparison with fretting and noise, although peak amplitude was generally low.

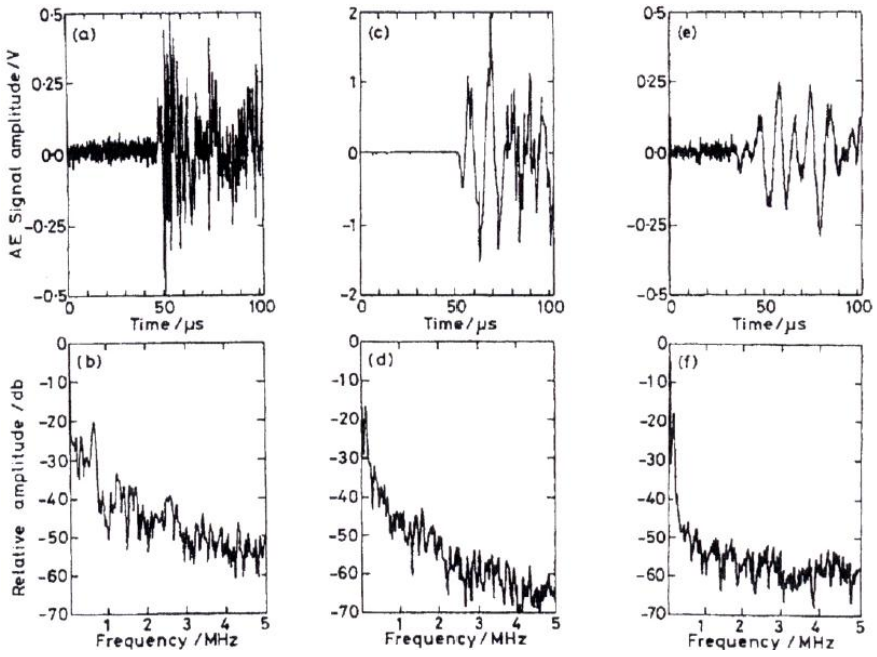

Fig.2.21 Wave forms and corresponding frequency spectra [10].

2.4.3 AE sources

Generally, an AE signal is generated upon the initiation and growth of cracks, due to slip and dislocation movements, twinning, or phase transformation in metals. In these cases, stress plays an important role in giving rise to AE. Plastic deformation is induced by permanent changes in the positions of atoms in metals. These changes are related to and based on the movement of the

dislocations [62]. In addition, fracture occurs when the material breaks and new surfaces are produced. Fig.2.22 presents the AE sources from steel. The major macroscopic AE sources from steel specimens are crack jumps, development of plastic deformation, fracturing and de-bonding of hard inclusions. The main microscopic AE sources include dislocation movement, interaction, annihilation, slip formation, void nucleation, void growth and void interaction [75-77].

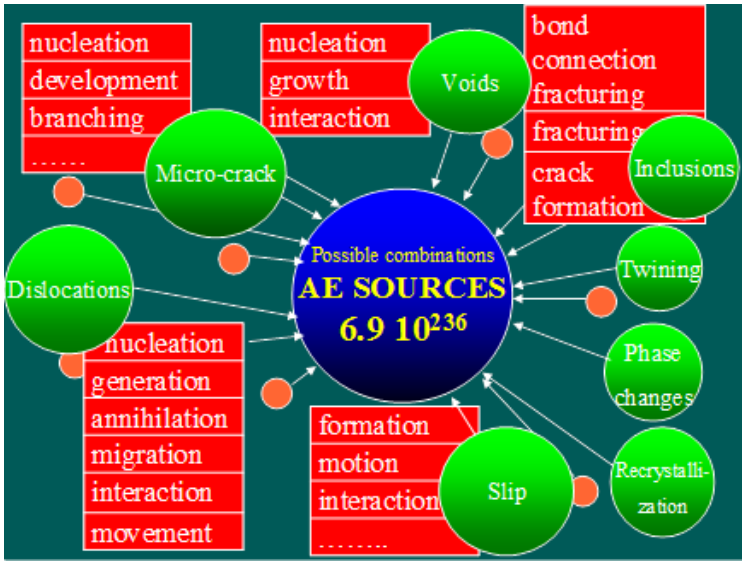

Fig.2.22 AE source from steel in the micro and macro structure [62].

The most detectable AE signals are generated when a loaded material undergoes plastic deformation or when a material is loaded at or near its yield stress [78]. AE activity can also be observed when the material ahead of the crack tip undergoes plastic deformation (micro-yielding). In primary emissions arising from crack growth, there are two sources of cracks that affect the AE [79]. In the first case, there may be emissive particles (e.g. nonmetallic inclusions) in the stress concentration region near the crack tip. Since these particles are less ductile than the surrounding material, they tend to break more easily when the metal is strained, resulting in an

AE signal. The second AE source is the propagation of the crack tip that occurs as a result of the movement of dislocations and small-scale cleavage produced by tri-axial stresses.

The amount of energy released by an AE and the amplitude of the waveform are proportional to the magnitude of the event. Large and discrete crack jumps will produce larger AE signals than cracks that propagate slowly over the same distance. An AE signal arising from crack propagation may be of a higher frequency than that arising from plastic deformation. An AE signal arising from brittle fracture has a higher frequency than that arising from ductile fracture. Generally, the highest frequency is observed for brittle fracture, crack and crack growth, while lower frequencies are observed for plastic deformation [57]. However, there is no general recommendation to attribute specific frequency ranges to a given fracture mechanism because fracture-related AE features vary with material type, sample geometry [80] and the parameters of the AE acquisition system [8].

Table 2.1 Acoustic emission factors vs changes of AE amplitude.

AE Amplitude	
Increase	Decrease
High strength	Low strength
High strain rate	Low strain rate
Low temperature	High temperature
Anisotropy	Isotropy
Heterogeneity	Homogeneity
Thick sections	Thin sections
Brittle failure (cleavage)	Ductile failure (shear)
Material containing discontinuities	Material without discontinuities
Martensitic phase transformations	Diffusion controlled phase transformations
Crack propagation	Plastic propagation
Cast materials	Wrought materials
Large grain size	Small grain size
Mechanical induced twinning	Thermally induced twinning

Table 2.1 [81] shows factors that generally tend to increase and decrease the amplitude of acoustic emission.It can be seen from Table 2.1 that an AE signal arising from crack propagation may be of higher amplitude than one arising from plastic deformation. An AE signal generated at low test temperature may correspond to higher AE activity than one generated at high test temperature. Moreover, an AE signal from brittle fracture has a higher amplitude than that from ductile fracture [57].

Energy conservation during crack growth for ductile and brittle fracture is shown in Fig.2.23. There are three type of source energy released from crack growth: surface energy, plastic deformation and AE event energy [73]. Surface energy is the energy needed to disband single layers of atoms that form the newly created surface. This surface energy is greater in ductile fracture than brittle fracture. In ductile fracture, most of the energy is dissipated in plastic deformation and a small of energy is generated from AE energy. On the other hand, in brittle fracture, more than two thirds of the energy goes to AE energy and the remainder comes from plastic deformation and surface dis-bonding.

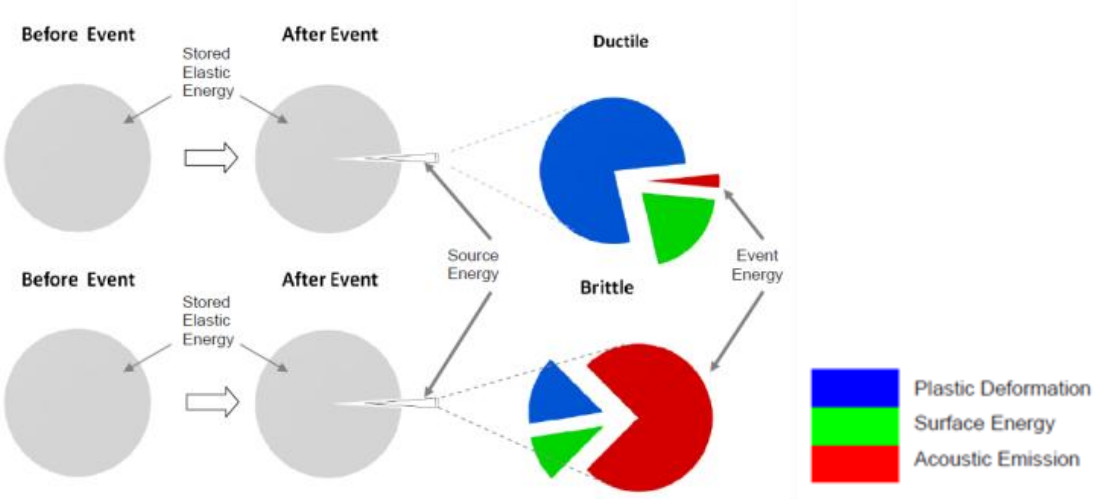

Fig.2.23 A schematic of energy distribution before and after fracture behavior [73].

General characteristic trends of AE features from various AE sources are shown in Table 2.2. There is no general theory as to what frequency ranges should be attributed to a given fracture mechanism, due to variation in the fracture mechanisms with varying material and test types. Although a substantial amount of qualitative research data have been published, a considerable experimental study should be carried out to validate the correlation of the quantitative parameters of AE signals with the parameters of AE sources.

Table 2.2 General Characteristics of AE waveform features from various sources.

AE sources	Factors	AE waveform parameters						Ref
		Amplitude range	Frequency content	Duration	Rise time	Count	Waveform/ signal type	
Fracture modes	Ductile fracture	Low	Low	Long	Low	Low	Continuous signal	[57]
	Brittle fracture	High	High	Short	High	High	Burst signal	
Material behavior	Plastic deformation	Low	Low	long	Low	-	Continuous signal	[10]
	Crack initiation and propagation	High	High	Short	High	-	Burst signal	[82, 83]
Crack type	Tensile mode-I	High	High	Short	high		Longitudinal wave	[8]
	Shear mode-II	Low	Low	long	low		Shear wave	
Notch effect	Notch specimen	High	-	-	-	low	-	[84]
	Plain specimen	Low	-	-	-	high	-	
Strain rate effect	High Strain rate	High	-	-	-	-	-	[85]
	Low strain rate	Low	-	-	-	-	-	
Temperature effect	Low Temperature	High	High	Short	high	-	Burst signal	[10]
	High Temperature	Low	Low	Long	low	-	Continuous	
Noise effect		Constant	Low	-	-	-	Circular waveform	[10, 57]

2.4.4 Relationship between AE parameters and fracture parameter

The dependence of the AE signature on fracture parameters is a significant and interesting problem that calls for new research. Important early attempts were made to correlate AE with plastic deformation size using stress intensity factors. Based on fracture mechanics, the stress concentration at the front of the crack tip can be expressed in terms of the stress intensity factor (K). The 'plastic zone model' was developed to relate the stress intensity factor to the AE parameter. The material gives the highest rate of AE when it is loaded to the yield strain.

The size and shape of the plastic zone ahead of the crack are determined from linear elastic fracture mechanics concepts [40].

$$r_y = \frac{1}{\alpha\pi}\left[\frac{K_1}{\sigma_{ys}}\right]^2 \tag{2.9}$$

α=2 or 6 (plain stress or plain strain)

where K is the stress intensity factor, E is the elasticity modulus and σ_{ys} is the yield stress.

Strains at the crack tip vary at $r^{-0.5}$ where r is the radial distance from the crack tip.

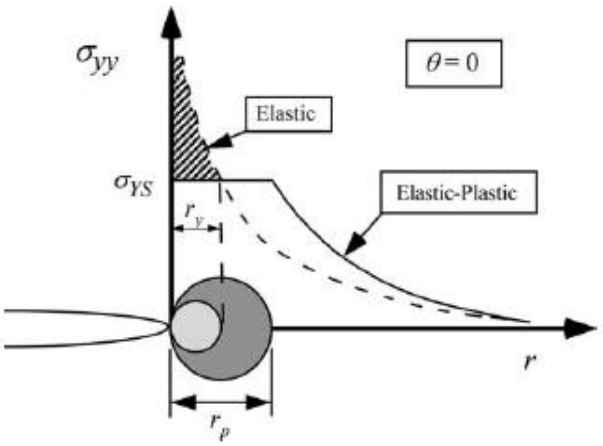

Fig.2.24 Plastic zone ahead of the crack tip [40].

$$N \propto V_p \tag{2.10}$$

where N is AE count rate, V_p is the volume strained between ε_y (yield strain) and ε_u (uniform strain).

The plastic zone model leads to development of the following equations for α=2

$$V_p \cong \pi(r_y^2 - r_u^2)B = \pi B\left[\frac{1}{2\pi}\left(\frac{K}{E\varepsilon_y}\right)^2\right]^2 - \left[\frac{1}{2\pi}\left(\frac{K}{E\varepsilon_u}\right)^2\right]^2 = \frac{B}{4\pi}\left[\frac{r_y^2 - r_u^2}{4\pi(E\varepsilon_y\varepsilon_u)}\right]K^4 \tag{2.11}$$

$$V_p \propto K^4$$

where B is the plate thickness.

The relationship between acoustic emission counts and volume of the crack tip is as follows:

$$V_p = B_0 \sum N \tag{2.12}$$

where B_0 is a proportionally constant and $\sum$N is the total cumulative acoustic emission measured during test.

Combination of Eq.(2.11) and Eq.(2.12) indicates that the AE count rate (N) from a specimen containing a crack is proportional to the forth power of the stress intensity factor (K) [86].

$$N \infty K^4 \tag{2.13}$$

It was found [86] that the acoustic emission count is proportional to the stress intensity factor during tensile test of six beryllium fracture specimens (Fig.2.25).

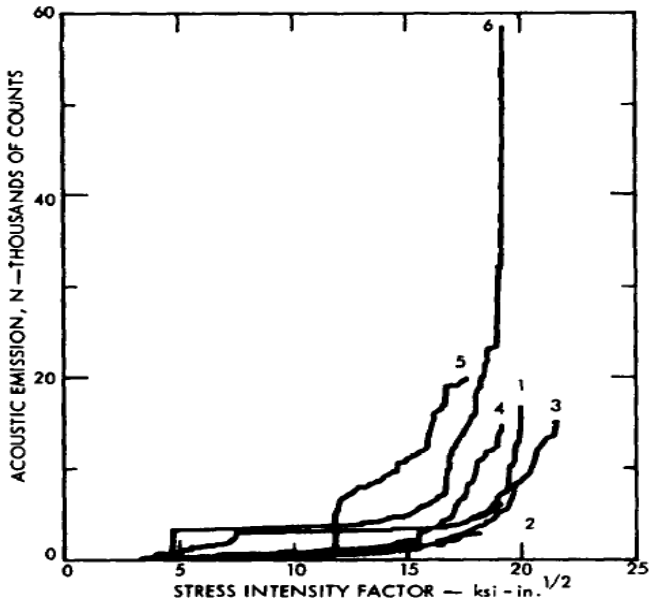

Fig.2.25 AE counts as a function stress intensity factor [86].

Palmer and Herald investigated the application of acoustic emission measurement to fracture mechanics related to the calculation of the total count prior to failure as function of defect size [87]. They found that acoustic emission count was directly proportional to the plastic zone size. During fracture tests of pressure vessel steel, the AE count rose rapidly until a yield point and then fell down because of the decrease in the expansion of plastic zone. It was also observed that most of the acoustic emission activities appeared before 2% strain during rising load [86].

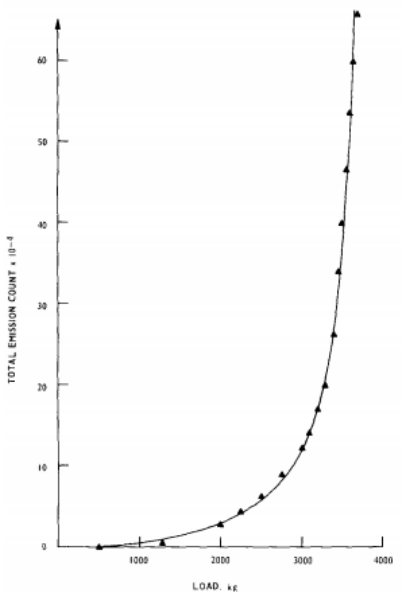

Fig.2.26 Load and AE count [86].

Dilipkumar and Wood [88] developed a quantitative relationship between fracture toughness, fracture mode and acoustic emission parameter including cumulative count. They proposed that the cumulative AE counts (N) is proportional to the crack length as described by:

$$N \infty \beta a \tag{2.14}$$

where β is the value of proportionality constant which is related to fracture toughness and fracture mode and material properties.

Palmer and his co-workers [89] investigated the relationship between AE parameters and fracture parameters. They found that the acoustic emission count was linearly proportional to the crack opening displacement.

Blanchette proposed [90, 91] that the cumulative ring-down count was proportional to the number of fractured second particles and the volume of material being plastically strained during the crack growth. They have developed following equation:

$$N\left(\frac{a}{w}\right) = \frac{\beta B D_o E W}{6(1-\nu^2)\sigma_y^2} \int_{\frac{a_o}{w}}^{\frac{a}{w}} G\left(\frac{a}{w}\right) d(a/w) \tag{2.15}$$

where N is the AE cumulative ring-down count, a_o is the initial crack length, B is the thickness, D_o is the density of inclusion-type particle (it can be measured on image analyzer).

$$G = (1-\nu^2)K^2/E \tag{2.16}$$

where G is the elastic energy release rate, ν is the Poisson's ratio, E is Young's modulus and σ_y is the yield stress.

Another equation linking the AE count to the fracture parameter was developed by Lysak [92] which is expressed as:

$$N = \beta M \tag{2.17}$$

$$M = -\frac{\alpha_1 K_{1c}^2 F(K_1)}{K_1^2 + K_{10}^2} F(K_1) = \frac{K_1^2 - K_{10}^2}{K_c^2} + ln\frac{K_c^2 - K_1^2}{K_c^2 - K_{10}^2}$$

$$\alpha_1 = \beta\alpha_2; \quad \alpha_2 = \alpha_3 E/a; \ \alpha_3 = \pi\sigma\beta\sigma_{02}/6E$$

where β is a proportionality factor.K_c^2 and K_{10}^2 are the critical and initial values of K_1, σ_{02} is the material yield stress and E is the elasticity modulus.

Fig.2.27 shows good agreement between prediction (curve) by Eq.(2.15) and the experimental AE data (symbols). The white and black squares symbols in the figure represent the results of grey cast iron and Ti3Al respectively, while the white and black circles symbols represent the high strength and malleable cast iron.

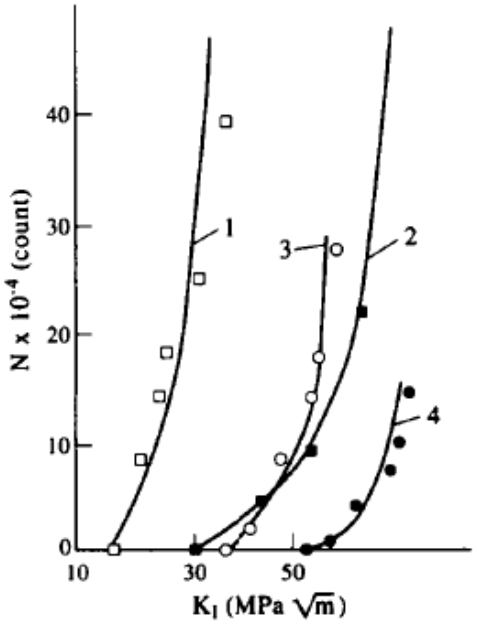

Fig.2.27 Dependence of acoustic emission count and stress intensity factor [91].

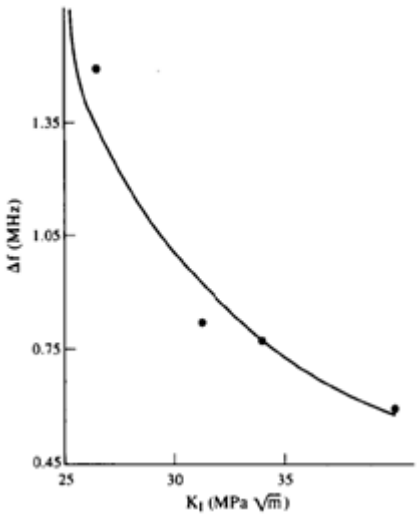

Fig.2.28 Dependence of frequency and K (points from experimental result) [92].

Lysak [92] also found that there was a good agreement between the experimental and theoretical results for AE signal frequencies and stress intensity factor during compact tension specimens made of aluminum alloys as shown in Fig.2.28.

2.5 Acoustic emission monitoring of mechanical testing

This section reviews that acoustic emission monitoring of mechanical testings such as tensile test and Charpy impact tests, and the application of the AE monitoring in gas pipeline.

2.5.1 AE monitoring during tensile test

A number of AE studies have been performed for tensile tests: i.e. detection the burst AE signal near yielding [10]; identification of AE activity originating from movement of dislocations [93], and AE wave parameters arising from macro-yielding [84]. Others researchers have studied the relationship between AE features (such as signal amplitude, frequency, energy, duration and count) and the parameters of mechanical testing (load, stress and crack growth) during tensile testing of notched and plain metal specimens [82, 85, 91, 94-96]. AE Energy along the stress-strain curve during tensile testing of Q345 steel is shown in Fig.2.29.

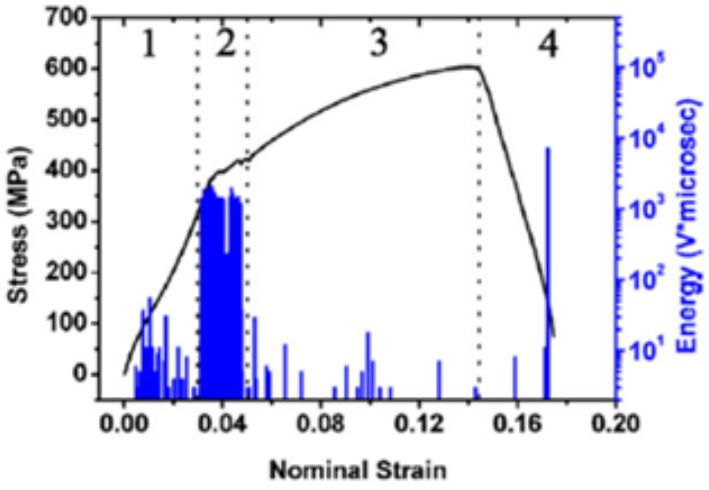

Fig.2.29 Stress Vs Strain and AE Energy [85].

It can be seen from Fig.2.29 that, the tensile process could be classified into four stages: (1) micro-plastic deformation, (2) yield, (3) strain hardening and (4) necking and fracture. Significant AE energy is expended in mainly the first and second stages during tensile testing. AE energy decreased in stage III and the density of AE activity increased at the final stage due to the occurrence of specimen fracture. These observation were common in metals [93, 97].

More studies confirmed that the AE count increased significantly around the yield point due to an increase in the movement of dislocations [98] and the initial stage of the deformation [99]. Fracture tests were carried out to detect AE signals associated with crack initiations [96, 100, 101] and crack growth in metals [83, 97, 102, 103]. AE activity observed during tensile testing of specimens of AISI 316 stainless steel has been analyzed to correlate the power spectra of various stages of plastic deformation [104]. It was found that the predominant frequency had a low value of 140 kHz obtained in the uniform deformation region of the stress-strain curve. In the necking region, the AE activity is associated with micro-void coalescence and crack growth, and is higher than the AE activity resulting from any dislocation.

Fig.2.30 presents the cumulative AE count, AE count rate, and stress versus strain relationship during a tensile test [105]. The cumulative AE count is the sum of the count of all AE events. The AE count rate is the time derivative of the AE cumulative count. The beginning portion of the linear elastic region is very quiet with low count rates and cumulative counts. This is associated with an incubation stage. The AE activity reaches its peak in the second stage right

before yielding occurs. After the material yields, the AE activity decreases, but is still detectable until the material fails.

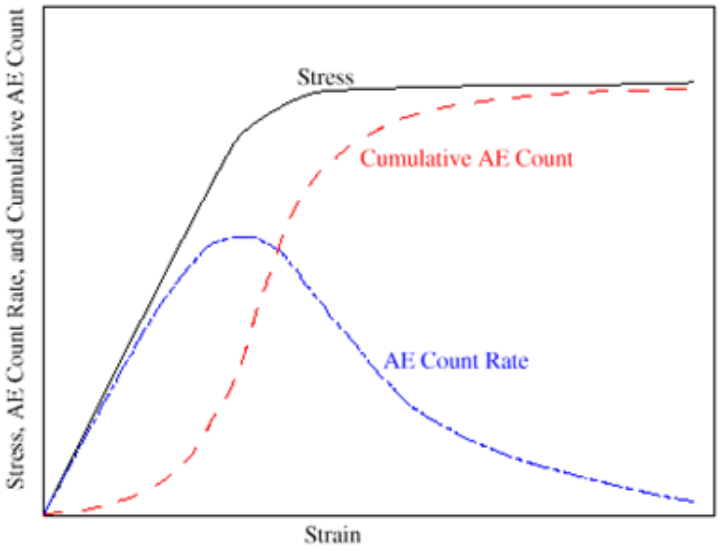

Fig.2.30 Stress, AE count Rate and Cumulative AE count vs Strain [105].

The effect of notched and unnotched specimens of stainless steel on acoustic emission was found in Ref. [84]. The purpose of the study was to investigate comparative analysis of AE activities from unnotched and notched specimens with varying notch lengths. The major observations were:

1) Acoustic activities in the region prior to and during yielding of the specimens with the presence of notches are higher compared to that in the unnotched specimens,
2) AE generated in the notched specimens in the region prior to and during yielding increases with increase in the notch length,
3) AE generated in both unnotched and notched specimens decreases with increase in nominal strain,

4) AE generated during necking elongation is more for the notched specimens than the unnotched specimens,

5) The relation between the AE total count and the stress intensity factor is linear in the logarithmic scale as shown in Fig.2.31. The exponent in $N=AK^m$ is found to lie between m=1.11–1.93.

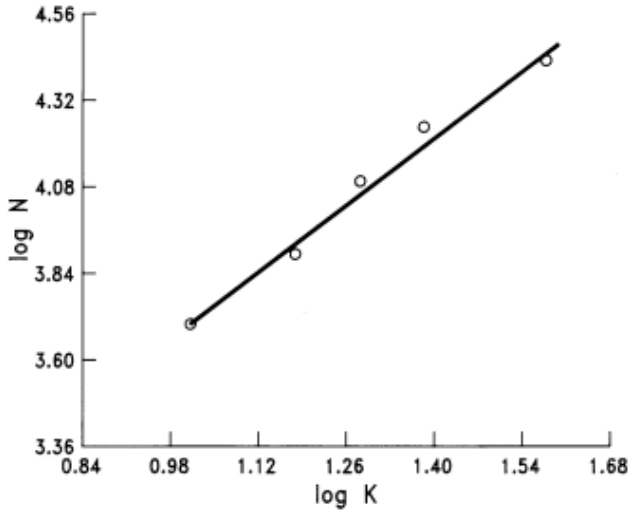

Fig.2.31 Acoustic emission count (N) Vs Stress intensity factor (K) [84].

2.5.2 AE monitoring during dynamic impact test

Weiss [106] and Ochiai [107] performed dynamic fracture toughness tests of high strength materials to study the AE signal resulting from crack initiation and propagation. It was found that emissions resulting from crack initiation and propagation in the brittle mode could be recorded using high-frequency transducers and that emission associated with plastic deformation could be recorded using low-frequency transducers. In other studies by Richter et al [108, 109] modified CVN specimens of 10CrMo 9 steel with 20 % side grooves were used to detect the onset of

tearing. They performed a dynamic three-point bending test using AE sensor coupled with an instrumented machine and located inside the hammer of the tester (Fig.2.32). This study investigated dynamic fracture behavior and determination of fracture initiation using the AE method. The main purpose of the investigation was to use the dynamic J integral (J_{id}) at crack initiation and dynamic yield stress (G_{yd}) for the characterization of elastic-plastic material behavior under rapid loading (impact).

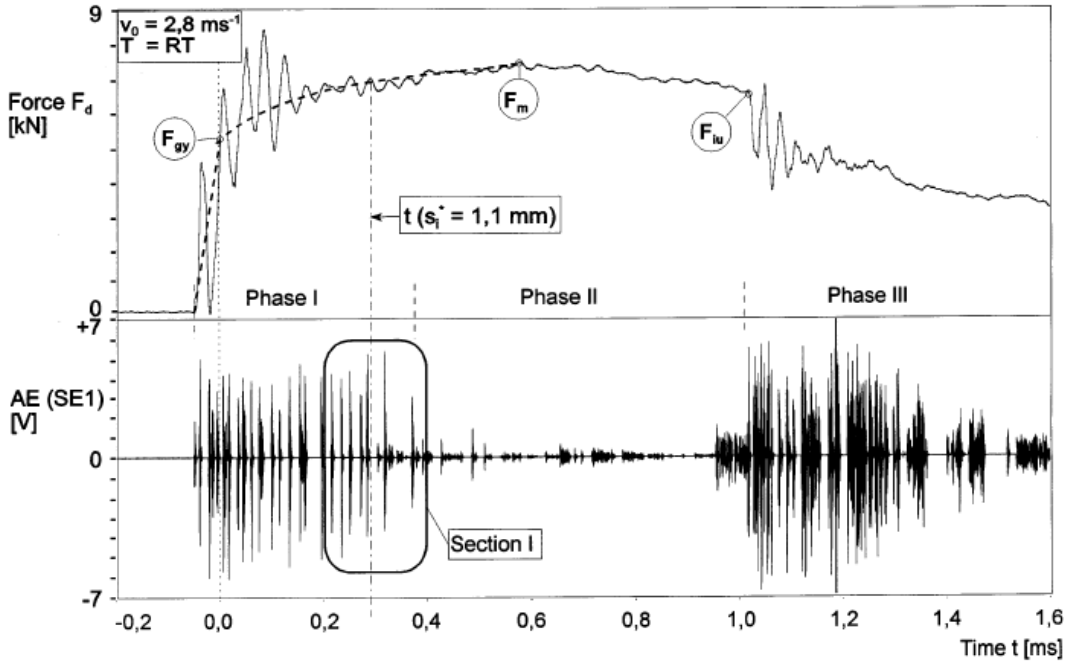

Fig.2.32 Load and AE signal from instrumented three point impact loading [108].

The possibility of detection of split formation during low-blow Charpy impact (40-100 Joules) testing was also shown for high strength steel by Kostryzhev et al. [9]. AE waveform analysis was carried out to separate signals generated from the hammer, plastic deformation and split initiation.Fig.2.33 shows acoustic waves and power spectra during testing of strip steel specimens at 60 J and 80 J impact energies. The AE waves were generated from split crack

initiation and growth in two peak amplitudes between 200-500 kHz and 500-1000 kHz. It is indicated by a shorter duration of the fracture process than that of deformation by dislocation slip.

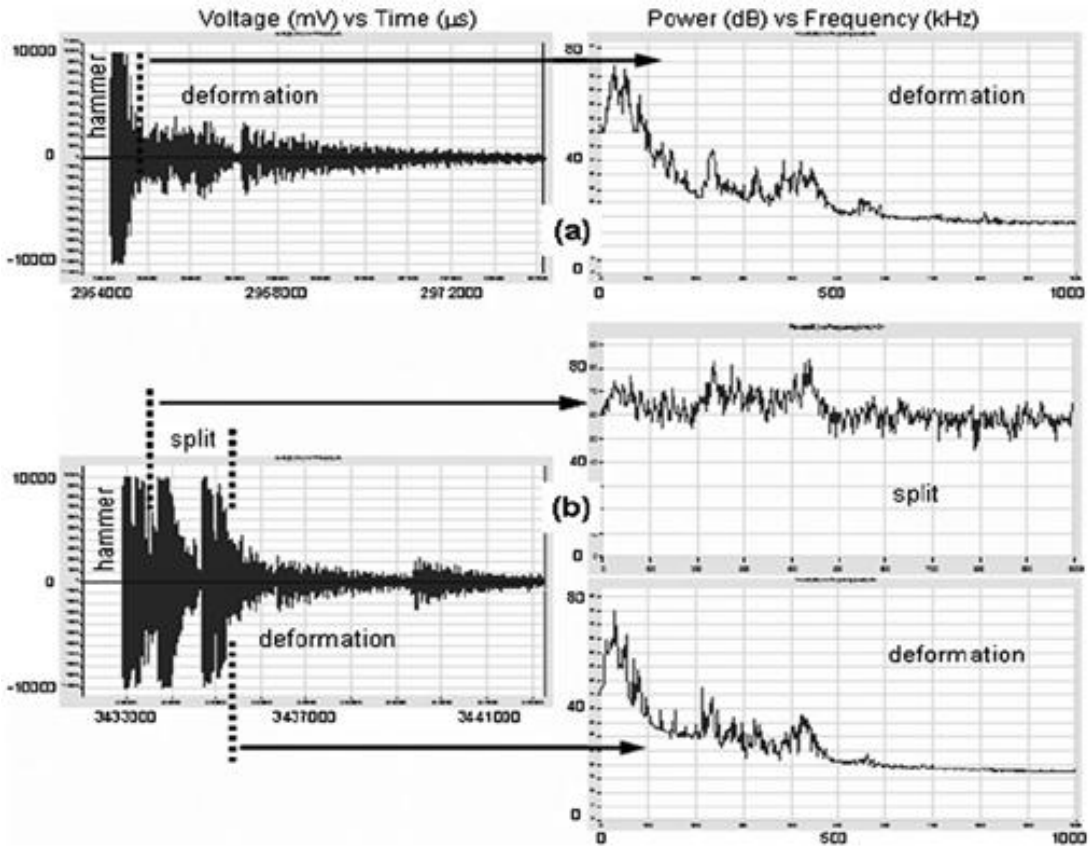

Fig.2.33 Acoustic emission during CVN at 60J and 80J impact energies [9].

Tronskar et al.[110] applied a different approach to determine the onset ductile tearing in instrumented Charpy testing of NVE 36 steel. A linear correlation was found between the time of ductile fracture initiation determined by the AE monitoring and direct displacement interferometric strip method. The AE signal was divided into three phases with respect to test duration. Phase I (frequency range 499 kHz to 693 kHz) was associated with strong oscillations,

friction and yielding. In contrast, ductile tearing occurred in Phase II (with a longer duration than Phase I; frequency range 400 kHz to 639 kHz). Phase III was related to brittle fracture which resulted in a higher AE peak amplitude than Phase II and the frequency ranging from 493 kHz to 278 kHz. Fig.2.34 shows load, AE and displacement curves at 0°C for CVN specimen.

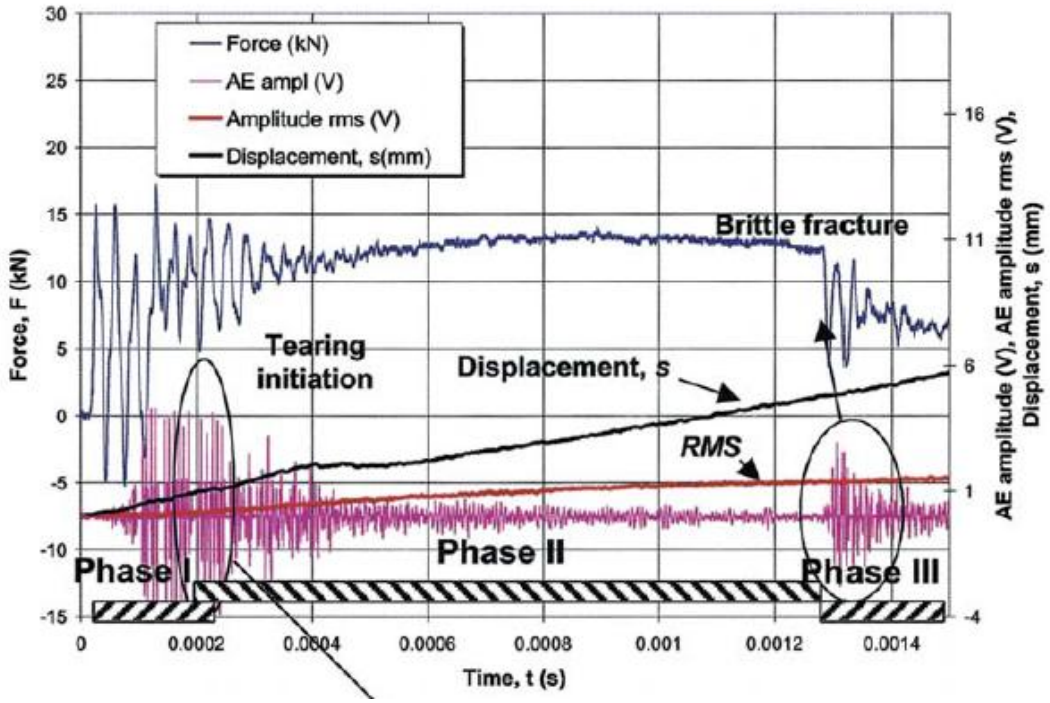

Fig.2.34 Load, AE Vs Time for CVN sample at 0°C [110].

2.5.3 AE study on pipeline steel

The possible use of AE monitoring to identify defects such as leaks and cracks in pipelines has been explored [111, 112]. Several experimental studies have demonstrated correlations between AE features and fracture of line pipe steels during tensile tests [61, 113] , compacting tests [114, 115], bending tests [116] and fatigue tests [103].

Ingram et al. [61, 117] studied the AE activity in a number of structural steels including X60 pipeline steel during tensile and bending tests. They observed significant effects of the yield deformation on AE activity and that an increased AE count could be obtained due to discontinuous yield. In general, the AE activity was found to increase with increasing strength and reducing toughness.

Ostby et al. [118] investigated the possibility of correlating the AE signal amplitude with cleavage (micro-crack) size during a three-point bending test on X65 line pipe steel. SEM imaging of the isolated cleavage area (micro-crack) for the X65 steel specimen showed that the corresponding AE signals had an amplitude of 60-110 dB.

Yusof et al. [103] studied AE activity of X70 pipeline steel subjected to fatigue. It was found that crack initiation was indicated by a rapid increase in the AE count value at positive peak stress.

Capelle et al. [119] compared the local fracture of pipeline steels such as X52, X70 and X100 using three-point bending tests to analyse the effect of hydrogen concentration on fracture while simultaneously recording AE. The AE technique was used to identify the onset of fracture. A study of the local strength of notched specimens in presence of hydrogen revealed the dependencies of the fracture initiation energy from the notch (U_i) and the total fracture energy for the specimen (U_f). Points on the ‘‘load–displacement’’ diagram, corresponding to fracture initiation and total fracture were identified on the basis of the AE analysis.

Almeida et al. [120] studied the behavior of high-strength and low strength line pipe steels during tensile testing using the AE technique. It was found that the AE signal can indicate local plastic deformation before the macroscopic yield for both types of steel and thus enabled detection of damage in the early stages of loading.

Drew et al. [113] used AE during tensile testing of X42, X60 and X65 line pipe steels. It was found that the amplitude of events was relatively small and the number of events was low. Most of AE activity detected at around yield was for high-strength X65 steel. It was observed that crack tip blunting and crack initiation of X65 steel could be identified due to a large increase in AE events with a burst-type waveform.

2.6 Summary

The main findings from the literature review can be summarized as follows:

1) Predicting the presence of defects in line pipe steel, as well as identifying crack initiation and propagation, are of crucial importance in fracture control of pipelines. To fully explain pipeline failure, research is needed to develop a better understanding of the mechanical properties of pipeline steel and fracture initiation and propagation in pipeline steels.
2) Numerical simulations of the CVN impact tests and SENT tests on line pipe steel can be performed using the commercial finite element software with the Gusron-Tveergaard-Needleman (GTN) constitutive model.

3) The AE technique can be applied to investigate defects in pipelines, and is more effective than other non-destructive techniques.
4) There are two types of AE analysis: parameter-based and waveform-based. A combination of both types of analysis is needed in the present research.
5) To date, there is no general theory that correlates frequency ranges with fracture mechanisms. This is due to the variation in fracture mechanisms with material, test types and AE data acquisition hardware.
6) During AE monitoring, separating the AE signal due to fracture initiation from background noise presents a major challenge. Such noise may be generated due to machine operation and the test environment.
7) The literature review indicates that quantitative dependences of AE parameters on the fracture parameters (e.g. brittle or ductile mode of propagation, crack growth rate, etc.) are not completely understood. Consequently, no recommendation exists to relate the AE parameters to the fracture parameters.
8) The relationship between the AE parameters (such as amplitude and frequency) and the fracture parameters during SENT tests (such as crack initiation and crack growth rate) has not received much attention.
9) The quantitative dependence of the AE parameters (such as amplitude and frequency) on fracture parameters during Charpy impact tests (such as ductile or brittle fracture mode, and fracture growth rate) is not yet fully understood.

3 MATERIALS AND EQUIPMENT

This chapter gives detailed information on the specimens and equipment used in this study.

3.1 Line pipe steels

Two grades of pipeline steels, API-X70 and API-X80, were used in this study. Their chemical compositions are shown in Table 3.1and

Table 3.2. All X70 specimens used in SENT and CVN tests were cut from a pipe with 14.1 mm wall thickness and 1067 mm diameter. All X80 specimens were prepared from a pipe with 25 mm wall thickness and 1067 mm diameter.

Table 3.1 Composition of X70 pipeline steel.

C	Mn	Si	Nb	Ti	V	Ni	Cr
0.0499	1.56	0.238	0.0576	0.0088	0.0256	0.214	0.028
Cu	Mo	Al	Ca	N	S	P	B
0.163	0.148	0.035	0.0015	0.0036	0.0014	0.0059	0.0001

Table 3.2 Composition of X80 pipeline steel.

C	Si	Mn	P	S	Cu	Alt	Nb	Ni	Cr	Ti	Ceq	Pcm
0.064	0.22	1.72	0.006	0.002	0.23	0.027	0.068	0.206	0.22	0.0158	0.42	0.18

The mechanical properties of the line pipe steels were obtained by tensile tests carried out in accordance with the Australian Standard AS 1391-2007: Metallic materials-Tensile testing at ambient temperature [121]. Fig.3.1 shows the stress-strain curves for the two materials and Table 3.3 lists the major mechanical properties.

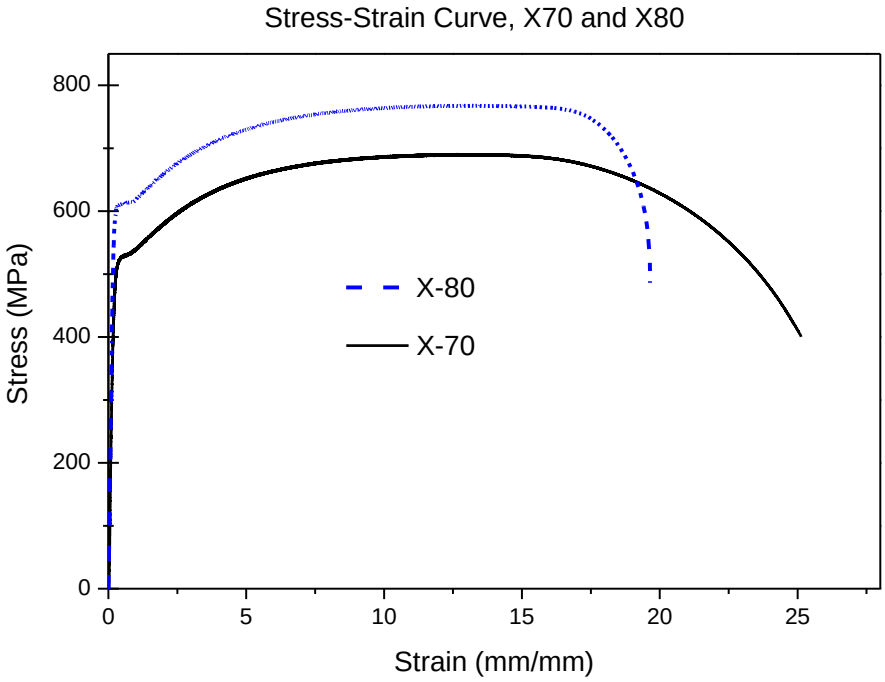

Fig.3.1 Stress-strain curve for X70 and X80 steels.

Table 3.3 Mechanical properties of X70 and X80 line pipe steel.

	Young modulus	Poisson ratio	Yield stress	Ultimate stress	Density
X 70	190 GPa	0.31	530 MPa	605 MPa	7710 kg/m^3
X 80	210 GPa	0.34	610 MPa	750 MPa	7780 kg/m^3

3.2 Single edge-notched tension (SENT) test

The SENT tests were carried out using an Instron 8801 servo hydraulic dynamic testing machine as shown in Fig.3.2. The machine has console software which provides full system control from a computer including waveform generation, calibration, limit set up, and status monitoring. The

testing system includes up to a 100 kN axial force capacity, a Dynacell load cell, standard height frame options and a wide range of grips, fixtures and accessories.

Fig.3.2 The Instron 8801 servo hydraulic dynamic testing machine.

Fig.3.3 shows the geometry of a SENT specimen conforming to DNV RP F108 specifications [43]. The geometries of specimens were 12 mm in width, 6 mm in thickness and 60 mm in gauge length and they had a notch representing an initial ‘crack’ of 2 mm in length and 0.3 mm in width. This ‘crack’ was cut using wire cutting. The crack (notch) depth was a third of the specimen thickness.

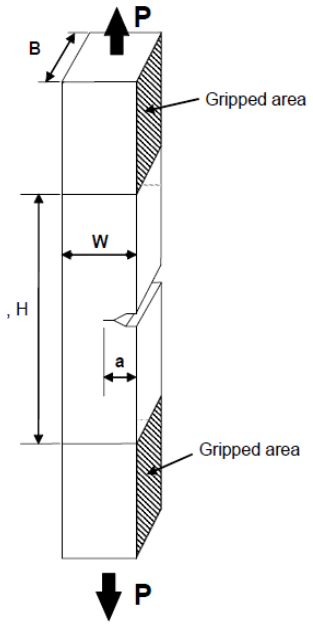

W (mm)	B (mm)	H (mm)	a (mm)	a/w
6	12	60	2	0.3

Specimen Geometry:

B- width

W- represent the pipe wall thickness (t)

a-Initial crack length

H- "Day-light between grips"

Requirement of the specimen geometer:

H=10W;

B=2W;

$0.2 \leq a/W \leq 0.5$;

If the reduction on wall thickness due to pipe dimension (D/t) will be more than 15% (w<0.85 t) the specimen width, B may be reduced but not to less than B≥W:

Fig.3.3 The geometry of a single-edge notched specimen used in this work.

3.3 Charpy V-notch (CVN) Impact test

In this study, the CVN impact tests were carried out using a 450MPX instrumented Instron Impact tester as shown in Fig.3.4. The capacity of this machine is 750 J. The load can be measured using a load cell in the striker, and the displacement is obtained from a transducer to

measure the rotation of the hammer. The absorbed energy is determined by measuring the difference in the hammer descent. The area under the load-displacement curve also gives the total energy consumed in the test. Fig.3.5 shows a typical load-displacement curve.

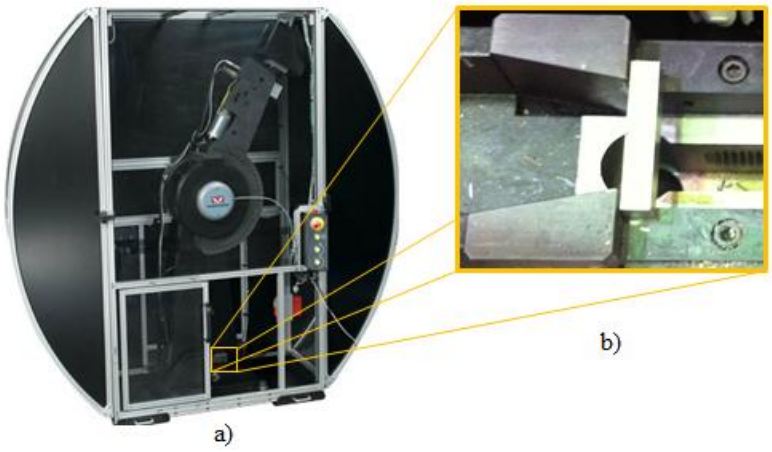

Fig.3.4 (a) 450MPX instrumented Instron Impact tester; (b) Charpy specimen location.

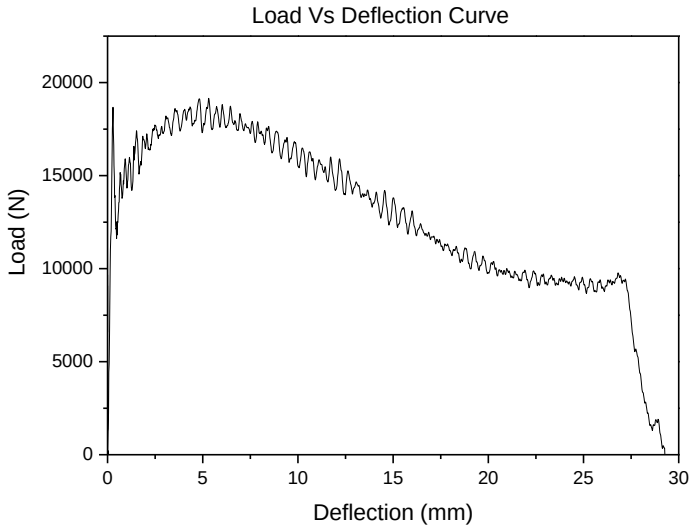

Fig.3.5 A typical load-deflection curve of an instrumented Charpy test.

The temperature of the specimen can be controlled by a cooler, as shown in Fig.3.6. The cooler used methanol to cool the specimen down to -80^{o}C and a mixture of liquid nitrogen and methanol to cool the specimen below -80^{o}C.

Fig.3.6 Charpy cooler.

3.4 AE instrumentation

Fig.3.7 shows the AE signal processor, manufactured by the Physical Acoustics Corporation (USA). The system consisted of a wideband sensor with an operating frequency range of 50 kHz to1000 kHz and an operating temperature range of -65^{o}C to +175^{o}C, a single-channel AE Digital Signal Processor with an internal low noise preamplifier and a USB connection to a computer [122].

Fig.3.7 A single-channel AE Digital Signal Processor.

The AE signal was recorded and analyzed using the AE Win software. This software has the ability to analyze waveforms, and conduct Fast Fourier Transforms (FFT). All data is saved in standard Physical Acoustics Corporation (PAC) defined DTA files for use with AE Win replay, AE Win POST and other PAC analysis programs.

3.5 High-speed camera

Redlake's MotionPro X camera was used in this study as shown in Fig.3.8. MotionPro X system has a wide variety of dynamic range options including a unique and proprietary extended dynamic range mode (XDR). They also feature excellent sensitivity and frame rates, including a 1280x1024 resolution at 1000 or 2,000 fps for superior resolution at high speeds. The camera is supplied in internal memory of 8GB and minimum shutter time is 1us (optional 100 ns). The cameras feature a USB 2.0 digital interface and Giga-Ethernet (1000 Mbps) that provides true and easy plug-and-play installation and capable of transfer at a high-speed rate to a desktop or laptop computer with a single cable.

Fig.3.8 High-speed camera.

3.6 Digital image correlation (DIC) system

The digital image correlation (DIC) system is an optical measuring device for non-contact and three dimensional measurements of shape, displacements and strains on components and structure made from materials [123]. The Dantec Digital image correlation system Q-400, as shown in Fig.3.9, was used in the study of SENT testing. The DIC system consisted of the DIC pair high speed cameras, illumination (red lights), electronic and timing-hub, tripod and fixations and software ISTRA 4D.

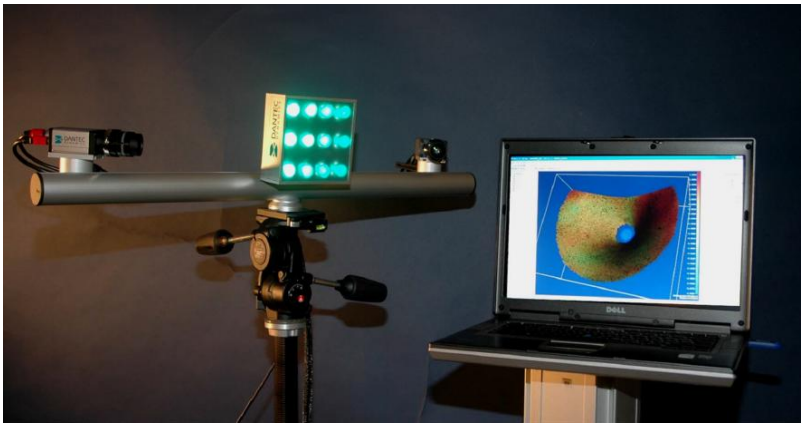

Fig.3.9 Digital image correlation apparatus.

Before testing, the specimens needed to be painted a white background and black dots on the surface for DIC software to identify and analyze the local displacement. The paint needed to be

matted and not shiny as this will affect the readability of the specimens by the DIC pair camera. A typical painted specimen is demonstrated in Fig.3.10.

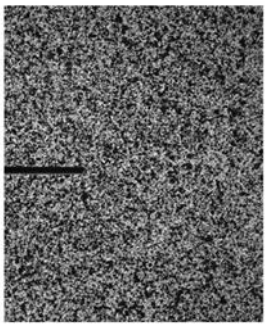

Fig.3.10 A typical spray-painted specimen for DIC measurement.

3.7 Scanning electron microscope (SEM)

The JEOL JSM-6490LA, as shown in Fig.3.11, is a high performance, scanning electron microscope with a maximum resolution of 3.0 nm [124]. Its asynchronous five-axis mechanically eccentric stage with compucentric rotation and tilt can accommodate a specimen of up to 8-inches in diameter (307.79 mm loadable). Standard automated features include Auto Focus/Auto Stigmator, Auto Gun (saturation, bias and alignment), and Automatic Contrast and Brightness.

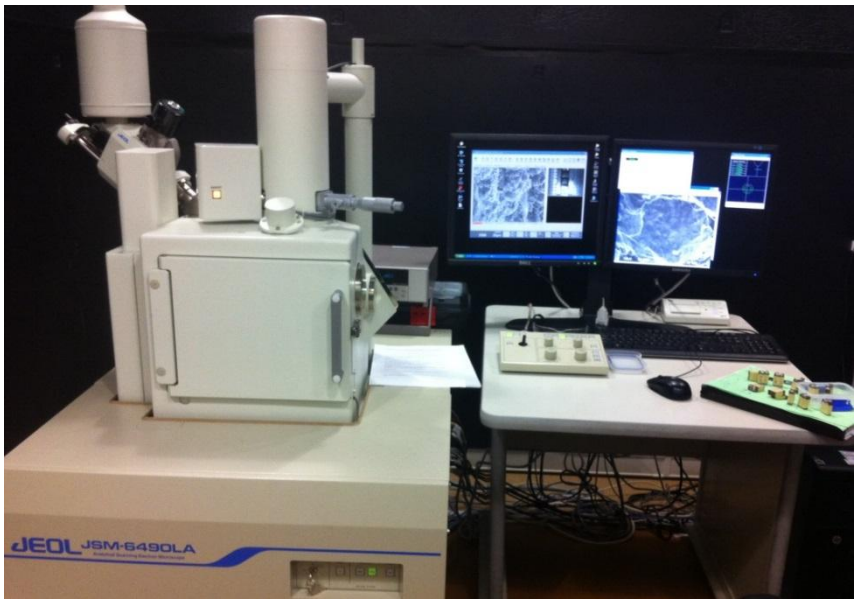

Fig.3.11 Scanning electron microscope (SEM).

3.8 FE software

In this study, the LS-DYNA explicit code was used to model the CVN and SENT tests. LS-DYNA is a general-purpose finite element program used to analyse the nonlinear dynamic response of three-dimensional structures[125]. This simulation model was developed in the LS-PREPOST, which is an advanced pre and post-processor that is delivered with LS-DYNA, and saved into a K file. The K file was then uploaded to a supercomputer to preform parallel FEM simulations. After the completion of the simulation, the results were downloaded to the PC and analysed by the LS-PREPOST.

4 ACOUSTIC EMISSION MONITORING OF SENT TEST

In this chapter, the fracture behaviour of the line pipe steel during single edge-notched tension (SENT) was investigated using the acoustic emission (AE) monitoring technique. The work of the chapter has been published in Material Science and Engineering A [126].

4.1 Experimental procedure

Seven groups of tests were carried out. They will be named Tests 1-7 in this chapter respectively. Each group of tests were repeated twice or three times. Only one typical result will be shown and discussed for each group of tests in the following sections. The conditions of all tests are shown in Table 4.1.

Table 4.1 Testing conditions.

Test number	Material grade	Test type	Temperature	Strain rate
1	X70	Plain tension	RT (20^{o}C)	5.5×10^{-3}
2	X70	SENT	RT (20^{o}C)	2.7×10^{-4}
3	X70	SENT	RT (20^{o}C)	5.5×10^{-3}
4	X70	SENT	-20^{o}C	5.5×10^{-3}
5	X80	SENT	RT (20^{o}C)	2.7×10^{-4}
6	X80	SENT	RT (20^{o}C)	2.7×10^{-3}
7	X80	SENT	RT (20^{o}C)	5.5×10^{-3}

Note: RT means room temperature

The geometry of the SENT samples has been described in Section 3.2. The sample used in Test 1 (Plain tension test) had the same geometry as the SENT sample, but it didn't have the pre-

machined notch. Test 2, Test 5 and Test 6 adopted a slower strain rate of $2.7x10^{-4}$ compared to the strain rate of 5.5×10^{-3} in other tests. Test 4 was conducted at a lower temperature of -20°C, while other tests were performed at room temperature (approximate 20°C). The material used in Tests 1-4 was X70 line pipe steel while the material in Test 5, Test 6 and Test 7 were X80 line pipe steel. X70 specimens were cut using wire cutting from a 14 mm wall thickness, 1067 mm diameter pipe. X80 specimens were cut from a 25 mm wall thickness, 1067 mm diameter pipe.

The experimental set up is shown in Fig.4.1. The tests were carried out in an Instron testing machine described in Section 3.2. The AE monitoring system and high speed camera were used in all the tests. During the tests the load was measured by the Instron machine and the extension (displacement) of the specimen was measured by a 50 mm gauge length extensometer.

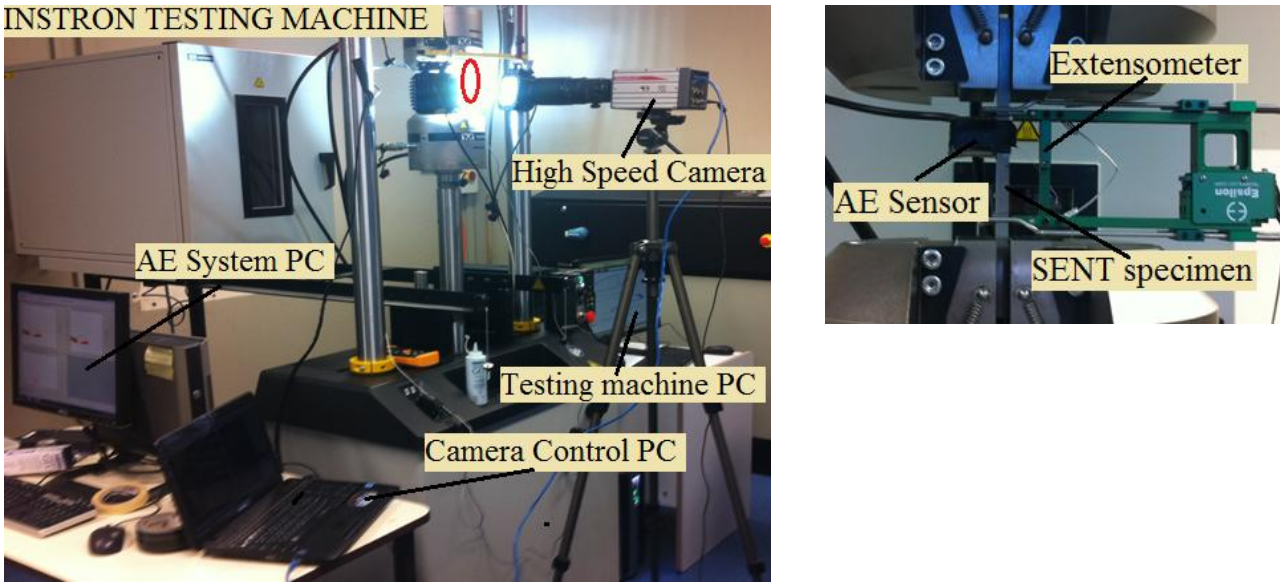

Fig.4.1 The experimental setup of the tensile testing.

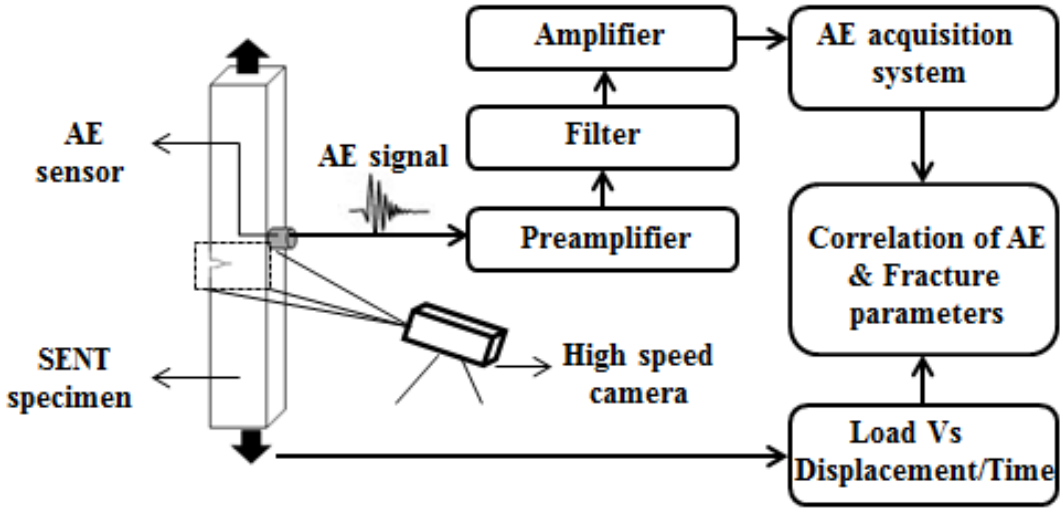

Fig.4.2 A Schematic of AE measurement setup of SENT testing.

A schematic of AE measurement setup of SENT testing is illustrated in Fig.4.2. During testing the AE sensor was attached to the specimen using a sticky band with ultrasound treatment gel applied between the specimen and sensor surfaces as a coupling material to increase the signal quality. All the recorded waveforms were analyzed in time and frequency domain (frequency spectrum) using Fast Fourier Transform (FFT). The crack propagation during the SENT testing was observed using a MotionPro X3 high speed camera with excellent resolution, up to 8500 µs exposure time and up to 300 of frame/sec recording rate. After testing the fracture surface was observed by JEOL JSM-6490LA SEM operating at 20 kV.

Additionally, the SENT test of X80 line pipe steel (Test 5) was also recorded simultaneously by AE monitoring technique and Digital image correlation (DIC) method. The DIC method was used to evaluate and measure plastic deformation around the notch and to confirm and monitor the fracture process on the specimen surface.

4.2 Experimental results

4.2.1 Test 1

Fig.4.3 shows the load-displacement curve of Test 1. The load linearly increases with the displacement at the early stage of deformation, namely elastic deformation, and then the specimen yields at the displacement of about 1.5 mm. The yield point is determined by 0.2% offset method. As the deformation proceeds further the specimen is subject to plastic deformation. During the period of plastic deformation, the load still increases with displacement, but the slope of the curve decreases. At the displacement of about 11 mm, the load reaches its maximum value, followed by a decrease of the load until the end of the test.

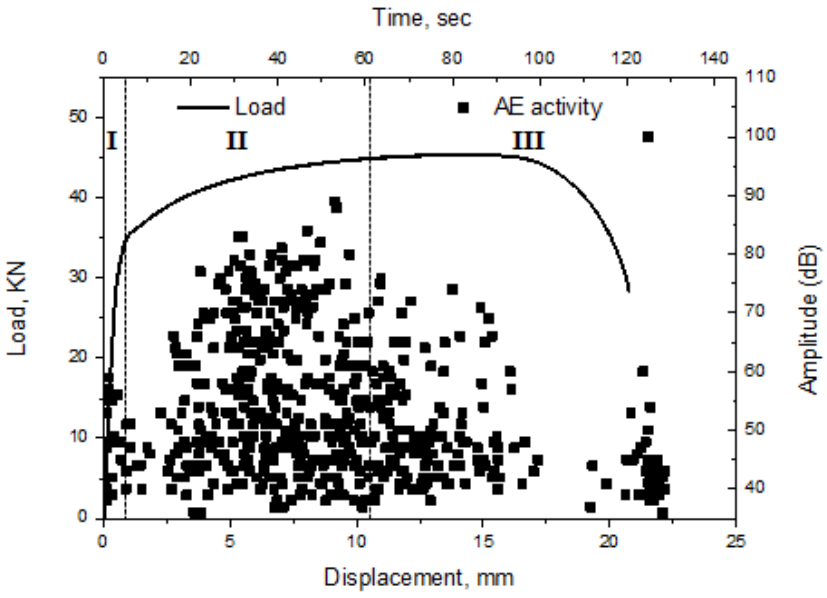

Fig.4.3 Load-displacement curve, AE amplitude for Test 1.

Fig.4.4 (a) shows the recorded AE signals in Test 1. A large number of hits can be observed in the figure. Three hits with higher amplitude values have been marked in Fig.4.4 (a). They are

named as Hit A, Hit B and Hit C, respectively. The detailed signals of these three hits are given in Fig.4.4 (b), (c) and (d), respectively. Hit A and Hit B are typical burst signals. They start with a large amplitude and then the amplitude decays towards the threshold within a very short period. Hit C also consists of burst signals. However most of its peak values have exceeded the measurement limit.

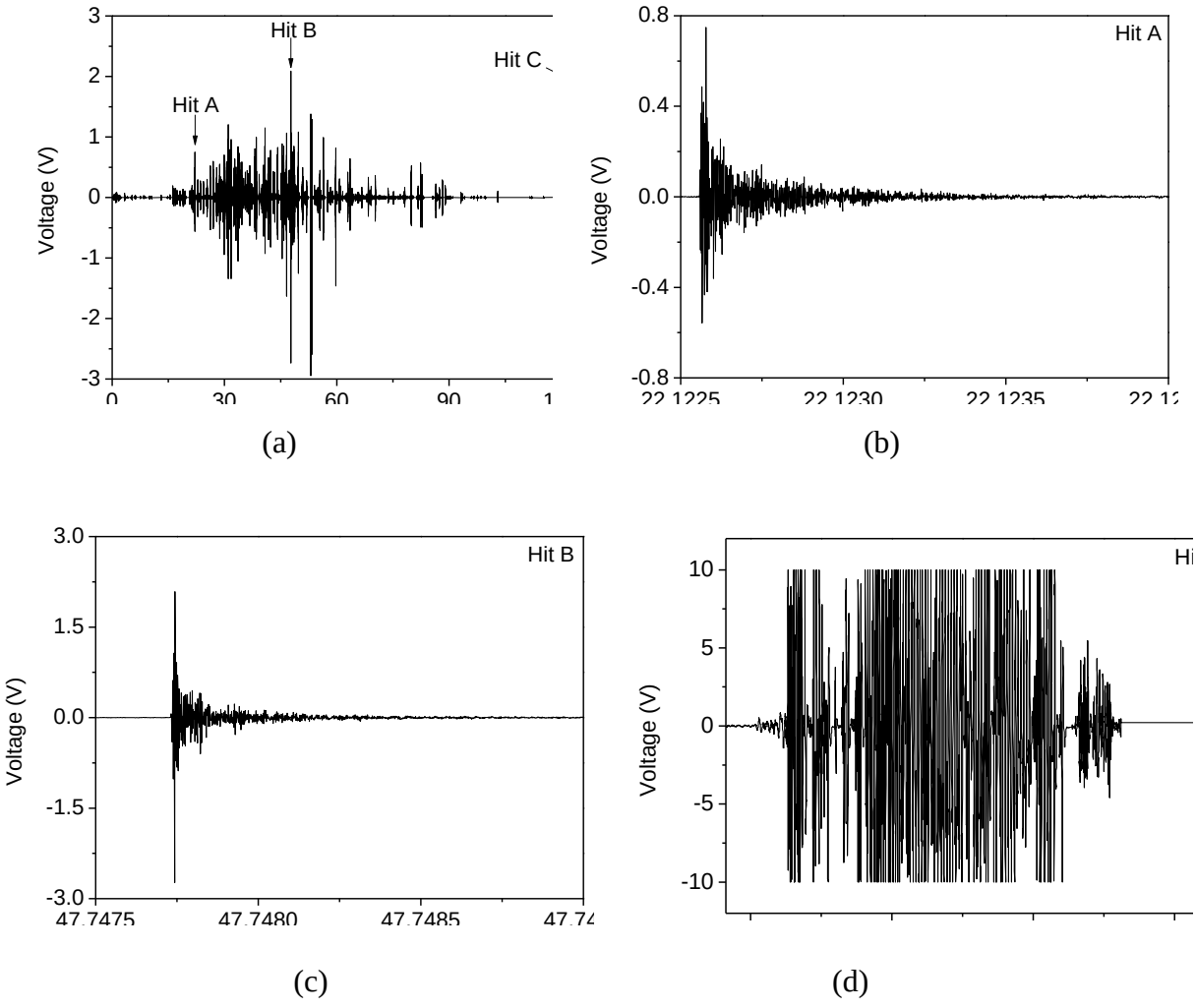

Fig.4.4 AE signals of Test 1.

(a) whole AE waveform; (b) waveform of Hit A; (c) waveform of Hit B; (d) waveform of Hit C.

The amplitude and average frequency have been calculated for each hit and the results are displayed in the same figure as the load-displacement curve (Fig.4.3). The load-displacement curve can be divided into three regions as marked in the figure:

1) Region I. This region is located before the yield point. Several AE hits with lower amplitudes have been observed in this region. It is well known that these AE hits are related to the elastic deformation and dislocation activities.
2) Region II. This region is located between the yield point and the point with the maximum load. There are a large number of hits in this region. The maximum amplitude is 85 dB while the average frequency ranges from 150 kHz to 250 kHz. These hits are believed to be caused by plastic deformation and fracture behavior. The detailed discussion will be conducted in Section 4.3.3.
3) Region III. This region is located after the maximum load point. The AE activity in this region decreases compared to Region II. The AE amplitude is up to 100 dB and the average frequency is in the 100-150 kHz range. Necking is responsible for most AE activity in this region. There are several extremely strong hits, including Hit C, at the end of Test 1. This is due to the final separation of material in the test.

4.2.2 Test 2

The load-displacement curve of Test 2 is shown in Fig.4.5. Test 2 was a SENT test. The specimen had a pre-machined notch. Therefore, the total displacement to failure is much smaller than Test 1 as shown in Fig.4.3. The material yields at the displacement of about 0.4 mm and reaches the maximum load at the displacement of 1.5 mm. After the peak point the load

gradually decreases. Beyond the displacement of 2.5 mm, the slope of the load-displacement curve decreases.

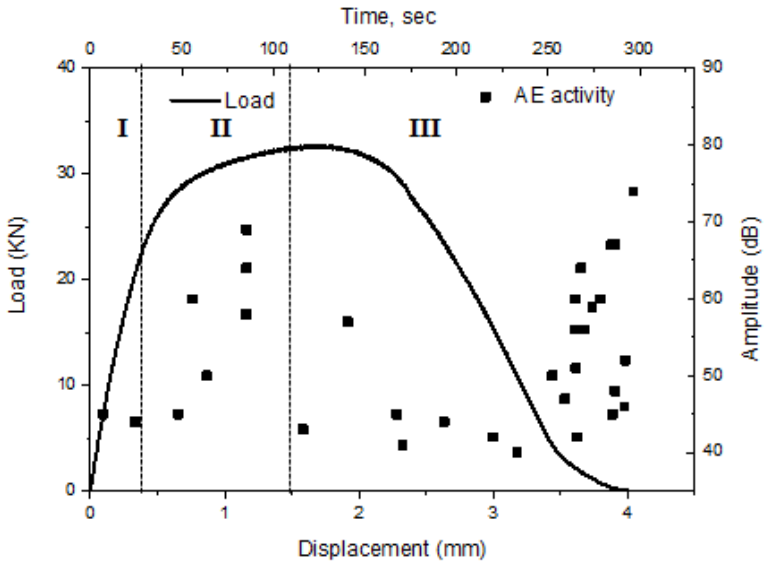

Fig.4.5 Load-displacement curve, AE amplitude for Test 2.

Fig.4.6 (a) shows the recorded AE signals in Test 2. Compared to Test 1 (Fig.4.4 (a)), less hits are observed in Fig.4.6 (a). Three hits, Hits A, B and C marked in Fig.4.6 (a), have been selected. Their signals are detailed in Fig.4.6 (b), (c) and (d), respectively. It is clear that all three hits are burst signals. The maximum voltage of Hit C is much higher than other two hits.

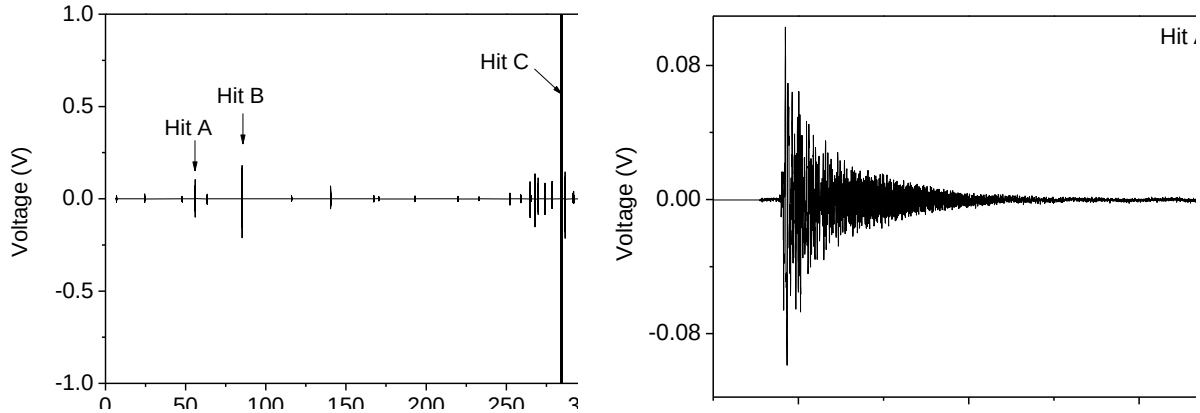

(a) (b)

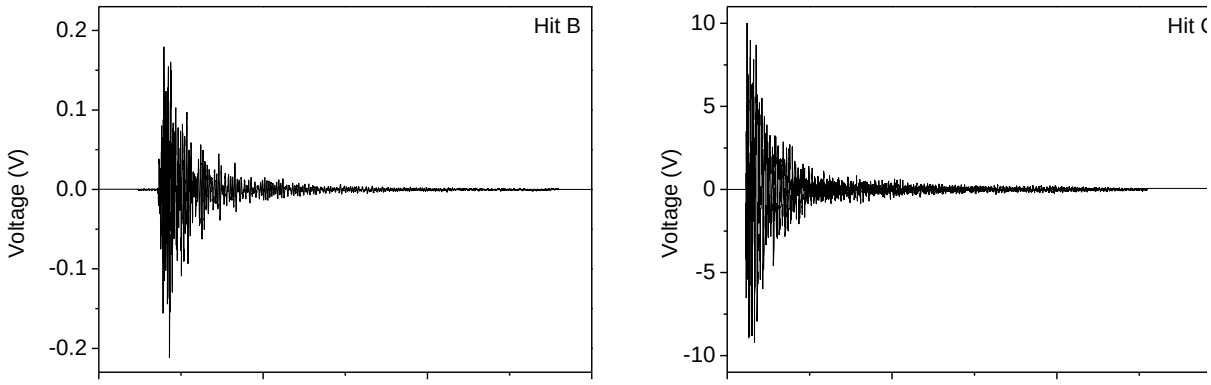

(c) (d)

Fig.4.6 AE signals of Test 2.

(a) whole AE waveform; (b) waveform of Hit A; (c) waveform of Hit B; (d) waveform of Hit C

The amplitude and average frequency are calculated from the AE signals. The calculated results are displayed in company with the load-displacement curve in Fig.4.5. Similar to Test 1, the load-displacement curve can be divided into three regions as marked in Fig.4.5.

1) Region I. There are several hits in this region. The maximum amplitude is 45 dB and the average frequency varies from 80 to 100 kHz.
2) Region II. The AE activity increased compared to Region I. There are 7 hits in this region. The maximum amplitude is 70 dB and the average frequency ranges from 100 to 350 kHz.
3) Region III. The AE activity is stable in accordance with the monotonous crack propagation. At the end of this region the AE hit density increases following occurrence of the multiple fracture events before separation of two parts of the specimen. The main

AE signals observed in this region are of an amplitude of up to 75 dB and average frequency of 200-400 kHz.

4.2.3 Test 3

The load-displacement curve of Test 3 is shown in

Fig.4.7. This curve looks similar to that of Test 2. Test 3 had a lower strain rate of $2.7x10^{-4}$ while Test 2 had a higher strain rate of $5.5x10^{-3}$. The effect of strain rate on the load-displacement curve will be discussed in Section 4.3.1. Fig.4.8 shows the waveforms of AE in Test 2.

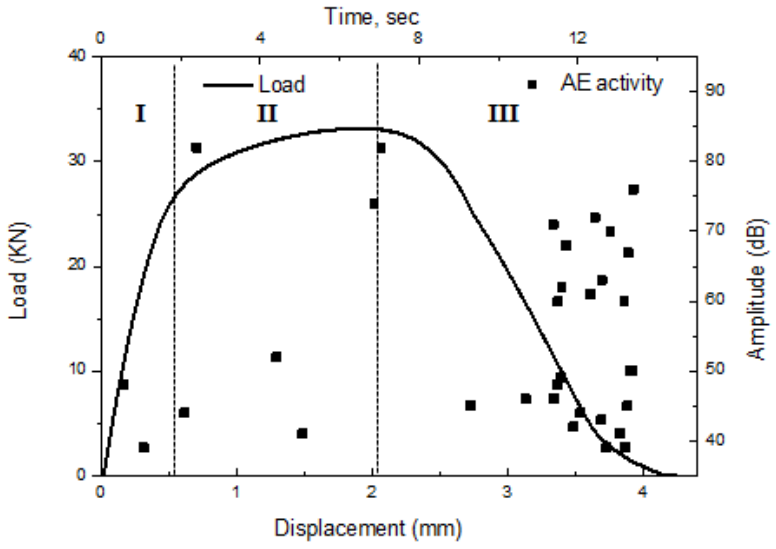

Fig.4.7 Load-displacement curve, AE amplitude for Test 3.

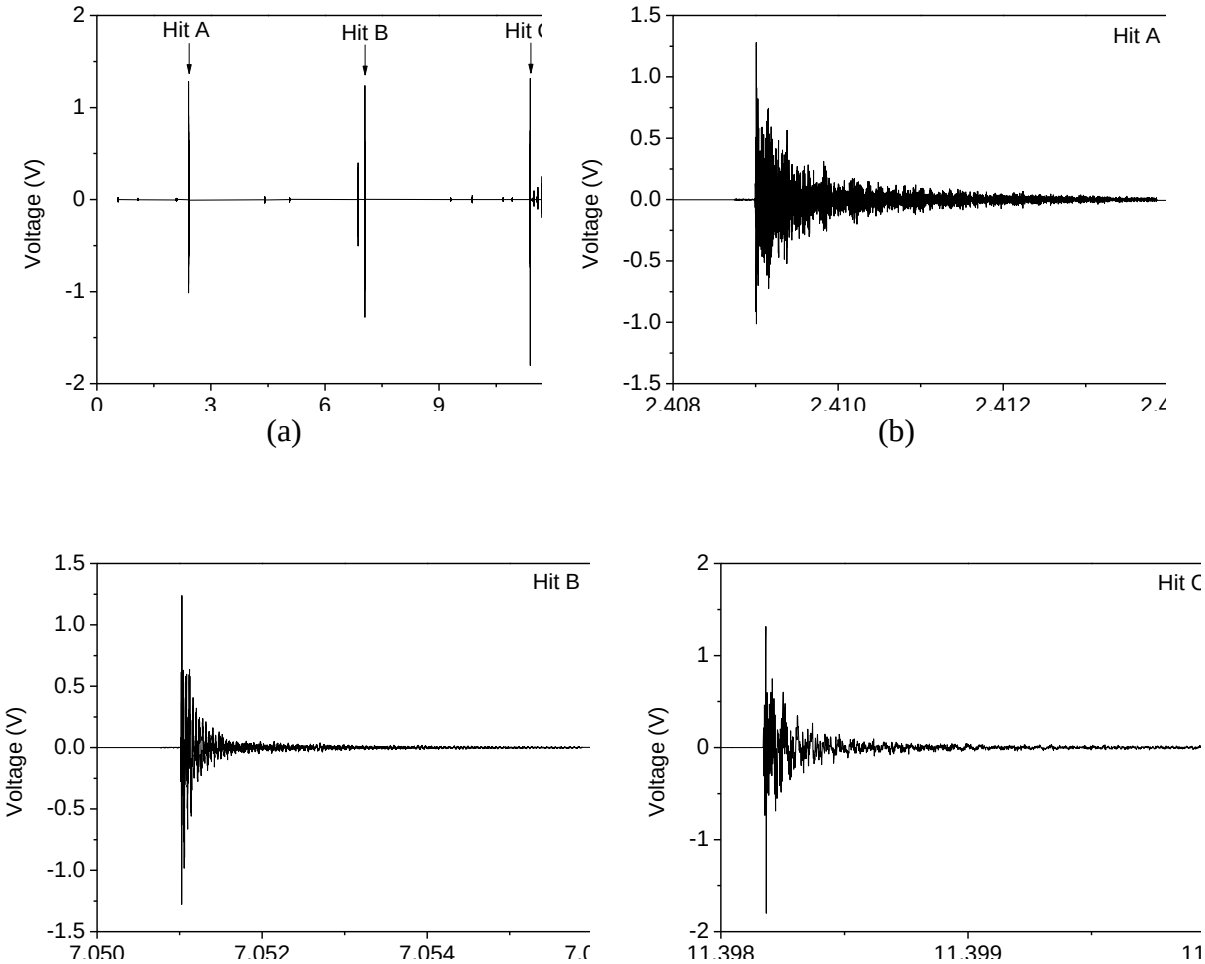

Fig.4.8 AE signals of Test 3.

(a) Whole AE waveform; (b) waveform of Hit A; (c) waveform of Hit B; (d) waveform of Hit C.

Fig.4.7 shows the amplitude and average frequency in company with the load-displacement curve. It can be observed that

1) Region I. There are 2 hits in this region. The maximum amplitude is 50dB and the average frequency varies from 50 to 150 kHz.
2) Region II. The AE activity increases compared to Region I. There are 5 hits in this region. The maximum amplitude is 80 dB and the average frequency ranges from 50 to 400 kHz.
3) Region III. The AE activity is stable in accordance with the monotonous crack propagation. At the end of this region the AE hit density increases following occurrence of the multiple fracture events before separation of two parts of the specimen. The main AE signals observed in this region are of an amplitude of up to 75 dB and average frequency ranges from 100-350 kHz.

4.2.4 Test 4

The load-displacement curve of Test 4 is shown in Fig.4.5. Test 4 is a SENT tested at -20^{o}C. The total displacement to failure is similar to Test 3 as shown in Fig.4.7. The material yields at the displacement of about 1.4 mm and reaches the maximum load at the displacement of 4.5 mm. After the peak point the load gradually decreases. Beyond the displacement of 3.1 mm, the slope of the load-displacement curve decreases.

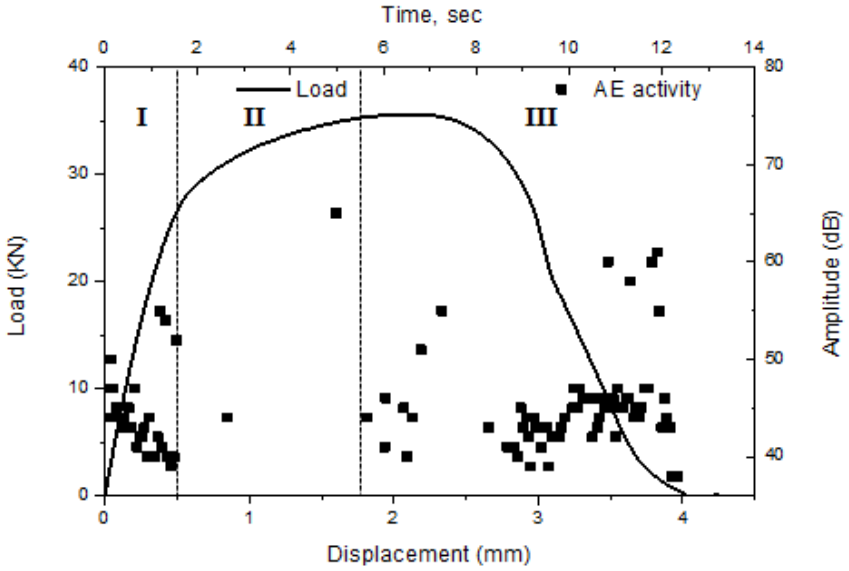

Fig.4.9 Load-displacement curve, AE amplitude for Test 4.

Fig.4.10 (a) shows the measured AE signals in Test 4. Compared to Test 3 (Fig.4.8 (a)), more hits are observed in Fig.4.10 (a). Three hits, Hits A, B and C marked in the figure, have been selected. Two of AE signals are detailed in Fig.4.6 (b), (c) and (d), respectively.

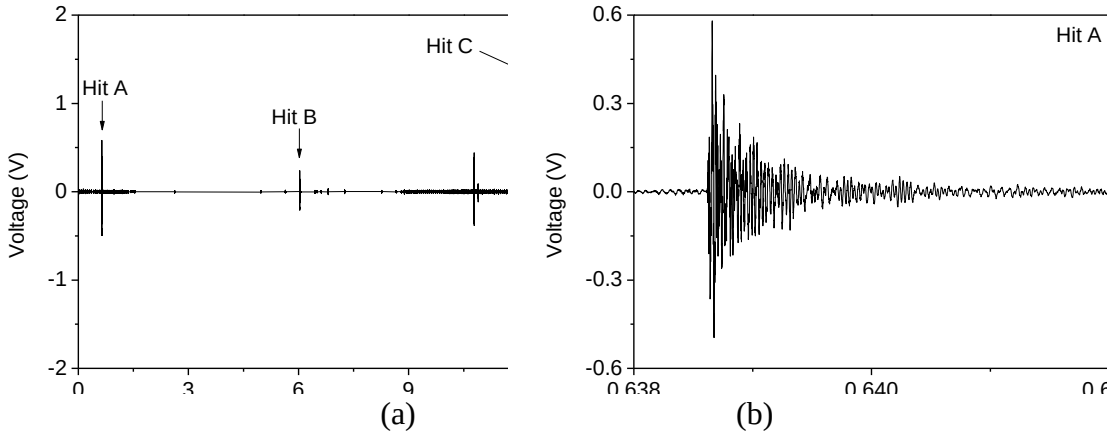

(a) (b)

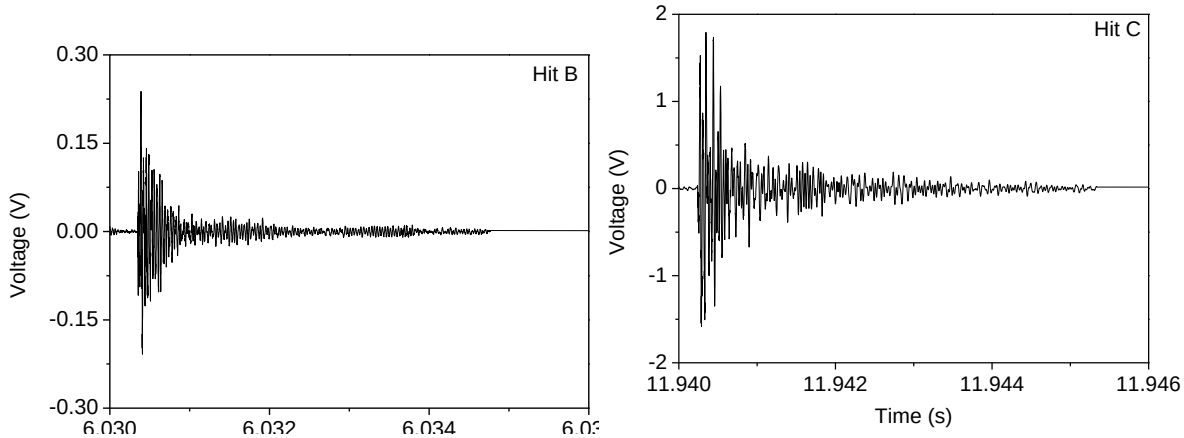

(c) (d)

Fig.4.10 AE signals of Test 4.

(a) whole AE waveform; (b) waveform of Hit A; (c) waveform of Hit B; (d) waveform of Hit C

Fig.4.9 shows the amplitude and average frequency in company with the load-displacement curve. It can be observed that

1) Region I. There are many hits in this region. The maximum amplitude is 50dB and the average frequency varies from 50 to 150 kHz.
2) Region II. The AE activity decreases compared to Region I. There are 3 hits in this region. The maximum amplitude is 65 dB and the average frequency ranges from 100 to 350 kHz.
3) Region III. The AE activity is stable in accordance with the monotonous crack propagation. At the end of this region the AE hit density increases following occurrence of the multiple fracture events before the separation of two parts of the specimen. The main AE signals observed in this region are of an amplitude of up to 60 dB and average frequency ranges from 100-300 kHz.

4.2.5 Test 5

The load-displacement curve of Test 5 is shown in Fig.4.11. Test 5 is a SENT of X80 line pipe steel at a strain rate of $2.7x10^{-4}$ s^{-1}.

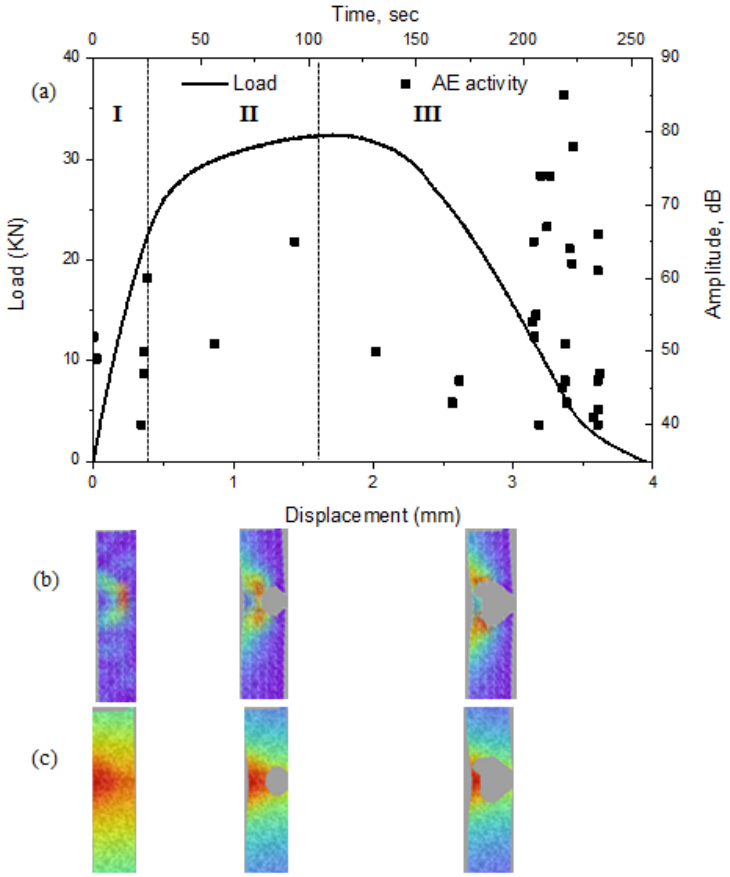

Fig.4.11 Load-displacement curve, AE amplitude for Test 5.

Fig.4.12 (a) shows the measured AE signals in Test 5. Compared to Test 2 (Fig.4.8 (a)), more hits are observed in Fig.4.10 (a). Three hits, Hits A, B and C marked in Fig.4.12 (a), have been plotted. Three of AE signals are detailed in Fig.4.6 (b) (c) and (d), respectively.

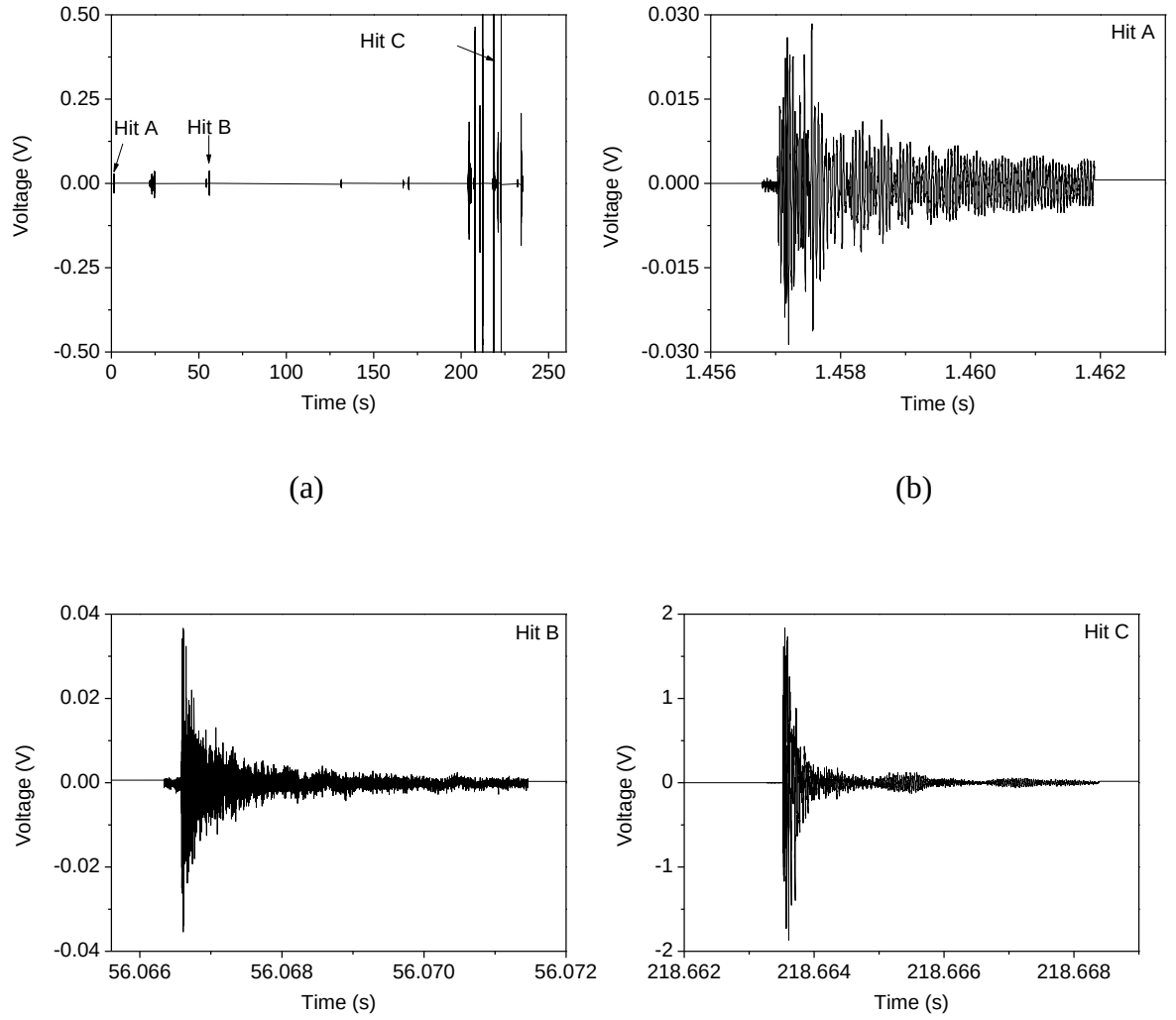

Fig.4.12 AE signals of Test 5.

(a) Whole AE waveform; (b) waveform of Hit A; (c) waveform of Hit B; (d) waveform of Hit C.

Fig.4.11 shows the amplitude and average frequency in company with the load-displacement curve. It can be observed that

1) Region I. There are 6 hits in this region. The maximum amplitude is 60dB and the average frequency varies from 50 to 150 kHz.

2) Region II. The AE activity decreases compared to Region I. There are 2 hits in this region. The maximum amplitude is 65 dB and the average frequency ranges from 100 to 300 kHz.

3) Region III. The AE activity is relatively stable due to the monotonous crack propagation. The main AE signals observed in this region are of an amplitude of up to 80 dB and average frequency ranges from 100-300 kHz.

4.2.6 Test 6

The load-displacement curve of Test 6 is shown in Fig.4.13. Test 6 was a SENT test of X80 at a lower strain rate of $2.7x10^{-3}$ s^{-1}. The specimen had a pre-machined notch. The material yields at the displacement of about 0.5 mm and reaches the maximum load at the displacement of 1.3 mm. After the peak point the load gradually decreases. Beyond the displacement of 2.2 mm, the slope of the load-displacement curve decreases.

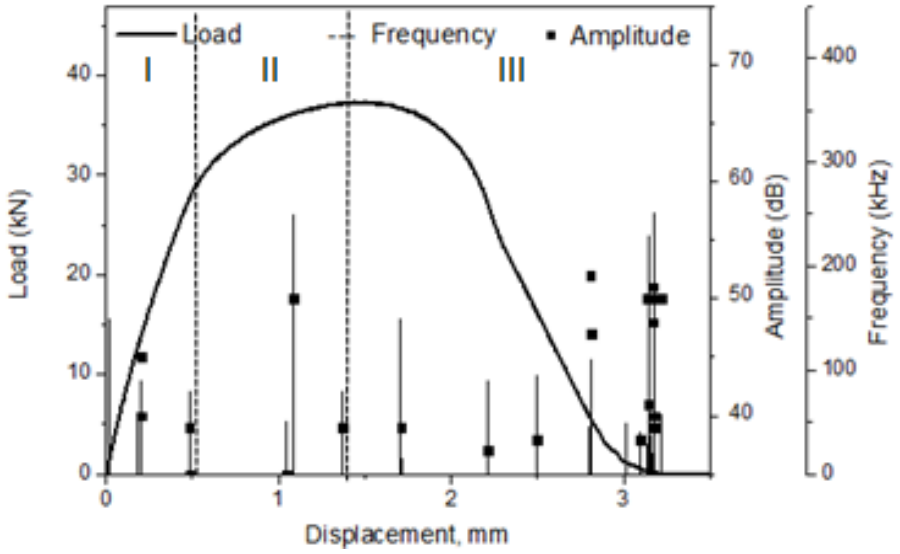

Fig.4.13 Load-displacement curve, AE amplitude and Average frequency for Test 6.

Fig.4.13 shows the amplitude and average frequency in company with the load-displacement curve. It can be observed that

1) Region I. There are 3 hits in this region. The maximum amplitude is 45 dB and the average frequency varies from 50 to 100 kHz.
2) Region II. The AE activity decreases compared to Region I. There are 2 hits in this region. The maximum amplitude is 50 dB and the average frequency ranges from 50 to 200 kHz.
3) Region III. The AE activity is stable due to the monotonous crack propagation. However, the relatively strong AE signals are detected at the final stage of the test. These AE hits are related to unstable crack propagation and final separation of the sample. The main AE signals observed in this region are of an amplitude of up to 55 dB and average frequency ranges from 100-200 kHz.

4.2.7 Test 7

The load-displacement curve of Test 7 is shown in Fig.4.14. Test 7 is a SENT of X80 line pipe steel at a strain rate of $5.5x10^{-3}$. Test 6 had a lower strain rate of $2.7x10^{-3}$ while Test 7 had a higher strain rate of $5.5x10^{-3}$. The effect of strain rate on the load-displacement curve for X80 will be discussed in Section 4.3.1.

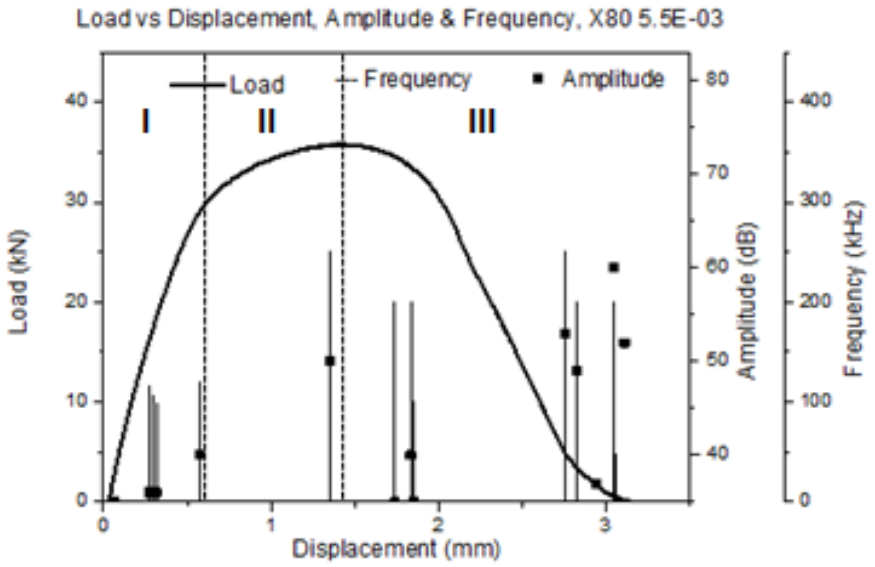

Fig.4.14 Load-displacement curve, AE amplitude and Average frequency for Test 7.

Fig.4.14 shows the amplitude and average frequency in company with the load-displacement curve. It can be observed that

1) Region I. There are 2 hits in this region. The maximum amplitude is 40 dB and the average frequency is 100 kHz.
2) Region II. The AE activity relatively decreases compared to Region I. The maximum amplitude is 50 dB and the average frequency is 250 kHz.
3) Region III. The AE activity increases at the final stage of the test These AE hits are related to unstable crack propagation and final separation of the sample. The maximum amplitude of up to 60 dB and average frequency ranges from 100 to 250 kHz.

4.3 Discussion

The load-displacement curves and the AE results have been given in Section 4.2 for all the tests. The load at yield and the maximum load are collected from the curves and listed in Table 4.2. Table 4.3 lists the ranges of both amplitude and frequency for each of three regions for all the tests.

Table 4.2 Load at yield and maximum load.

Test No.	Strain rate [s^{-1}]	Steel grade	Temperature [^{0}C]	Load at Yield [N]	Maximum Load [N]
1	5.5×10^{-3}	X70	ambient	34575.25	44815.25
2	2.7×10^{-4}	X70	ambient	27170.99	31500.15
3	5.5×10^{-3}	X70	ambient	28885.99	33812.66
4	5.5×10^{-3}	X70	-20	29391.39	36131.12
5	2.7×10^{-4}	X80	ambient	27275.15	32185.14
6	2.7×10^{-3}	X80	ambient	27955.19	34959.85
7	5.5×10^{-3}	X80	ambient	28945.86	35085.34

Table 4.3 The waveform parameters during tensile tests in the studied steels**.**

Test No.	Loading conditions (Strain rate & temperature)	Region	Amplitude [dB]	FFT power spectrum frequency peak [kHz]	Suggested cause of AE
1	5.5×10^{-3} at +20 ^{o}C (X70)	I	<60	100-150	Elastic (straining)
		II	40-80	100-250	Plastic deformation
		III	50-70	150-400	Necking and final fracture of the specimen.
2	2.7×10^{-4} s^{-1} at +20 ^{o}C (X70)	I	30-40	50-100	Elastic (straining)
		II	<30	100-300	Plastic deformation (dislocation)
		III	>40	150-350	Crack growth (void coalescence)
3	5.5×10^{-3} s^{-1} at +20 ^{o}C (X70)	I	>40	70-120	Elastic (straining)
		II	<40	150-400	Plastic deformation (dislocation)
		III	>45	150-350	Crack growth (void coalescence)
4	5.5×10^{-3} s^{-1} at -20 ^{o}C (X70)	I	40-55	50-200	Elastic
		II	>50	200-350	Plastic deformation
		III	40-60	100-300	Crack growth (void coalescence)
5	2.7×10^{-4} at +20 ^{o}C (X80)	I	<40	100-250	Elastic (straining)
		II	50-65	200-250	Plastic deformation (dislocation)
		III	40-75	150-350	Crack growth (void coalescence)
6	2.7×10^{-3} at +20 ^{o}C (X80)	I	<45	50-100	Elastic (straining)
		II	50	100-200	Plastic deformation (dislocation)
		III	55	100-200	Crack growth (void coalescence)
7	5.5×10^{-3} s^{-1} at +20 ^{o}C (X80)	I	<40	50-100	Elastic (straining)
		II	55	200-250	Plastic deformation (dislocation)
		III	<60	100-200	Crack growth (void coalescence)

4.3.1 Effect of strain rate

4.3.1.1 X70 line pipe steel

Fig.4.15 compares the load-displacement curves of two cases (Test 2 and Test 3) with different strain rates: 2.7×10^{-4} s^{-1} and 5.5×10^{-3} s^{-1}. Both tests of X70 were carried out at ambient temperatures. It can be seen that the two curves superpose up to the displacement of 1.65 mm. After this critical displacement, the load of the slower deformation (2.7×10^{-4} s^{-1}) decreases while the load of the faster deformation (5.5×10^{-3} s^{-1}) still increases for a certain displacement and then decreases. Beyond the displacement of 1.65 mm, the load of 5.5×10^{-3} s^{-1} is always higher than that of 2.7×10^{-4} s^{-1}.

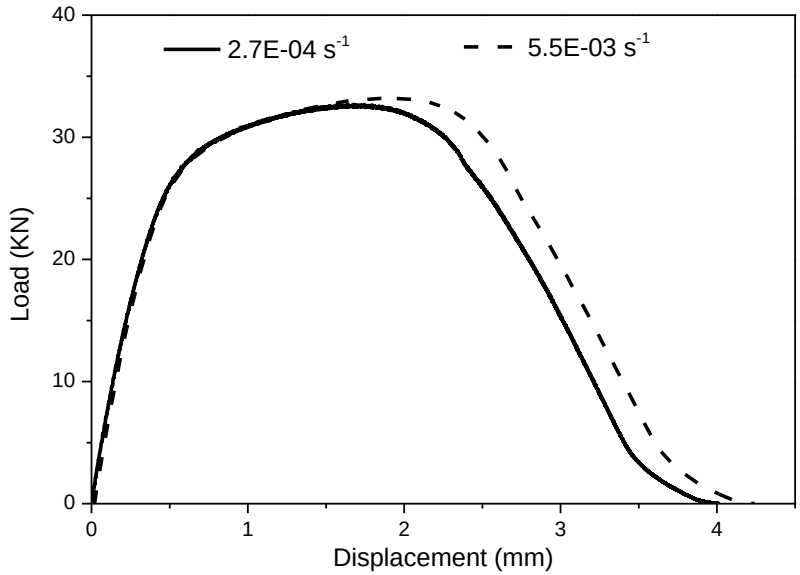

Fig.4.15 Comparison of the load-displacement curves of Test 2 and Test 3 with different two strain rates.

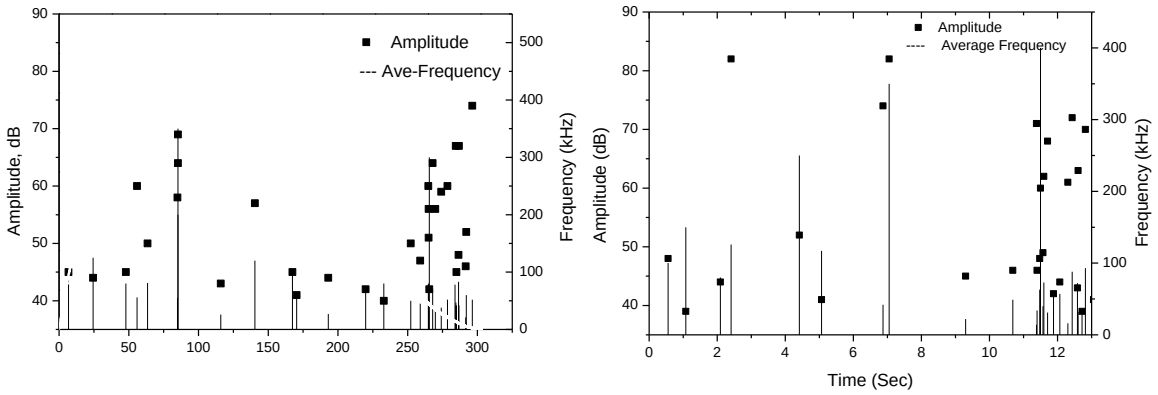

(a) (b)

Fig.4.16 Comparison of AE amplitudes and frequency of Test 2 (a) and Test 3 (b) with different strain rates.

Comparison of the load-displacement curves of Test 2 and Test 3 with different two strain rates is shown in Fig.4.16. It can be seen that in Region I with an increase in strain rate the AE amplitude increases from 35 dB to 50 dB, with some hits reaching 60 dB, and the average frequency increase from 100 kHz for 2.7×10^{-4} s^{-1} strain rate to 150 kHz for 5.5×10^{-3} s^{-1}strain rate. In Region II, with an increase in strain rate several strong bursts are generated in both cases (low and high strain rate). The AE amplitude increases from 45 to70 dB and the average frequency is in the range of 150-400 kHz. In Region III, with an increase in strain rate the AE amplitude increases from 45 dB to 70 dB for 2.7×10^{-4} s^{-1} strain rate and 65 dB to 75 dB for 5.5×10^{-3} s^{-1} strain rate and the average frequency is in the range of 100 to 350 kHz.

4.3.1.2 X80 line pipe steel

Fig.4.17 compares the load-displacement curves of three cases (Test 5, Test 6 and Test 7) with different strain rates: 2.7×10^{-4} s^{-1}, 2.7×10^{-3} s^{-1} and 5.5×10^{-3} s^{-1}. These tests of X80 were carried

out at ambient temperatures. It can be seen that the three curves superpose up to the displacement of 0.65 mm. After this critical displacement, the load of the slower deformation (2.7×10^{-3} s^{-1}) decreases while the load of the faster deformation (5.5×10^{-3} s^{-1}) still increases for a certain displacement and then decreases. Beyond the displacement of 1.05 mm, the load of 5.5×10^{-3} s^{-1} is always higher than that of 2.7×10^{-3} s^{-1}.

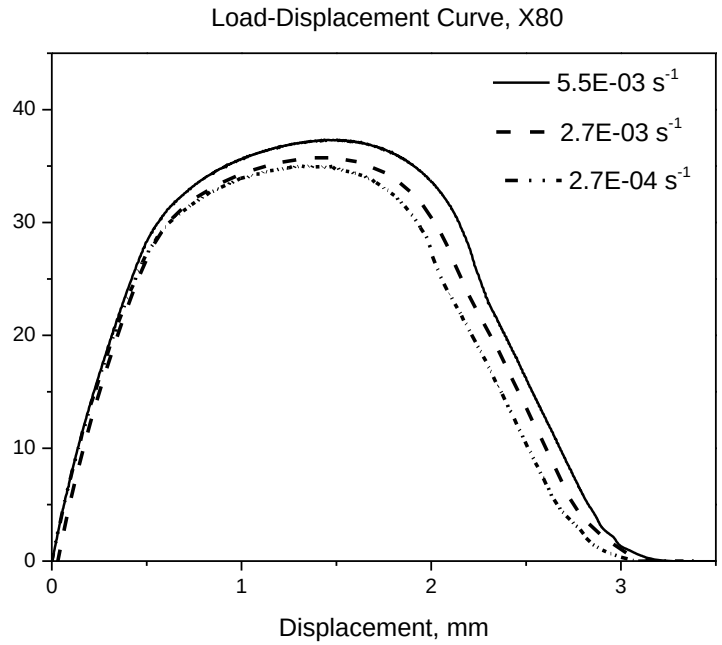

Fig.4.17 Comparison of the load-displacement curves of Test 5, Test 6 and Test 7 with different three strain rates.

The AE waveform and frequency analysis can be a powerful tool to classify events related to fractures [8] and distinguish them from noise [10, 57]. In previous works, the frequency spectrum was shown to vary along the stress-strain/load-displacement curves following a variation in the AE source operating during deformation and failure of steel [104, 127]. In the present study, a dependence of AE activity on loading conditions is investigated. The strain rate could influence AE activity during SENT (Fig.4.12, Fig.4.13 and Fig.4.16).

For X80 line pipe steel (Fig.4.12 and Fig.4.13), with an increase in strain rate, in Region I, the AE amplitude increases from 40 to 45 dB and the average frequency increased from 50-100 kHz to 80-120 kHz. In Region II - several strong bursts are generated from crack initiation. The AE amplitude increases from 50 to 50 dB, and the average frequency increased from 200 kHz to 250 kHz. In Region III, the amplitude increases from 55 dB to 60 dB, the average frequency increases from 100-200 kHz to 150- 250 kHz, and some strong burst signals observed in the end of final fracture.

4.3.2 Effect of temperature

Fig.4.18 compares the load-displacement curves of Test 3 at the ambient temperature and Test 4 at -20 ^{o}C. Both tests were carried out at the strain rate of 5.5×10^{-3} s^{-1}. It can be seen that the two curves superpose up to the displacement of 0.5 mm. After this critical displacement at around yield point, the load of the lower temperature (-20^{o}C) increases compared to the load of the room temperature (+22^{o}C) and then decreases. Beyond the displacement of 0.5 mm, the load of the lower temperature is always higher than that of room temperature. At the final stage of the test, both load curves are superpose.

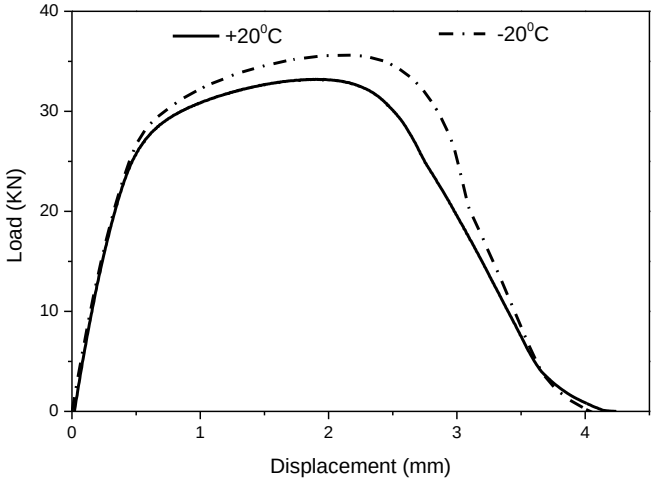

Fig.4.18 Comparison of the load-displacement curves of Test 3 and Test 4 with different testing temperatures.

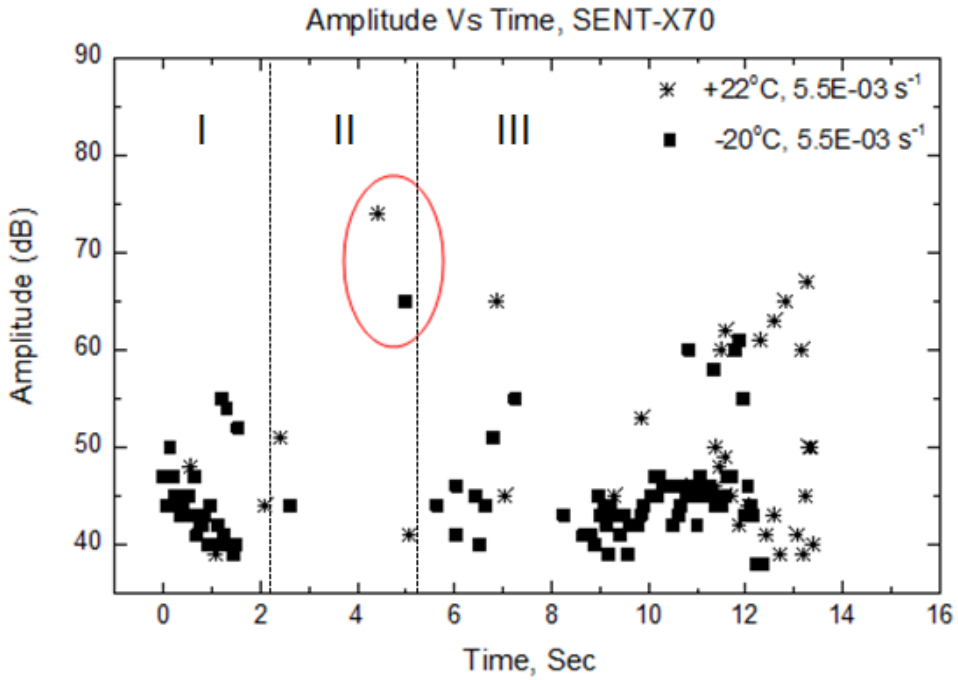

Fig.4.19 Comparison of AE amplitudes of Test 3 and Test 4 with different testing temperatures.

The AE results in Fig.4.19 demonstrate that an increased AE activity in Test 4 was recorded in Region I before the yield point when compared to the test at ambient temperature. In this region, AE signals with amplitude in the range of 50-55dB and frequencies of 200 kHz are detected. A significant increase in the AE hit density is observed in Region III after the maximum load until the final fracture. These hits with an amplitude of ~50 dB and an average frequency of ~100 kHz are associated with crack growth. The relatively strong AE signals with amplitude of 60-65dB and average frequencies of 100-300 kHz are detected at the final stage of the tests. These AE hits are related to unstable crack propagation.

The testing temperature could lead to an increase of AE activity (Fig.4.18). It can be explained by the increase in strength with decreasing temperature. It has been found that the yield and maximum load values of the load-displacement curve are slightly higher at the low temperature than at ambient temperature (Table 4.2). With a decrease in temperature, a significant increase in the AE hit density is observed in Regions I and III. In Region I, the AE amplitude increases from 30-40 dB to 45-50 dB, and the average frequency increases from 50 kHz to 200 kHz. In Region II - the AE amplitude increases from 40 dB for ambient temperature to more than 50 dB for -20^{o}C, and the average frequency increases from 200-300 kHz to 300-400 kHz. In Region III - the AE amplitude increases from 40 to 60 dB and the average frequency increases from 100 kHz to 300 kHz.

4.3.3 Effect of specimen type

Fig.4.20 compares the load-displacement curves of Test 1 and Test 3 at ambient temperature with the strain rate of 5.5×10^{-3} s^{-1}. The specimen for Test 3 has a pre-machined notch. Therefore,

the total displacement to failure is much smaller than Test 1 as shown in Fig.4.20. It has been found that the yield and maximum load values of the load-displacement curve are higher for plain specimen than the SENT.

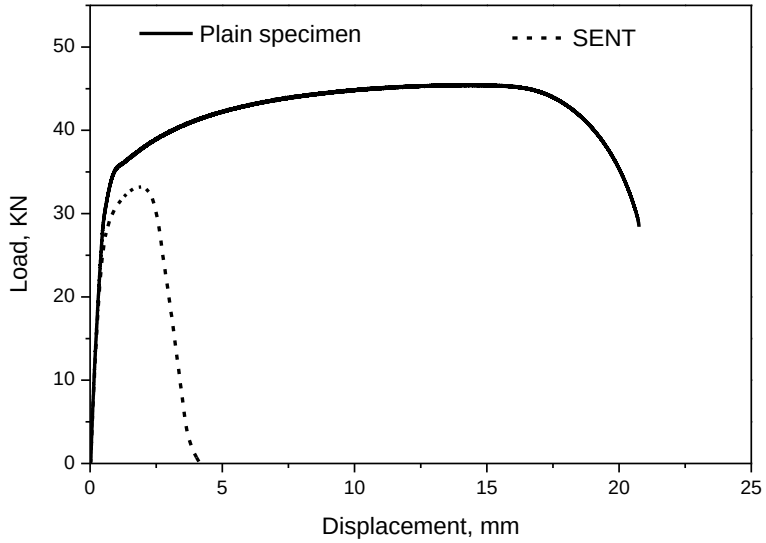

Fig.4.20 Comparison of the load-displacement curves of Test 1 and Test 3.

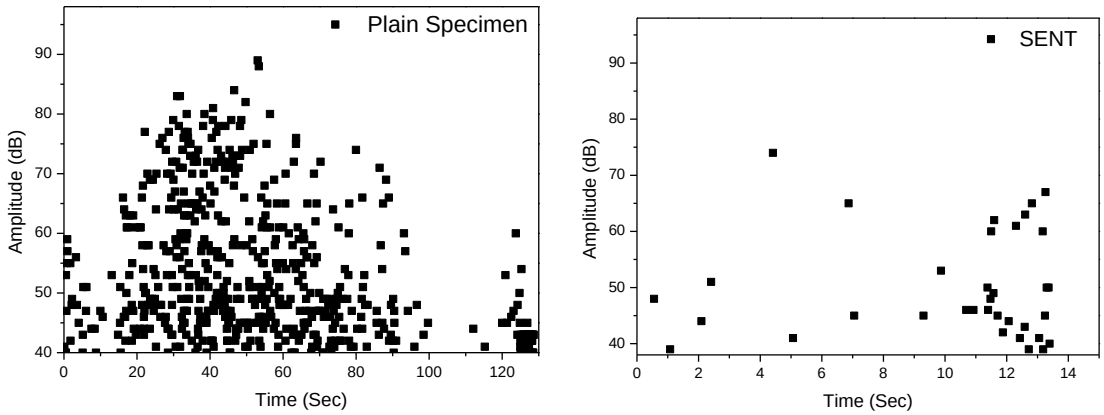

(a) (b)

Fig.4.21 Comparison of AE amplitudes of Test 1 (a) and Test 3 (b).

Comparison of the AE results shown in Fig.4.21 indicates that the AE hit density during work hardening is significantly higher for the plain specimens than that for the notched specimens. As expected, the acoustic emission during testing of plain specimens is higher compared to the notched specimens due to an increased sample deformation zone volume of the plain specimen in contract to the notched specimen.

4.3.4 Effect of steel grade

Comparison of the AE results of X70 and X80 steels at a strain rate of 2.7×10^{-4} s^{-1} and 5.5×10^{-3} s^{-1} are discussed in this section.

4.3.4.1 A lower strain rate

The load-displacement curves of X70 and X80 steels at a strain rate of 2.7×10^{-4} s^{-1} are compared in Fig.4.22. Both SENT tests were carried out at ambient temperatures. It can be seen that the two curves superpose up to the displacement of 1.5 mm. After this displacement, the load of the X70 curve decreases while the load of the X80 still increases for a certain displacement.

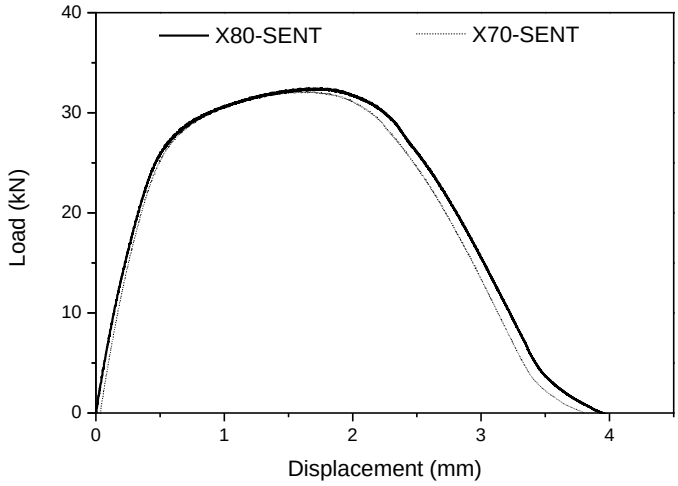

Fig.4.22 Comparison of the load-displacement curves of Test 2 (X70) and Test 5 (X80).

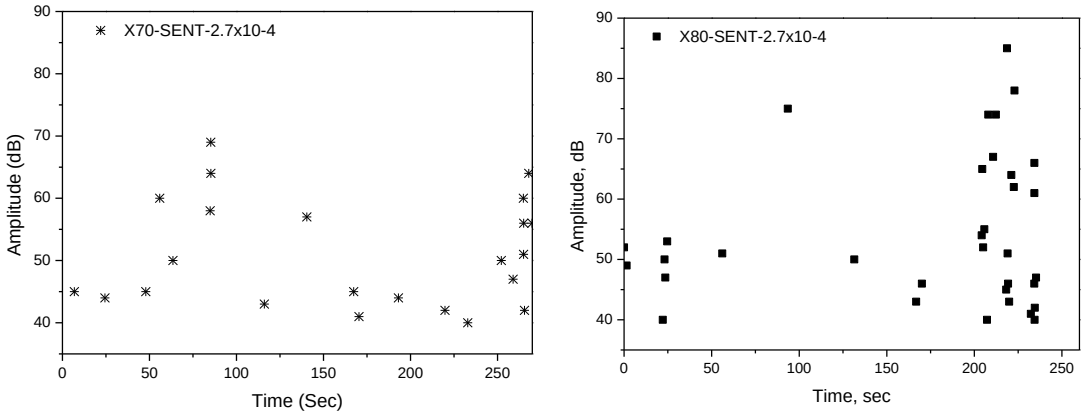

(a) (b)

Fig.4.23 Comparison of AE amplitudes of (a) Test 2 and (b) Test 5.

It can be seen from Fig.4.23 that the AE signal amplitude value of X80 are slightly higher compared to X70 specimen. Other investigations have found similar trend [61, 97, 113] that AE activity increase with an increase of steel strength.

In Region I, the AE signal amplitude increases from 40-50 dB to 50-60 dB, and the average frequency is in the range of 100-150 kHz. In Region II, the amplitude increases from 50-70 dB to

60-75 dB. In this region, the fracture initiation is detected by a sudden change in acoustic emission activity while the onset of plasticity is observed using DIC (Fig.4.11 (b) and (c) in Region II). In Region III, an increased number of AE hits are generated by crack growth and the AE hits density is enhanced at the end of this region. With an increase of fracture toughness for high strength steel, crack growth becomes critical and significant AE signals are generated by micro-void coalescence and alternating shear fracture [10]. The AE signal amplitude varies from 40 dB to 70 dB, with some strong burst signals reaching 75 dB at the final stage of the final separation (Fig.4.11 (a)). The average frequency of 150-300 kHz is detected.

4.3.4.2 A higher strain rate

The load-displacement curve and AE activity of X70 (Test 3) and X80 (Test 7) steels at a strain rate of 5.5×10^{-3} s^{-1} are compared in Fig.4.24 and Fig.4.25, respectively.

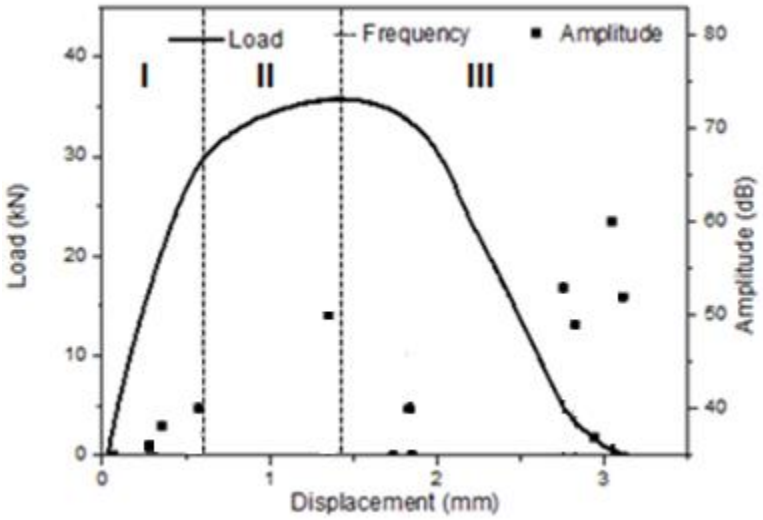

Fig.4.24 Load-displacement curve, AE amplitude for X80

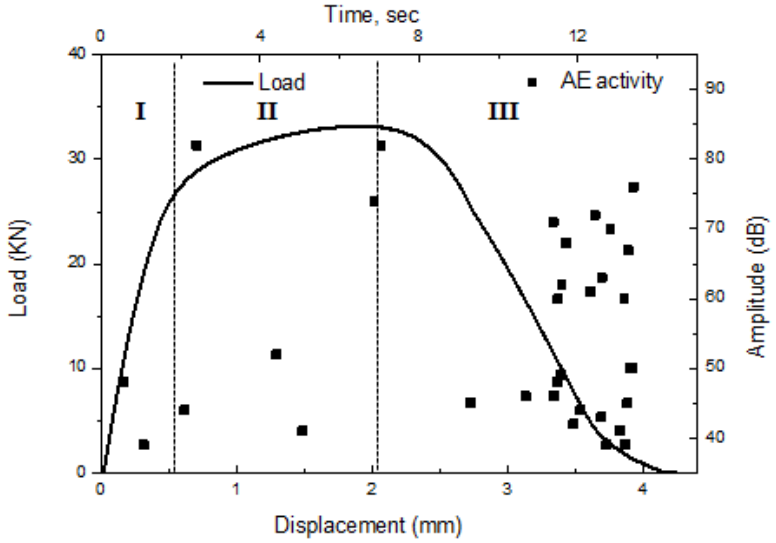

Fig.4.25 Load-displacement curve, AE amplitude for X70

It can be seen from Fig.4.24 and Fig.4.25 that with an increase in steel grade, in Region I, the AE signal amplitude is in the range of 40-45 dB, the average frequency increases from 70-120 kHz to 100-200 kHz. In Region II, the amplitude increases from 40 dB to 55 dB and the average frequency is the range of 100-350. In this region, the fracture initiation is detected by a sudden change in AE hit. In Region III, an increased number of AE hits are generated by crack growth compared to X80 line pipe steel.

4.3.5 Determination of crack initiation point

As described in Chapter 2, the determination of fracture initiation plays a very important role in the research of the pipeline fracture control. In this study, a high speed camera has been used to visualize the moment when the fracture initiates. In order to analyze, the AE feature before fracture initiation, Fig.4.26, Fig.4.27 and Fig.4.28 have been plotted in the following:

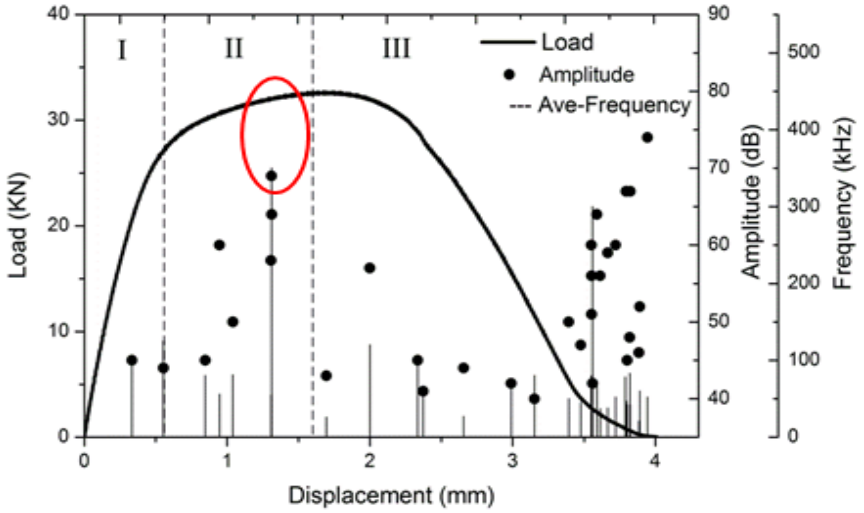

Fig.4.26 Load-displacement curves vs AE activity obtained during testing of SENT specimens at a strain rate of $2.7\times10^{-4}\ s^{-1}$ at ambient temperature.

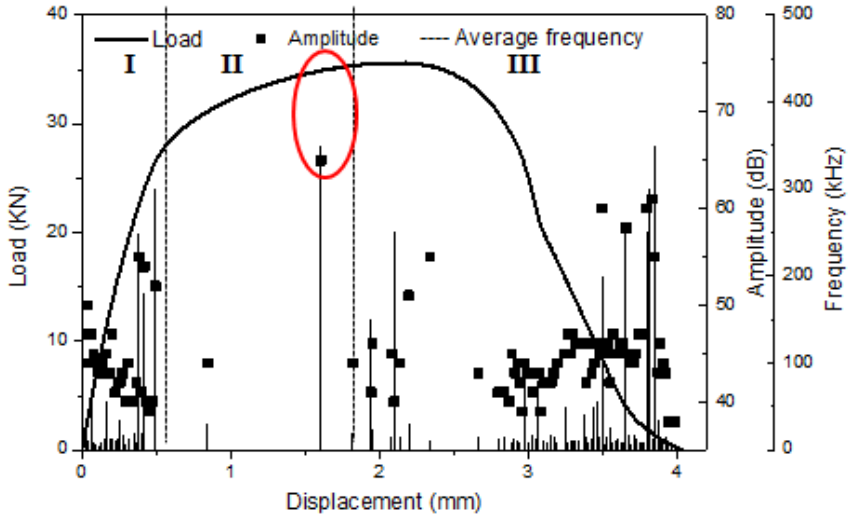

Fig.4.27 Load-time curves vs AE activity obtained during testing of SENT specimens at strain rate of $5.5\times10^{-3}\ s^{-1}$ at -20^{o}C temperature.

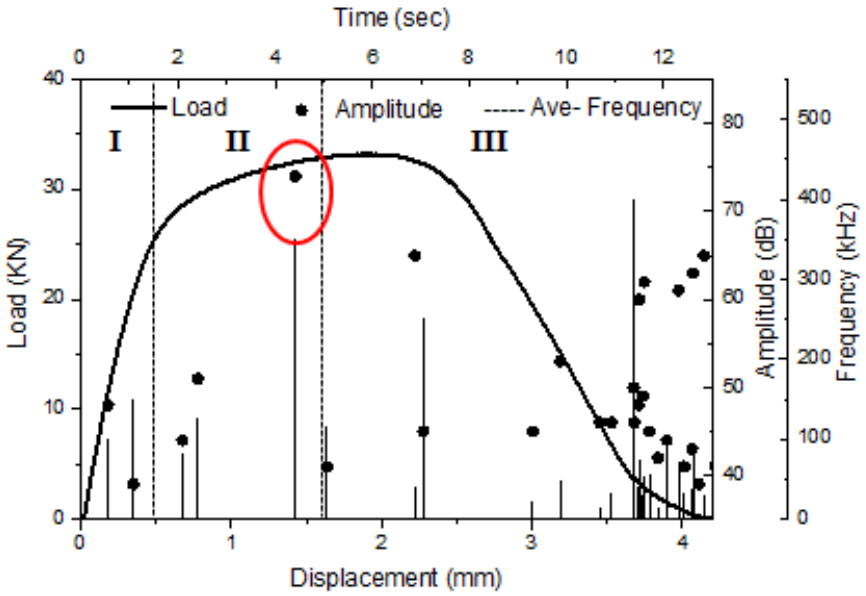

Fig.4.28 Load-time curves vs AE activity obtained during testing of SENT specimens at strain rate of 5.5×10^{-3} s^{-1} at room temperature.

Fig.4.29 shows three pictures collected from the recorded video during SENT at strain rate of 5.5×10^{-3} s^{-1}at room temperature. The corresponding results are given in Fig.4.28. Fig.4.29 (a), (b) and (c) correspond to three loading times, 0.01s, 3.85s and 4.15s, respectively. At the time of 0.01 s the stretching just started. At the time of 3.85s the sample was subjected to plastic deformation. It can be seen that the crack is initiated at the notch tip at t=4.15s as marked by a red circle in Fig.4.29. Fig.4.28 shows that the crack initiation occurred before the peak load was reached and produced the AE signal of 75 dB amplitude and 350 kHz average frequency, which are higher, than those of other AE hits.

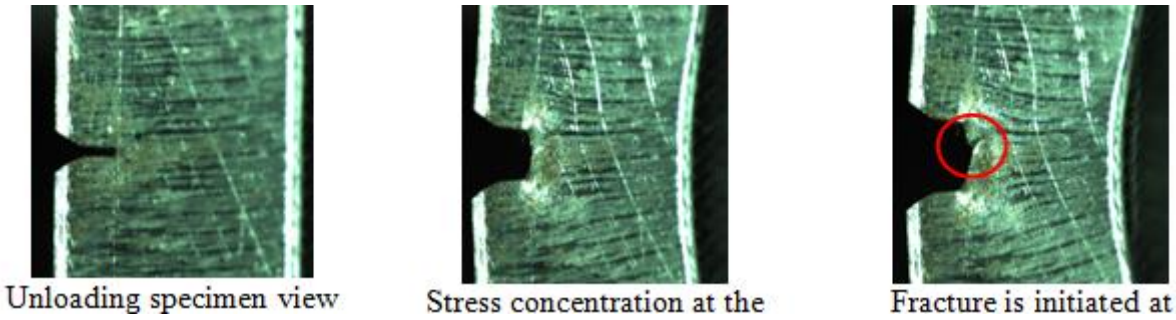

a. b. c.

Fig.4.29 Selected video shots obtained by the high speed camera during testing at a strain rate of 5.5×10^{-3} s^{-1} after (a) 0.01 s, (b) 3.85 s and (c) 4.15 s test time.

Fig.4.28 shows that there is a rapid change in AE activity; in particular an increase in the AE hit density, signal amplitude and average frequency at around t=4.15s. It can be concluded that the rapid change in AE activity in Region II is caused by the fracture initiation. An AE hit with relatively large amplitude can also be observed in the other tests. The video data confirms that the fracture initiation is responsible for this event. This finding is similar to some earlier published data. During compact and bending tests of SA333 steel a sudden increase in AE cumulative count and cumulative energy was resulted from crack initiation [96]. During mechanical testing of pressure vessel steel a high amplitude AE signal was initiated by the crack growth [100]. However, in this study it has been found that the cumulative count is not an effective parameter for detecting the fracture initiation point.

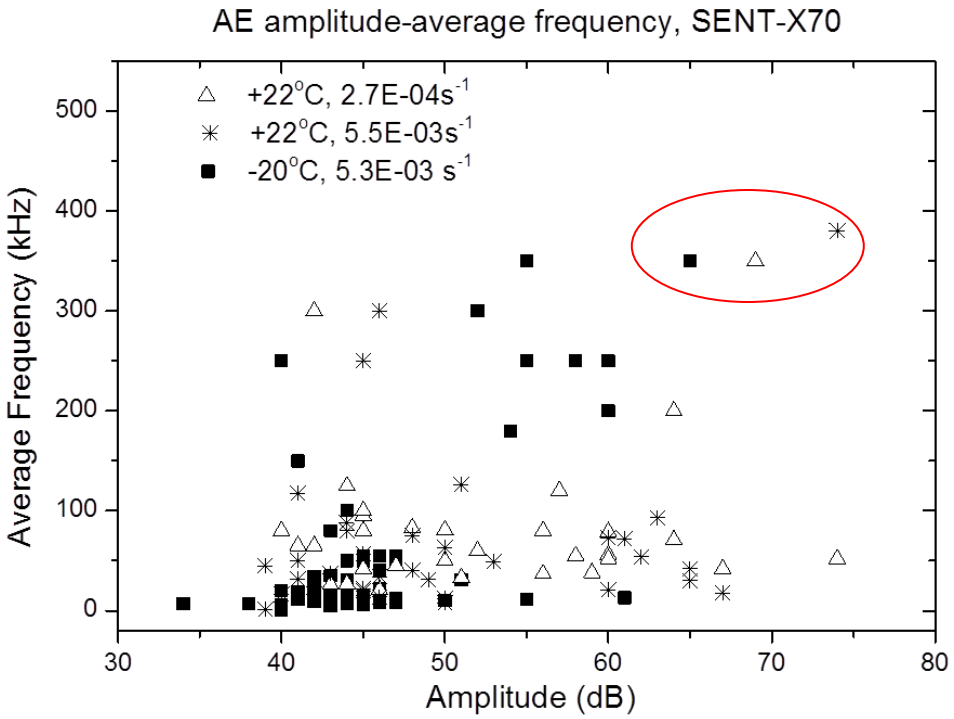

Fig.4.30 The AE hit average frequency-amplitude distributions during testing of single edge notched tension specimens for three loading conditions.

Fig.4.30 shows the AE hit average frequency-amplitude distributions during testing of single edge notched tension specimens for three loading conditions.The power spectra corresponding to Regions II shows a larger number of high frequency peaks for the higher strain rate, compared to that for the lower strain rate In addition, the power spectrum peaks occurred at higher frequencies for the higher strain rate compared to these for the lower strain rate (Fig.4.30). These observations can be attributed to crack initiation and propagation. The crack growth related AE has been shown earlier to feature a strong high frequency content [10]. During the final stage of loading, the frequency in Region III becomes high with an increase in strain rate and a decrease in temperature. Selected AE hit waveforms and power spectra corresponding to the fracture

initiation point in loading region II during testing of single edge notch tension specimen at the three conditions are shown in Fig.4.31.

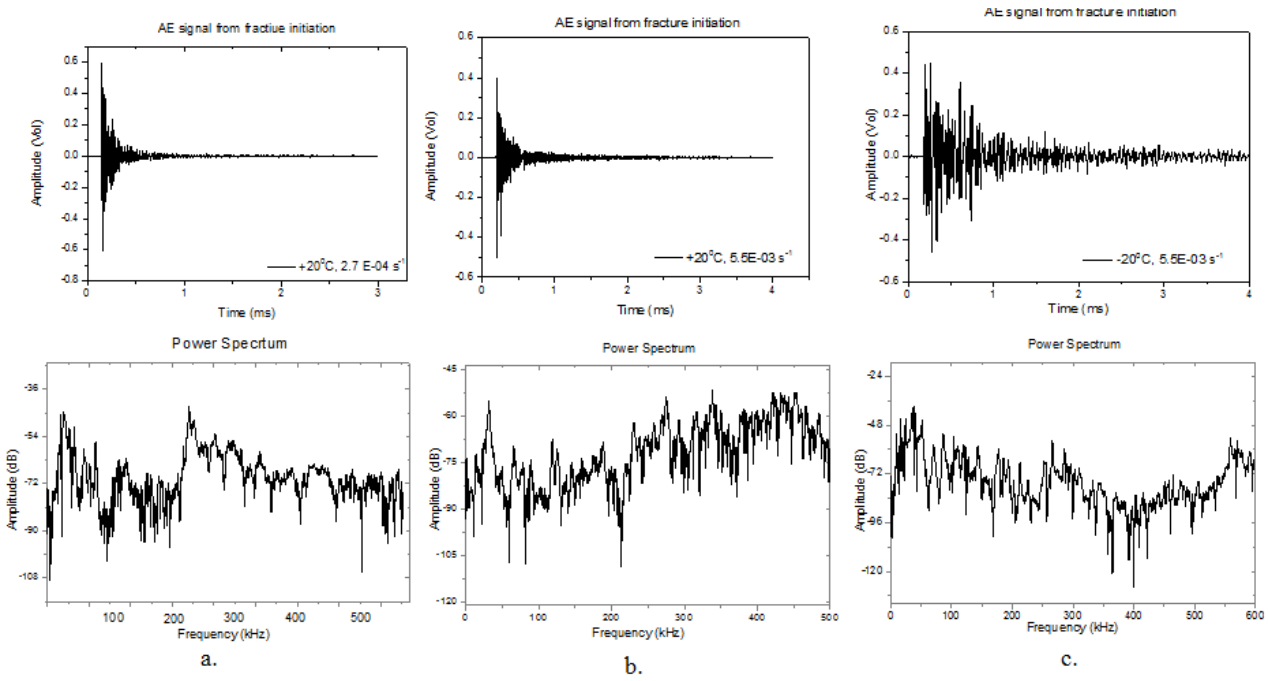

Fig.4.31 Selected AE hit waveforms and power spectra corresponding to the fracture initiation point in loading region II during testing of single edge notch tension specimen at the following conditions: (a) +22^{o}C temperature and 2.7×10 $^{-4}$ s^{-1} strain rate; (b) +22^{o}C temperature and of 5.5×10^{-3}s^{-1} strain rate; (c) -20^{o}C temperature and strain rate of 5.5×10^{-3}s^{-1};

4.3.6 Dependence of AE parameters on crack growth

Void growth and coalescence in ductile materials, such as the line pipe steel, are relatively ‘quiet’ processes. However, a certain detectable amount of AE activity can be generated by the crack propagation in high strength steels [10]. In this study, a high speed video camera was used to measure the crack length during the test (Fig.4.32 (a)) and the crack growth rate was then calculated (Fig.4.32 (b)). Once fracture initiated at 4.15 sec (see red circle), the crack growth was

slow until around 7 sec. Then the crack growth rate increased rapidly up to the final fracture. The correlation between the AE count rate and crack growth rate is shown in Fig.4.32 (b). The AE count rate has a higher peak increase during the period of the fracture initiation (up to 2.5 mm of crack length). Its value is a steadily low during the period of fracture propagation (3-4.5 mm of crack length) and has the second peak during the period of final failure (4.8-5.2 mm of crack length).At the end of the test the AE count rate decreases (5.5-6.0 mm of crack length). It can be seen from Fig.4.32 (b) that the crack growth rate is proportional to the AE count rate.

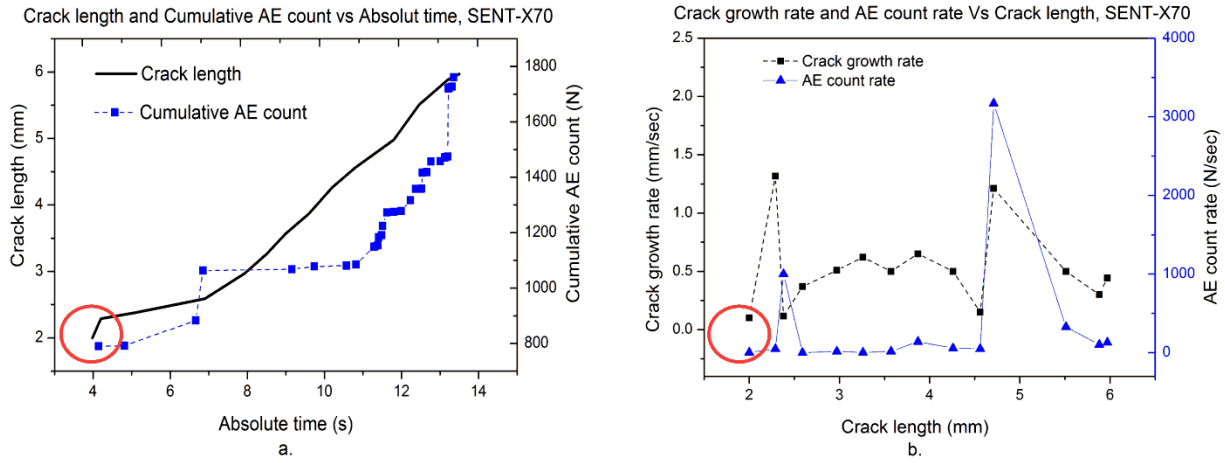

Fig.4.32 Variation in (a) crack length and AE cumulative count with test time and (b) crack growth rate and AE count rate with crack length during SENT at strain rate of 5.5×10^{-3} s^{-1} at ambient temperature.

4.3.7 Dependence of AE parameters on fracture mode

In all the tests conducted in this chapter, the fracture behaves in the ductile mode. From fracture mechanics, it has been known that the ductile crack growth is characterized by micro void nucleation, growth and coalescence. As the specimen is loaded, local strains and stresses at the

crack tip become sufficient to nucleate voids and these voids grow as the crack blunts, and link with the main crack [40].

Scanning electron microscopy (SEM) has been used to observe fracture surfaces of four X70 SENT tested specimens. The testing conditions are given in Table 4.4. Fig.4.33 shows the observed fracture surfaces. The final void size can be measured from these SEM pictures.

Table 4.4 Average void size with a various testing condition.

Testing condition	A	B	C	D
Strain rate	$5.5(10)^{-3}$ s^{-1}	$5.5(10)^{-3}$ s^{-1}	$2.7(10)^{-4}$ s^{-1}	$2.7(10)^{-4}$ s^{-1}
Temperature	$-20^{o}C$	$+22^{o}C$	$-20^{o}C$	$+22^{o}C$
Average Void size	1.7 µm	2.5µm	2.7µm	3.4µm

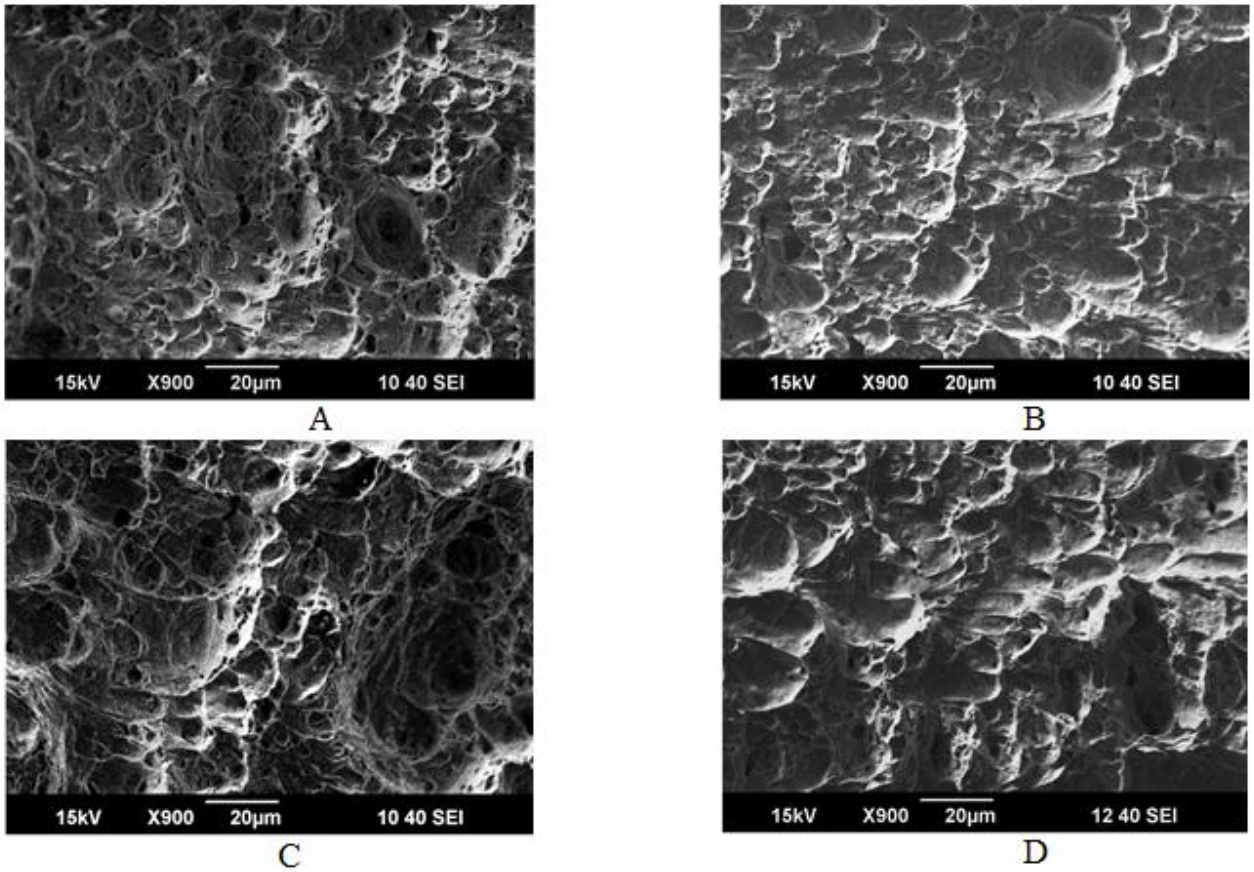

Fig.4.33 Fracture surfaces of SENT specimens for four test conditions A, B, C and D listed inTable 4.4.

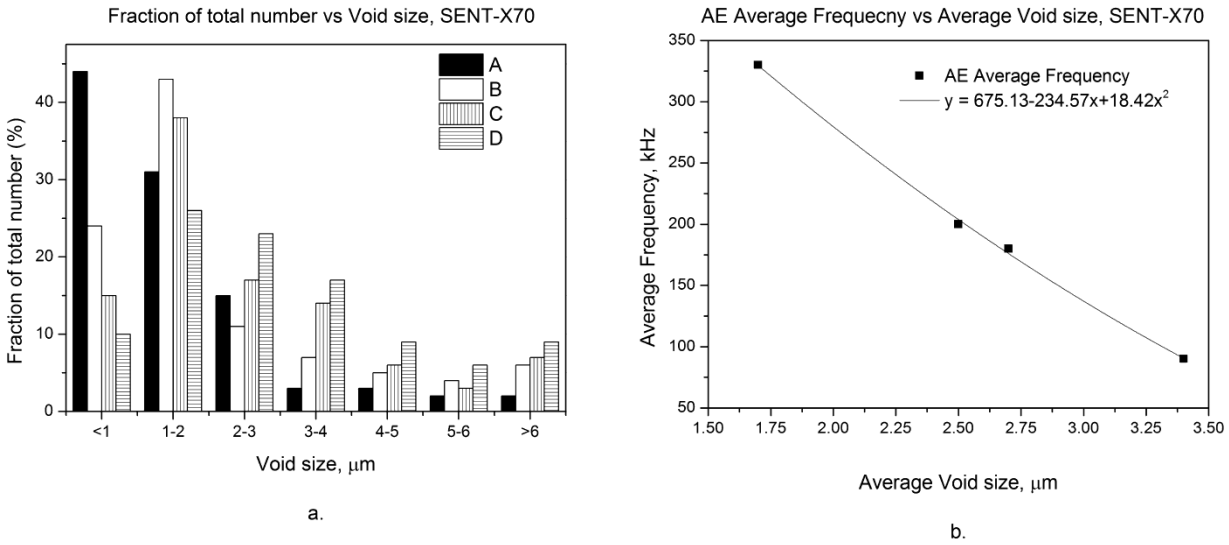

Fig.4.34 (a) The void size distributions for four studied test conditions and (b) the variation in AE average frequency with average void size

Fig.4.34 shows the distribution of void size for four specimens. It can be seen that the void size distribution varies with the test conditions (Fig.4.34 (a)). The number of small voids (< 1 μm) decreases and the number of large voids (> 3 μm) increases with an increase in temperature and a decrease in strain rate. This finding is consistent with the conclusion previously reported [128]. Fig.4.34 (b) shows the AE average frequency as a function of void size. It is clear that the average frequency decreases with the void size. A function, $y=675.13-234.57x+18.42x^2$, can be used to describe their relationship. To the best knowledge of the author, the dependence of the AE average frequency on average void size obtained in this work is reported for the first time.

4.4 Summary

The research of this chapter can be summarized as follows:

1) The AE activity started before the yield point (Region I) due to the stress concentration at the crack tip and increased suddenly before the maximum load was reached (Region II) due to the fracture initiation. Towards the end of test (Region III), the AE hit density increased following the completion of fracture.
2) With an increase in the strain rate from 2.7E-04 s^{-1} to 5.5E-03 s^{-1}, in Region I, the AE amplitude increased from 30 to 40 dB, with some hits reaching 55 dB, and the average frequency increased from 100 kHz-150 kHz. In Region II, several strong bursts were generated in both conditions and with an increase in strain rate the AE amplitude increased from 45 to70 dB, although the average frequency was in the range of 150-400 kHz. In Region III, the AE amplitude increased from 45 dB to 65 dB and the average frequency was in the range of 150-350 kHz.
3) With a decrease in temperature, a significant increase in the AE hit density was observed in Region I and III. In Region I, the AE amplitude was in the range of 40-55 dB at -20 ^{o}C, and the average frequency increased from 50 kHz to 200 kHz. In Region II, the AE amplitude increased from 40 dB for the ambient temperature to more than 50 dB at -20^{o}C, and the average frequency was in the range of 200-350 kHz. In Region III, the AE amplitude was in the range of 40-60 dB and the average frequency increased from 100 kHz to 300 kHz at -20 ^{o}C.

4) AE activity during the tensile test of plain specimen was higher compared to the SENT specimen because of an increased sample volume of the plain specimen and with respect to the notched specimen.
5) The hybrid approach of DIC and AE monitoring method can provide a detailed observation of the plastic deformation around the notch and crack detection on the SENT specimen. The AE activity of the X 80 specimen increased compared to the X70 specimen and an increased number of AE hits were generated.
6) The fracture initiation point can be detected by a sudden change in the acoustic emission activity. In particular, the fracture initiation in the studied steel resulted in a burst AE signal with 65-75 dB amplitude and a 300-350 kHz average frequency just prior to the maximum point of load-displacement curve.
7) Crack growth rate can be predicted using its dependence on the AE count rate. With an increase in crack growth rate the AE count rate increases.
8) The amount of small voids decreases and the amount of large voids increases with an increase in temperature and a decrease in the strain rate, which supports a transition to a more ductile behaviour. The AE average frequency was observed decreasing with an increase in void size.

5 ACOUSTIC EMISSION MONITORING OF CVN TEST

In this chapter, the fracture behaviour of X70 and X80 line pipe steel during Charpy V-Notch test (CVN) was investigated using the acoustic emission (AE) monitoring technique. The work of the chapter has been submitted to Engineering Fracture Mechanics.The effects of testing temperature and specimen thickness on the fracture initiation and propagation are discussed in details.

5.1 Experimental procedure

The CVN procedures and a dimensions of the test pieces were taken from the Australian standard-1544.2 [35]. The configuration of supports (anvil), stricker and specimen have been given in Section 2.2.1.

CVN tests using full size specimen with the thickness of 10 mm (B=10mm, where B is the specimen thickness) were performed at various temperatures: RT (20^{o}C), -20^{o}C, -40 ^{o}C,-60 ^{o}C,-80^{o}C, -100^{o}C and -120^{o}C, using an instrumented Charpy impact machine. In addition, sub-size specimens with B=5 mm and 7.5mm for X70 line pipe steel were used for testing at ambient temperature. Each test has been repeated three times. During the test the absorbed impact energy and the load-deflection curve were measured. The tempertaure of the specimen was controlled by a cooler. The cooler uses methanol to cool the specimen down to -80 ^{o}C and a mixture of liquid nitrogen and methanol to cool the specimen below -80 ^{o}C. Before the test the specimen was kept in the cooler for at least 40 minutes to achieve a uniform temperature.

Fig.5.1 shows a schematic of the AE measurement setup in the CVN test. The AE sensor was non-permanently attached to one of the anvils of the Charpy machine with a sticky band, and ultrasound treatment gel was applied as a coupling material to increase the signal quality. The choice for the sensor location was determined by minimizing the saturation condition.

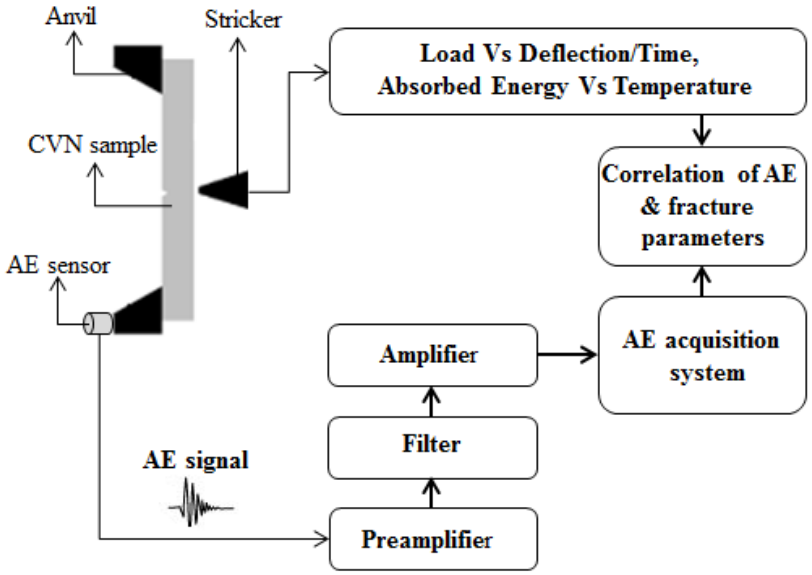

Fig.5.1 A schematic experimental set up of instrumented Charpy testing.

5.2 Effect of temperature

5.2.1 X70 line pipe steel

Full-size CVN tests have been conducted at 7 temperatures. Fig.5.2 only shows the load-deflection curves for three typical temperatures: 20^{o}C, -60^{o}C and -120^{o}C. It can be seen in Fig.5.2 that at 20^{o}C the load increases with the deflection. At a deflection of 5 mm, the load reaches its maximum and then gradually decreases with the deflection. At the final stage of the test at a deflection of around 25 mm, the load still remains a quite high value, followed by a

quick drop of the load. This behavior is due to the fact that the material is too tough to be fully broken at this temperature. For the test at -60^{0}C, the maximum load is higher than the test at 20^{o}C. However, beyond the peak point the drop of the load at -60^{0}C is much quicker than that for 20^{o}C. At the final stage of the -60^{o}C test the load gradually approaches zero. The load of the -120^{o}C test reaches its maximum value at a very low defection and then rapidly drop to near zero. This clearly indicates that the specimen broke in a brittle mode at this temperature.

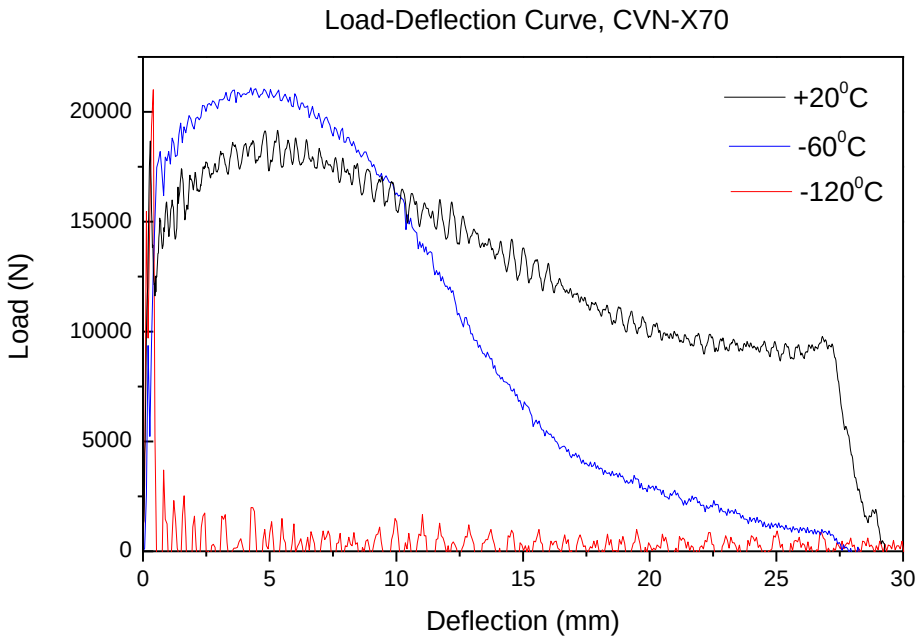

Fig.5.2 Load-Deflection curves of instrumented Charpy impact test at +20^{o}C, -60^{o}C and -120^{o}C.

Fig.5.3, Fig.5.4 and Fig.5.5 show the fracture surfaces of CVN specimens which were fractured at 20°C, –60°C and –120°C, respectively. For all three specimens, overall fracture surfaces were imaged at low magnification and regions close to the notch and close to the fracture were observed at high magnification. It can be seen that the overall appearances of the fracture

surfaces are different for the three specimens and the fracture mechanisms at regions close to the notch and close to the fracture in a single specimen are different.

It can be seen in Fig.5.3 that the fracture surface of the CVN specimen fractured at 20°C is fully ductile with 100% fibrosity. There can be seen apparent necking and shear lip areas. The region close to the notch shows a typical ductile fracture with elongated shearing dimples and microvoids. The region close to the fracture also shows a ductile fracture but the dimples are much larger in size and much shallower compared to the region close to the notch. The mechanism of ductile crack growth can be characterized by micro-void nucleation, growth and coalescence. As the specimen is loaded, local strains and stresses at the crack tip suffice for void nucleation. These voids grow as the crack tip blunts, and link with the main crack [40].

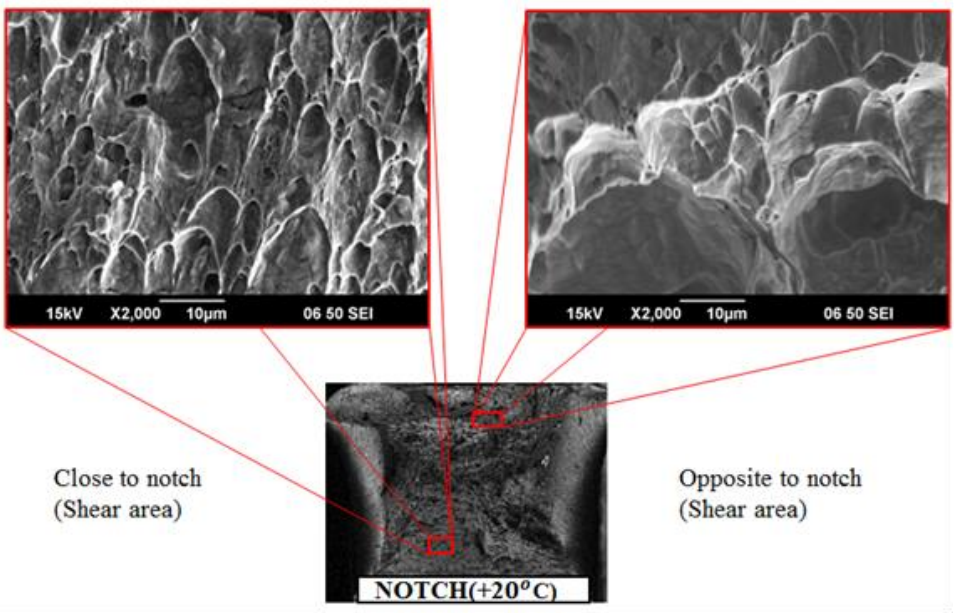

Fig.5.3 Fracture surface for 10 mm thick CVN specimen at +20°C.

The specimen fractured at –60°C shows a half ductile and half brittle type of fracture surface, as can be seen in Fig.5.4. The half close to the notch shows a similar appearance to that of Fig.5.3,

with apparent necking and shear lips. Observation at high magnification also shows ductile fracture with elongated dimples and microvoids. The half close to the fracture shows a typical brittle fracture appearance without necking and cleavage facets are observed at high magnification.

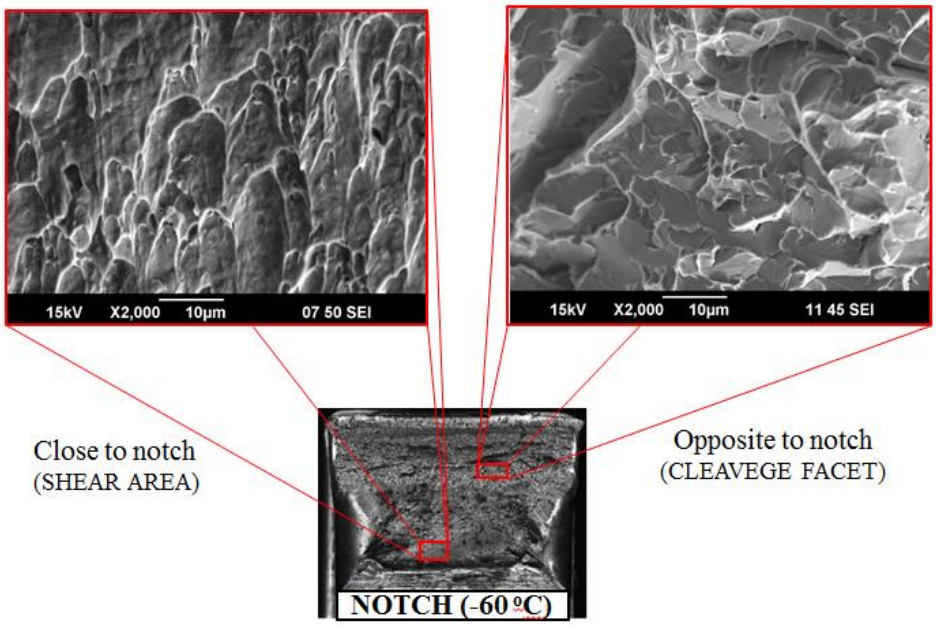

Fig.5.4 Fracture surface for 10 mm thick CVN specimen at -60^{o}C.

Fig.5.5 shows the fracture surface of the CVN specimen fractured at –120°C. A typical brittle fracture is observed for this specimen. The fracture surface is generally flat and without any necking. Higher magnification observation of the regions close to the notch and close to the fracture both show typical brittle fracture with cleavage facets and river patterns.

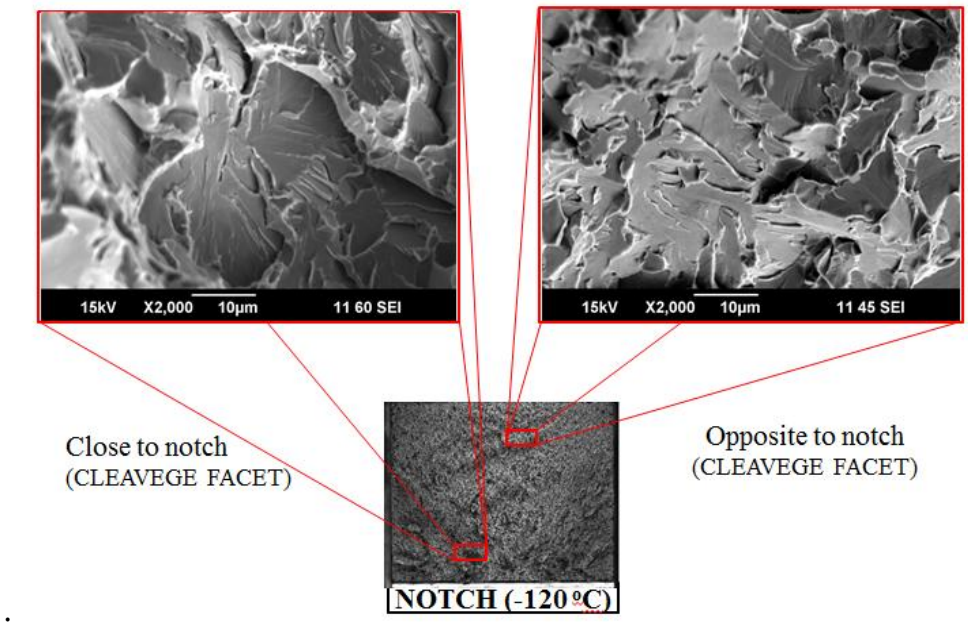

Fig.5.5 Fracture surface for 10 mm thick CVN specimen at -120^{o}C.

Table 5.1 lists the average CVN energy, shear area percentage, load at yield and maximum load for all the tests. The average CVN energy and shear area percentage decrease and the load at yield and the maximum load increase as the temperature decreases.

Table 5.1 Summary of experimental results for CVN standard specimens with a various temperature for X70.

Temperature, T [^{o}C]	Average CVN energy, C_v [J]	Shear Area, %	Load at yield P_{yield}[N]	Load at maximum P_{max}, [N]
+20	330.3	100	14895	17990
-20	310.5	100	16525	18952
-40	285.4	88	16874	20902
-60	228.5	74	17012	21150
-80	40.8	35	17989	21584
-100	12.1	24	-	21864
-120	8.5	7	-	21918

Fig.5.6 and Fig.5.7 demonstrate the CVN energy and the percentage of shear area as functions of the testing temperature, respectively. It is clear that at the ambient and -20^{o}C temperatures, the specimens have very high toughness and their shear area percentages are 100%, indicating that these specimens failed in a ductile mode. The material experiences a ductile-to-brittle transition as the temperature is reduced. The ductile to brittle transition temperatures (DBTT) is found here to be in the range of -40 ^{o}C – 80 ^{o}C. At lower temperatures (-100^{o}C and -120^{o}C), the shear area percentages are very low, meaning that the brittle mode dominates. Therefore the energy curve can be divided into separate regions: (1) the ductile fracture region which occurs prior to a temperature of -40 ^{o}C; (2) the transition region between -40 ^{o}C and -80 ^{o}C and (3) the brittle fracture region which occurs below -80 ^{o}C.

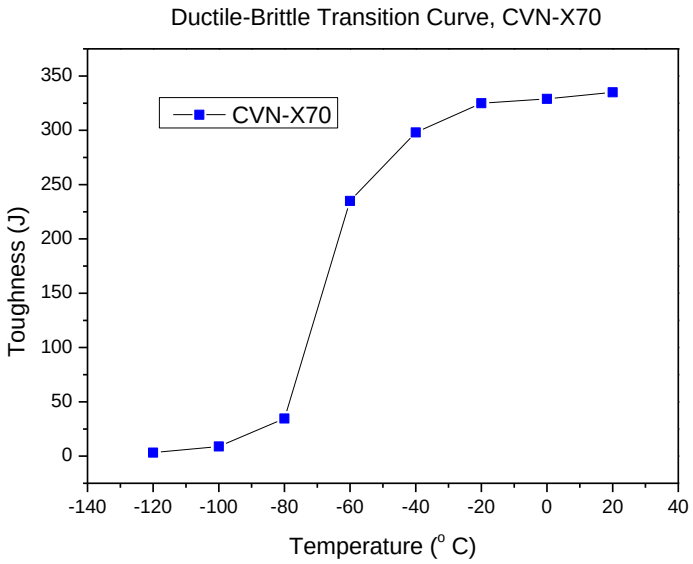

Fig.5.6 Charpy Absorbed Energy vs. Temperature curve during CVN testing.

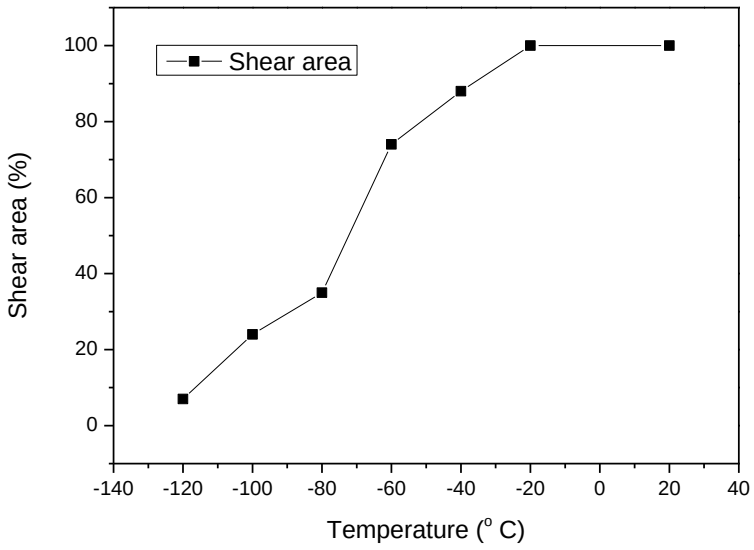

Fig.5.7 Shear area percentage against temperature.

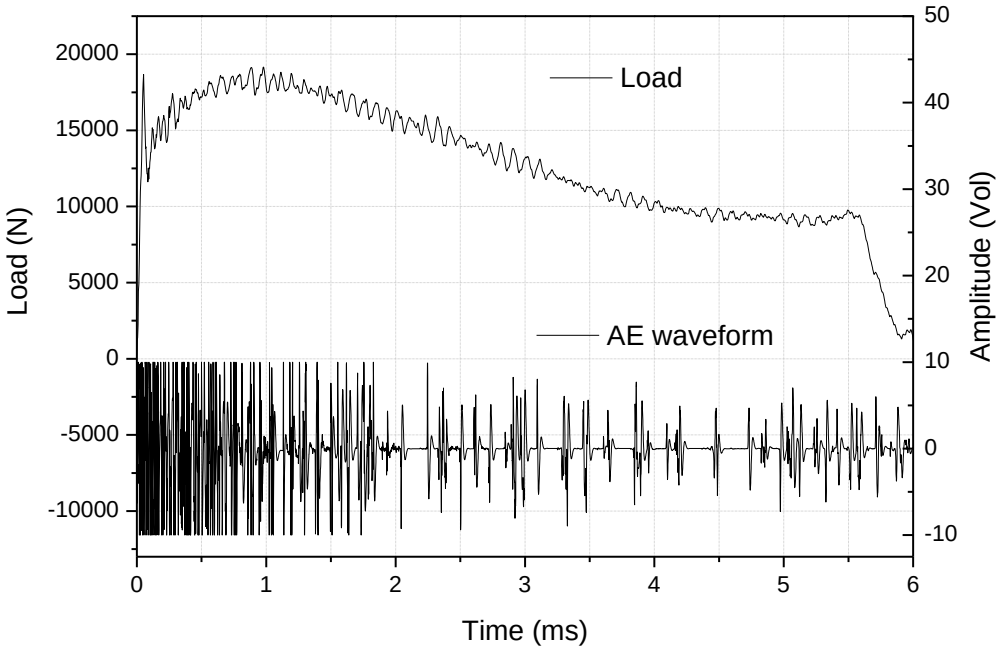

Fig.5.8 Load and Acoustic emission waves versus time for CVN Impact test at ambient temperature (B=10 mm).

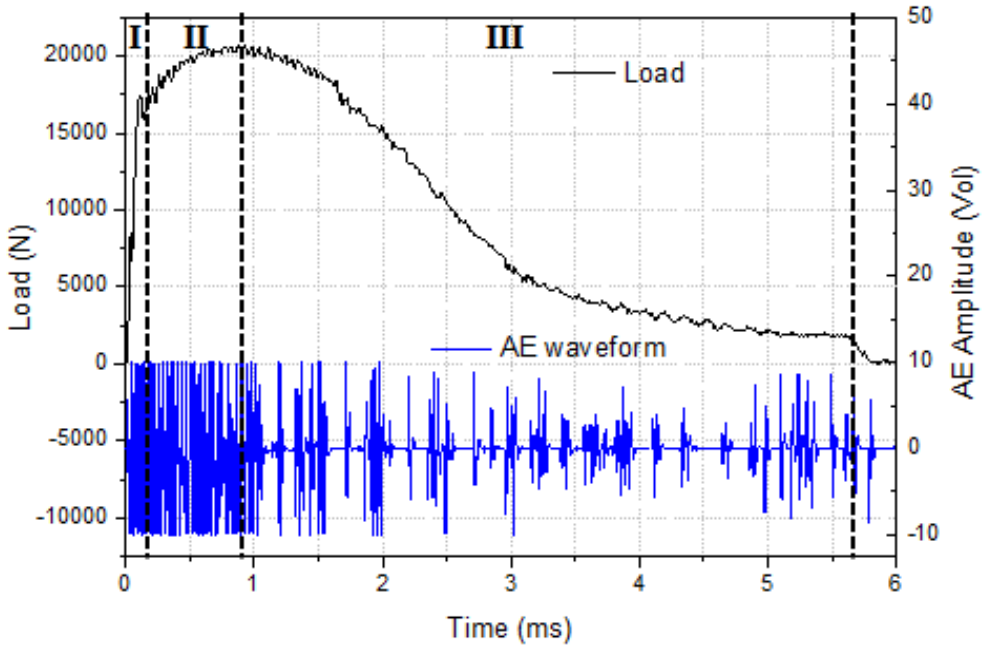

Fig.5.9 Load and Acoustic emission waves versus time for CVN Impact test at -40^{o}C temperature (B= 10 mm).

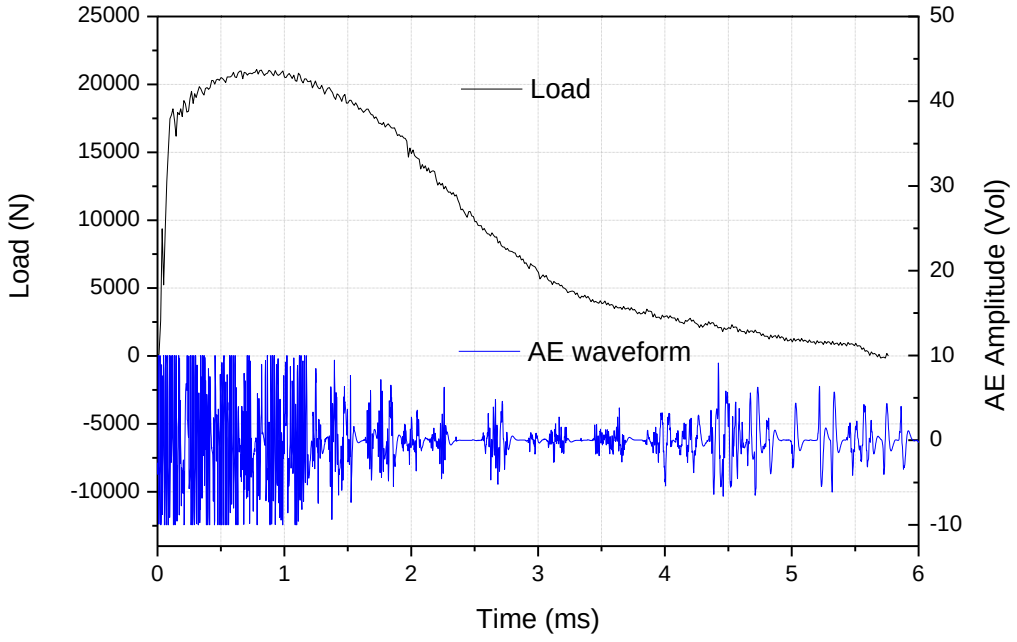

Fig.5.10 Load and Acoustic emission waves versus time for CVN Impact test at -60^{o}C temperature (B=10 mm).

AE signals along with the load-time curve for three tests with the temperatures of 20 ^{o}C,-40 ^{o}C and -60 ^{o}C are shown in Fig.5.8, Fig.5.9 and Fig.5.10, respectively. For the AE signal analysis, the load-deflection curve is divided into three regions: I - before the yield point, II - between the yield point and the peak point, and III - after the peak point till the final fracture. The general trends are observed from Fig.5.8, Fig.5.9 and Fig.5.10 as follows:

1) Region I. A high amplitude AE signal is generated from the hammer impact and sample yielding due to a sudden increase in load under elastic condition;
2) Region II. A characteristic high-frequency burst in the AE signal is observed. This corresponds to ductile fracture initiation. The phenomenon is observed for a short time between the yield point and the point of maximum load.
3) Region III. AE signals generated from fracture propagation are observed. They are of a burst type at high frequency, and a continuous type at frequency lower than in Region II; before the end of the loading curve, a distinct drop is observed that generated a burst in the high-frequency signal due to the occurrence of the brittle fracture.

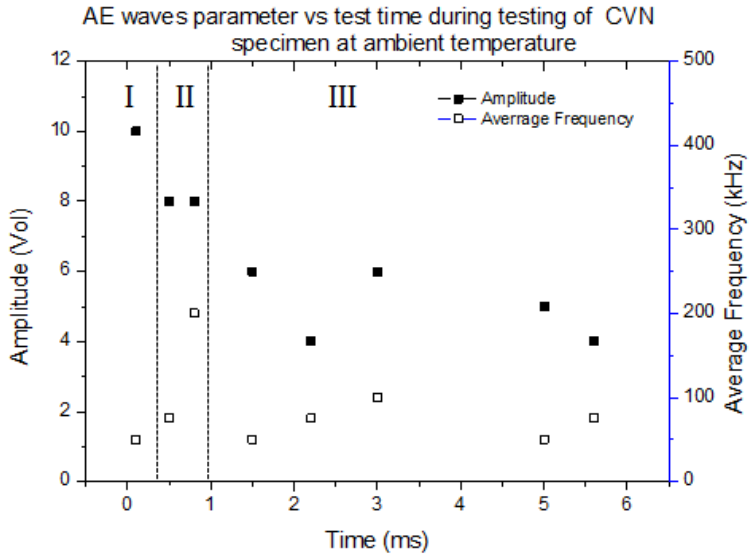

Fig.5.11 The AE average frequency and amplitude as a function of test time at room temperature.

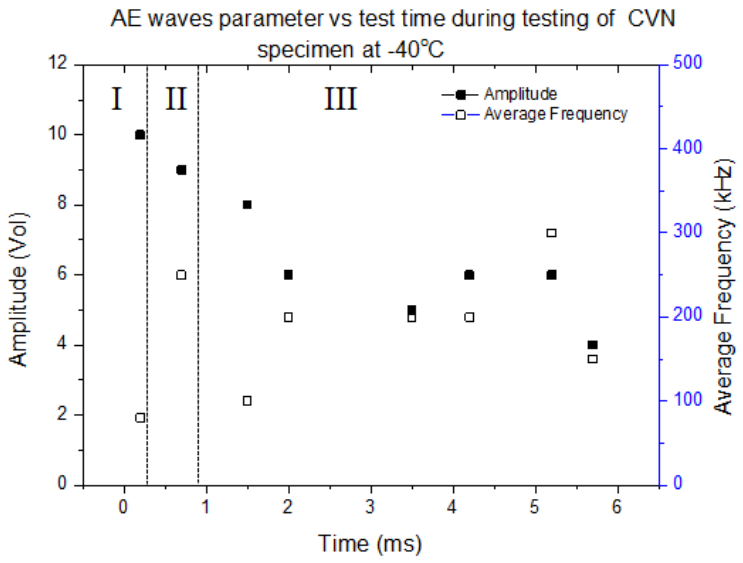

Fig.5.12 The AE average frequency and amplitude as a function of test time at -40°C.

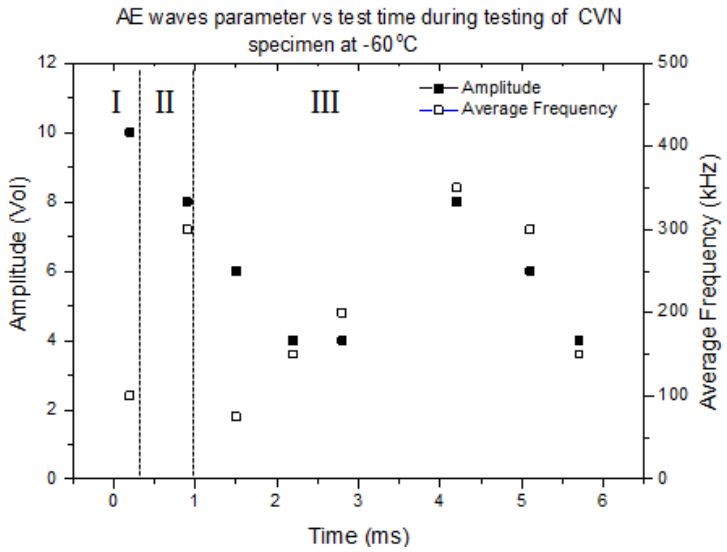

Fig.5.13 The AE average frequency and amplitude as a function of test time at -60°C.

The amplitude and average frequency are calculated from the AE signals and shown in Fig.5.11, Fig.5.12 and Fig.5.13, respectively. At the room temperature, in Region I, the AE signal with a strong amplitude value (8 vol) is observed and its average frequency is less than 100 kHz due to

the hammer impact and elastic deformation. In Region II, a significant burst AE signal with the average frequency in the range of 100-250 kHz is generated before the maximum load is attained. In Region III, the fracture propagates with a reduced load. This process generated a continuous AE signal with a low amplitude of 4 vol and an average frequency in the range of 50 kHz-150 kHz.

In contrast, at -60 ^{o}C, in Region I, the AE signal with the average frequency of 100 kHz is generated due to hammer impact and elastic deformation. In Region II, a significant burst AE signal with an average frequency in the range of 200-250 kHz is observed before the maximum load point. In Region III, the load is dropped rapidly. This process is associated with a few burst AE signals with an amplitude of 4-6 vol and an average frequency in the range of 150-250 kHz. A sudden load drop is observed due to brittle fracture that generates a burst AE signal with high amplitude of 8 vol and high frequency in range of 250-350 kHz.

Table 5.2 AE waveform parameters during CVN testing for X70.

Testing temperature	Region	Amplitude [Vol]	FFT power spectrum frequency peak [kHz]	Suggested cause of AE
RT	I	< 8	50-75	The hammer impact and general yielding (A point)
	II	<4-6	100-200	Plastic deformation and ductile fracture (A-B point)
	III	>4	50-150	Ductile fracture propagation (B-C point)
-40 ^{o}C	I	<8	50-100	The hammer impact and general yielding (A point)
	II	>8	200-250	Ductile fracture initiation (A-B)
	III	4-6	250-300	Crack propagation (B-C)
-60 ^{o}C	I	< 8	100-150	The hammer impact and general yielding (A)
	II	4-6	200-250	Ductile fracture and crack propagation (A-B)
	III	6-8	250-350	Brittle fracture (B-C)

Table 5.2 lists the amplitude and average frequency ranges for each of three regions of the tests conducted at the room temperature, -40°C and -60°C. In Region I, the strong AE signal is generated due to the hammer impact and general yielding. With a decrease in temperature from the room temperature to 60 °C, the AE average frequency increases from 50 kHz to 100 kHz. In Region II, strong AE bursts are generated from crack initiation. The AE average frequency increases from 100-200 kHz to 200-250 kHz. In Region III, the continuous AE signal is identified during crack propagation. The burst signal dominates due to a brittle fracture. Amplitude increases from 4-6 Vol to 6-8 Vol and the average frequency increases from 50-100 kHz to 250- 350 kHz.

5.2.2 X80 line pipe steel

Full-size CVN tests have been conducted at 3 temperatures such as 20°C, -60°C and -80°C. Fig.5.14 shows the load-deflection curves for three typical temperatures.

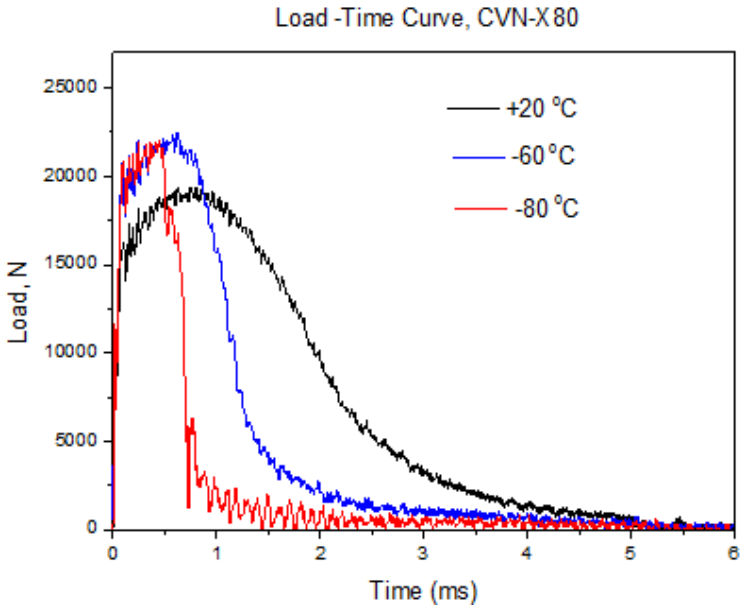

Fig.5.14 Load-Deflection curves of instrumented Charpy impact test at +20°C, -60°C and -80°C

AE signals along with the load-time curve for three tests with the temperatures of 20 ^{o}C,-60 ^{o}C and -80 ^{o}C are shown in Fig.5.15, Fig.5.16 and Fig.5.17, respectively.

For the AE signal analysis, the load-deflection curve is divided into three regions: I - before the yield point, II - between the yield point and the peak point, and III - after the peak point till the final fracture.

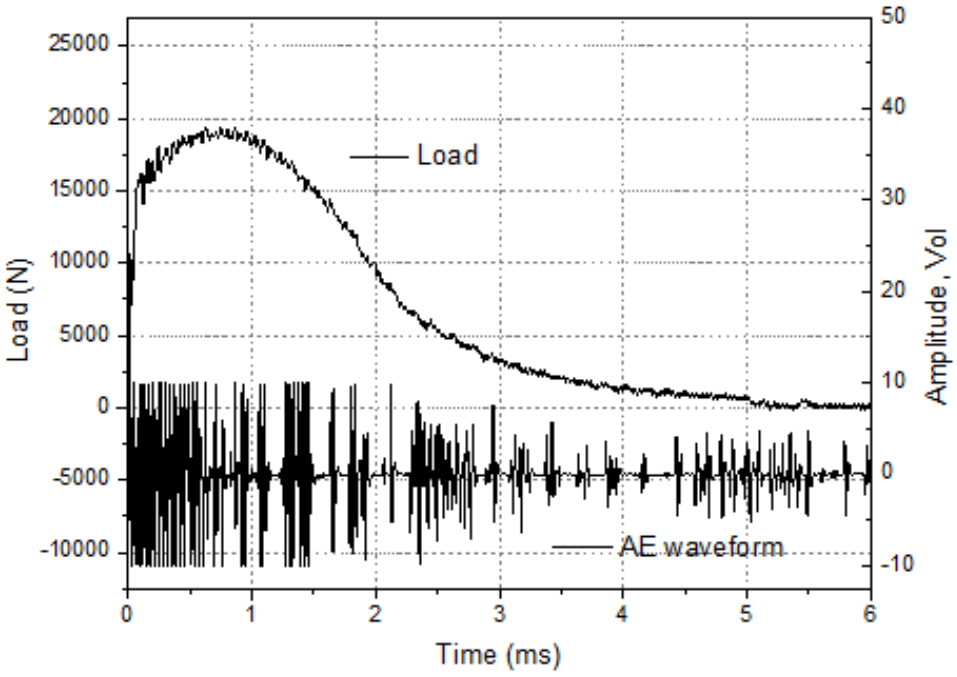

Fig.5.15 Load and Acoustic emission waves versus time for CVN Impact test at ambient temperature for X80 (B=10 mm)

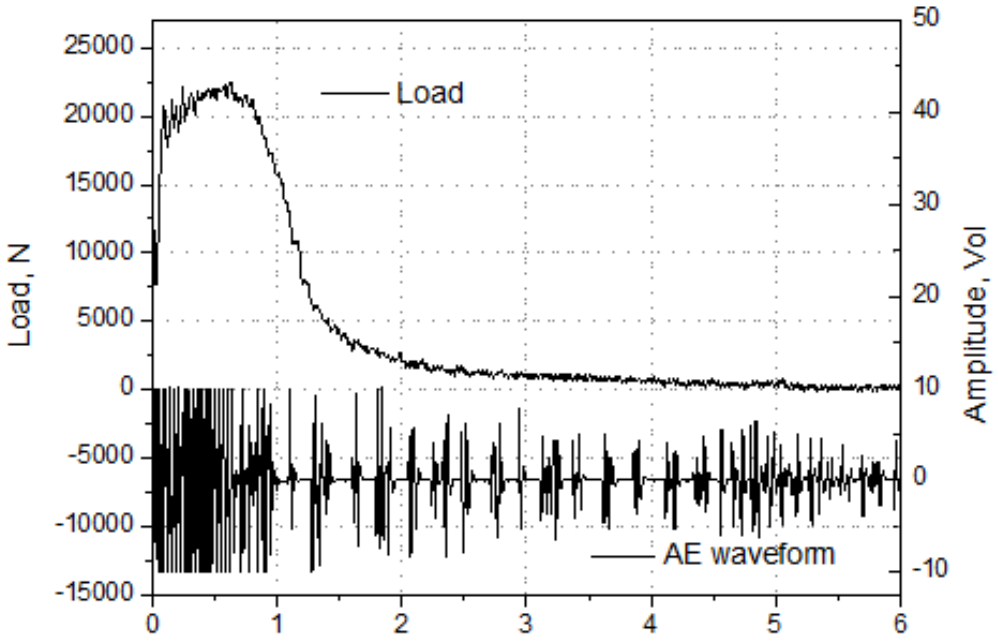

Fig.5.16 Load and Acoustic emission waves versus time for CVN Impact test at – 60 ^{o}C for X80 (B=10 mm).

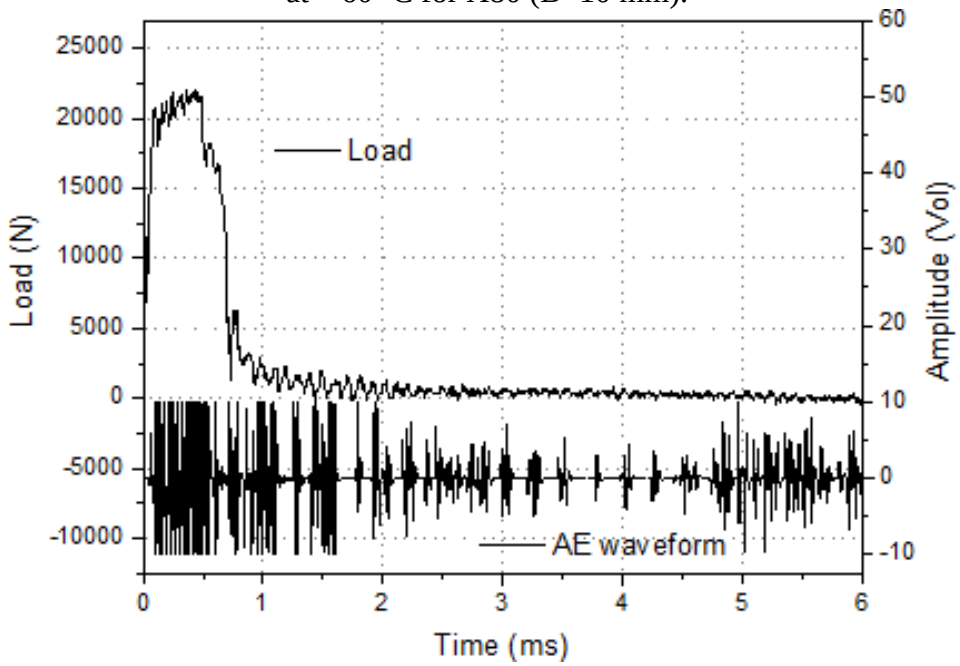

Fig.5.17 Load and Acoustic emission waves versus time for CVN Impact test at – 80 ^{o}C for X80 (B=10 mm).

The amplitude and average frequency are calculated from the AE signals and shown in Fig.5.15, Fig.5.16 and Fig.5.17, respectively. It can be seen from Table 5.3, at the room temperature, in

Region I, the AE signal with a strong amplitude value (10 vol) is observed and its average frequency is less than 50 kHz due to the hammer impact and elastic deformation. In Region II, a significant burst AE signal with the average frequency in the range of 100-200 kHz is generated before the maximum load is attained. In Region III, the fracture slightly propagates with a decrease in load. This process generated an AE signal with low amplitude of 4 vol and an average frequency in the range of 100 kHz-150 kHz.

In contrast, at -60 ^{o}C, in Region I, the AE signal with the average frequency of 100 kHz. In Region II, a significant burst AE signal with an average frequency in the range of 150-250 kHz is observed before the maximum load point. In Region III, the load is dropped rapidly. This process is associated with a few burst AE signals with an amplitude of 4 vol and an average frequency in the range of 100-200 kHz due to brittle fracture.

Table 5.3 AE waveform parameters during CVN testing for X80.

Testing temperature	Region	Amplitude [Vol]	FFT power spectrum frequency peak [kHz]	Suggested cause of AE
RT	I	< 10	<50	The hammer impact and general yielding (A point)
	II	<6	100-200	Plastic deformation and ductile fracture (A-B point)
	III	>4	100-150	Ductile fracture propagation (B-C point)
-60 ^{o}C	I	<8	<100	The hammer impact and general yielding (A point)
	II	>8	150-250	Ductile fracture initiation (A-B)
	III	4	100-200	Crack propagation (B-C)
-80 ^{o}C	I	10	<100	The hammer impact and general yielding (A)
	II	<8	200-250	Ductile fracture and crack propagation (A-B)
	III	<6	200-300	Brittle fracture (B-C)

5.3 Effect of specimen thickness

Fig.5.18 shows the load- deflection curves obtained during the CVN tests of X70 line pipe steel with different thicknesses (B=10mm, 7.5mm and 5mm) at the ambient temperature. Three curves have similar shape and the load increases with the specimen thickness. All the specimens exhibit ductile fracture behavior.

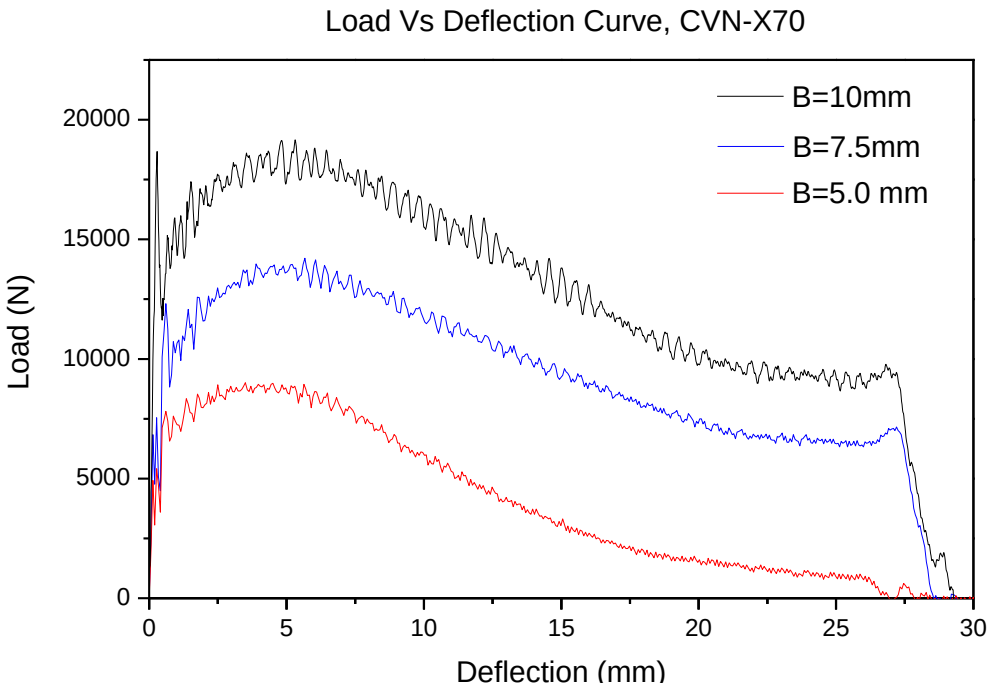

.

Fig.5.18 Load vs deflection curves obtained during instrumented CVN impact testing at ambient temperature of specimens with various thicknesses.

Table 5.4 Experimental results for testing at ambient temperature.

Specimen thickness, B [mm]	Average CVN energy, C_v [J]	Load at general yield $P_{yield\ [N]}$	Load at maximum P_{max}, [N]
10	330.3	14895	17990
7.5	197.3	11150	12800
5.0	108.0	4810	6105

Table 5.4 lists the CVN energy, the load at yield and the maximum load for three specimens with different thicknesses. As the specimen thickness decreases from 10 mm to 5.0 mm, the CVN energy decreases from 303.3 J to 108.0 J. Fig.5.19 (a) plots the CVN energy (Cv) as a function of the specimen thickness, while Fig.5.19(b) plots ln(Cv) against ln(B). A linear regression of the ln(Cv)-ln(B) relationship gives a slope of 1.6. This means that Cv and B have a power relationship, namely $Cv \propto B^{1.6}$.

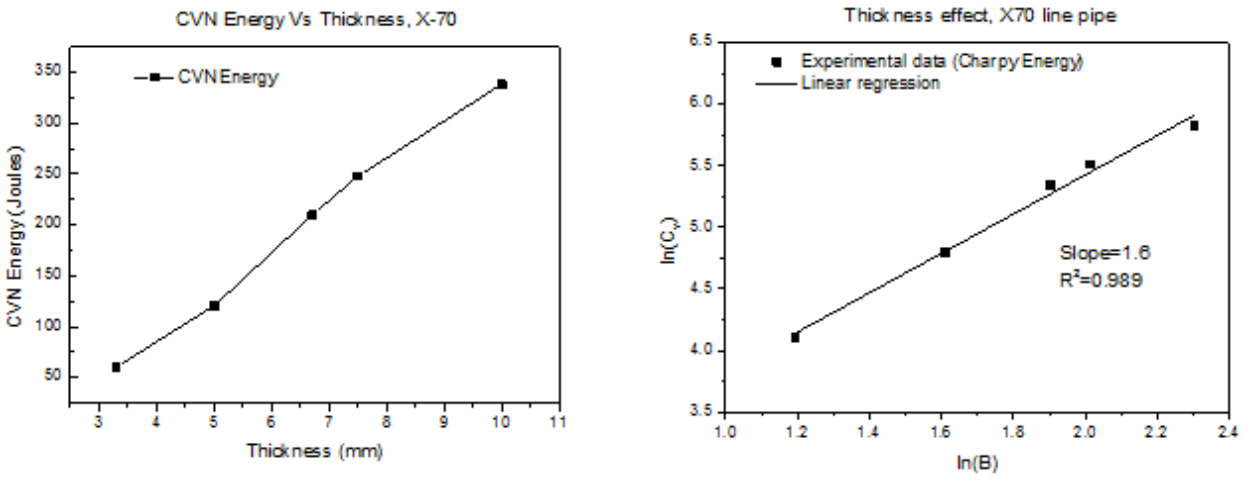

Fig.5.19 CVN energy (C_v) as a function of the specimen thickness (B).

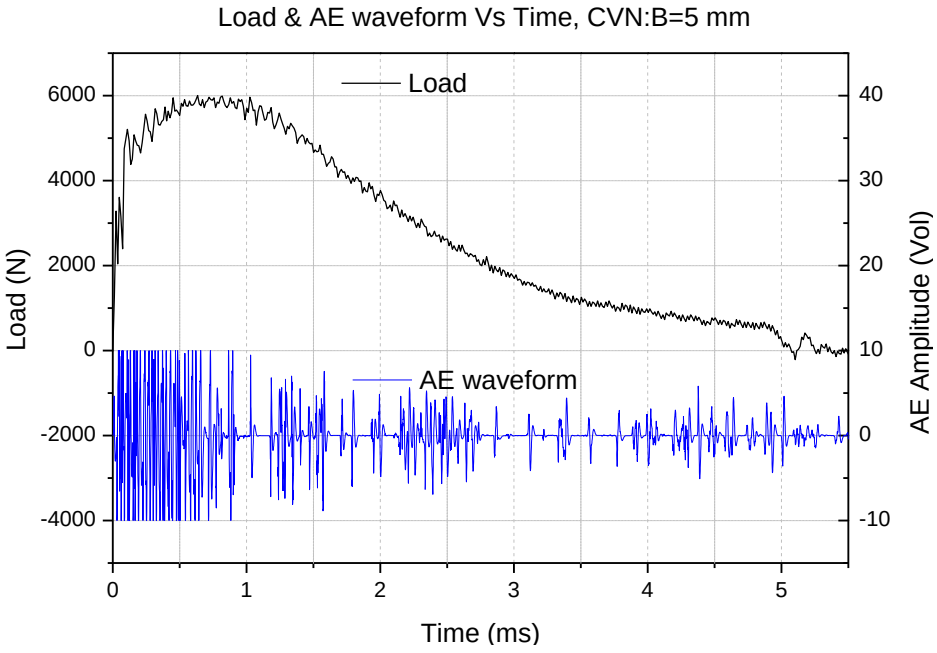

Fig.5.20 Load and acoustic emission waves versus time for CVN Impact test at ambient temperature (B=5 mm).

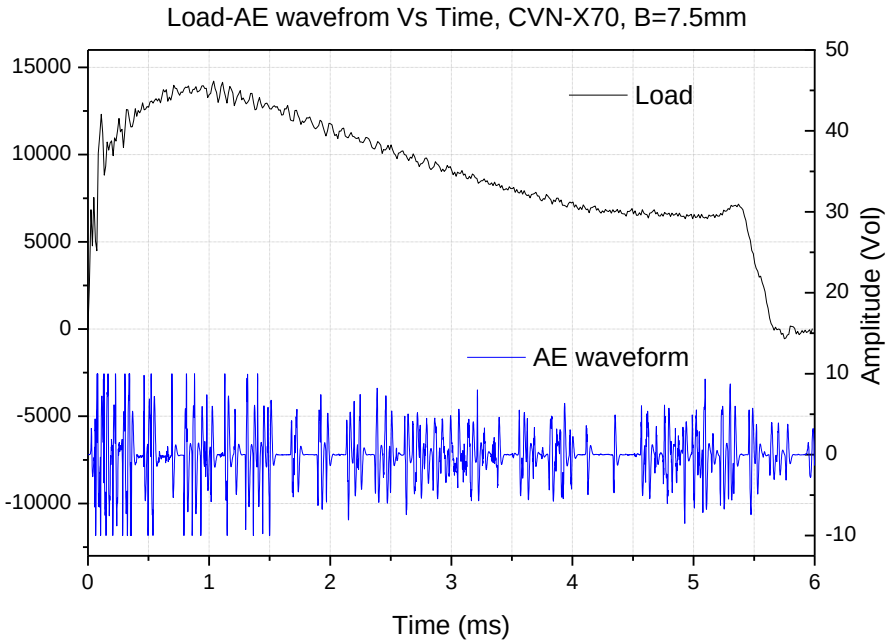

Fig.5.21 Load and acoustic emission waves versus time for CVN Impact test at ambient temperature (B=7.5 mm).

In this study the AE monitoring technique was used to investigate the effect of Charpy specimen thicknesses for the first time.The AE signals of 5 mm and 7.5 mm CVN tests are shown in Fig.5.11 and Fig.5.12, respectively. The AE signal of the 10mm CVN test has been given in Fig.5.8.

For 5 mm specimen, in Region I, a AE signal with a amplitude value of 8 V is observed and the average frequency is in the range of 50-80 kHz. This frequency value is lower than the full size specimen. In Region II, a burst AE signal with 4-6 V amplitude and an100 kHz average frequency is generated before the maximum load. This signal is associated with fracture initiation. In Region III, the load drops and continuous AE signals with the average frequency in the range of 50-100 kHz are generated.

In contrast, for the 7.5 mm specimen, the AE signal with high amplitude of 10 V is generated and the average frequency is in range 75-100 kHz due to hammer impact and general yielding. In Region II, a burst AE signal with short duration and the average frequency of 150 kHz was observed. In Region III, a continuous signal with 4-6 V amplitude and 80-100 kHz average frequency is generated (Fig.5.12). This is consistent with the finding in Ref. [129]. The AE intensity observed in 7.5 mm specimen in Region III (between the maximum load and end of test) is relatively higher compared to the 5 mm specimen in the same region.

Table 5. lists the AE amplitude and average frequency results for three different CVN tests. It can be found that as the specimen thickness decreases from 10 mm to 5 mm, in Region I, AE signal amplitude decreases from 10 V to 8 V and the average frequency is in the range of 50-100

kHz due to the hammer impact and general yielding. In Region II, a burst AE signal is generated due to the ductile initiation. Amplitude value is in the range of 4-6 V and the average frequency decreases from 200 to 100 kHz. In Region III, continuous AE signals are observed due to the slightly (slowly) dropped load. The AE amplitude decreases from 8 V to 4 V and the average frequency decreases from 150 kHz to 50 kHz.

Table 5.5 The AE waveform parameters during CVN Impact test in the studied X70 steel at a various thicknesses.

Sample thickness	Region	Amplitude [Vol]	FFT power spectrum frequency peak [kHz]	Suggested cause of AE
5.0 mm	I	<6	50-80	The hammer impact and general yielding (A)
	II	4-6	~100	Plastic deformation and ductile fracture (A-B)
	III	2-4	80-100	Ductile fracture propagation (B-C)
7.5 mm	I	< 6	75-100	The hammer impact and general yielding (A)
	II	4-6	~150	Plastic deformation and ductile fracture (A-B)
	III	2-4	100-150	Ductile fracture propagation (B-C)
10 mm	I	< 8	~100	The hammer impact and general yielding (A)
	II	<4-6	150-200	Plastic deformation and ductile fracture (A-B)
	III	>4	100-150	Ductile fracture propagation (B-C)

5.4 Determination of crack initiation point

It has been observed by the high speed camera and AE measurement in the SENT tests that the fracture doesn’t initiate at the peak load and it always occurs between the yield point and the

peak point with higher AE amplitude and frequency. In order to further validate the location of fracture initiation, additional quasi-static three point bending tests (TPBT) of X70 line pipe steel were performed using a tensile test machine.

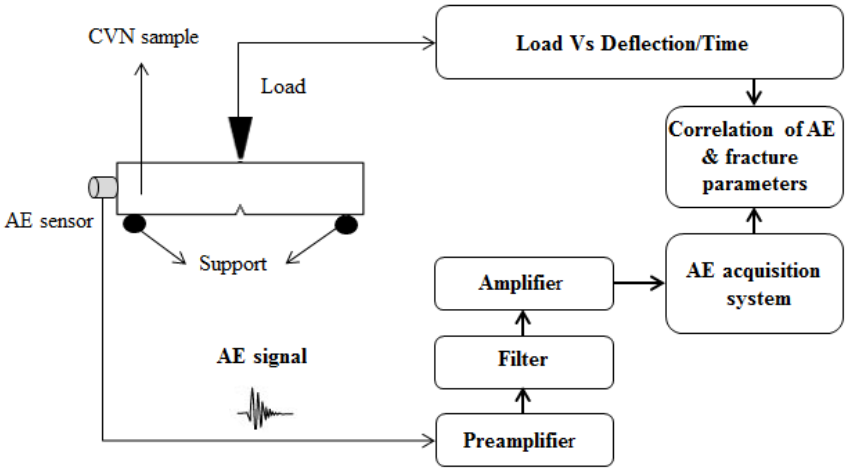

Fig.5.22 A schematic of the TPBT.

A schematic of the TPBT is shown in Fig.5.22. The TPBT specimen has the same geometry as the CVN specimen.

Fig.5.23 (a) shows the load-deflection curve of the TPBT and corresponding AE amplitude distribution. It has been found that before the peak load, a strong AE burst with larger amplitude, marked by a circle in the figure, was observed. High speed video indicates that fracture initiation is responsible for this AE burst event. Fig.5.23 (b) shows its whole AE signal waveform and power spectra. This strong AE signal corresponding to fracture initiation was of 70dB amplitude and an average frequency of 350 kHz.

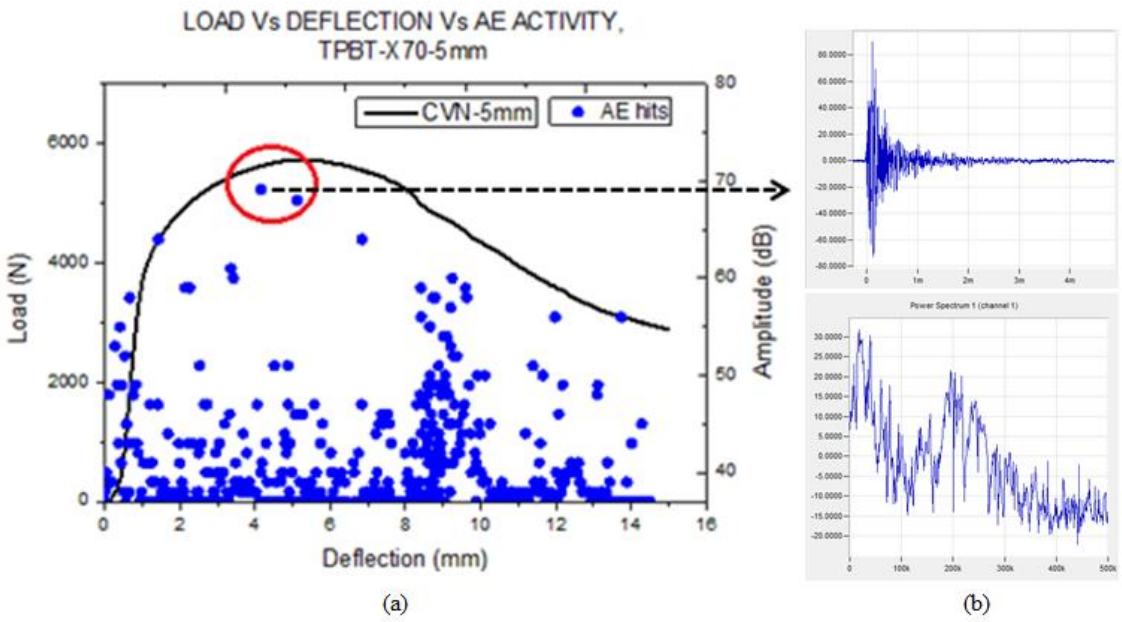

Fig.5.23 (a) AE activity corresponding to the load-deflection curve obtained during testing of three-point bending test; (b) Selected AE signal waveform and power spectrum corresponding to the fracture initiation for 5 mm thick CVN sample.

In the CVN test fracture initiation occurs within a very short time period and the high speed camera cannot be installed to observe the fracture behavior of the specimen. Therefore, it is impossible to determine directly the location of fracture initiation in the CVN load-displacement curve. Fig.5.24 and Fig.5.25 show the results of the CVN tests at room temperatures for B=5mm and B=7.5mm, respectively. It can be seen that there are some strong signals before the peak loads, marked in red in Fig.5.24 and Fig.5.25. It is believed that these signals correspond to the fracture initiation.

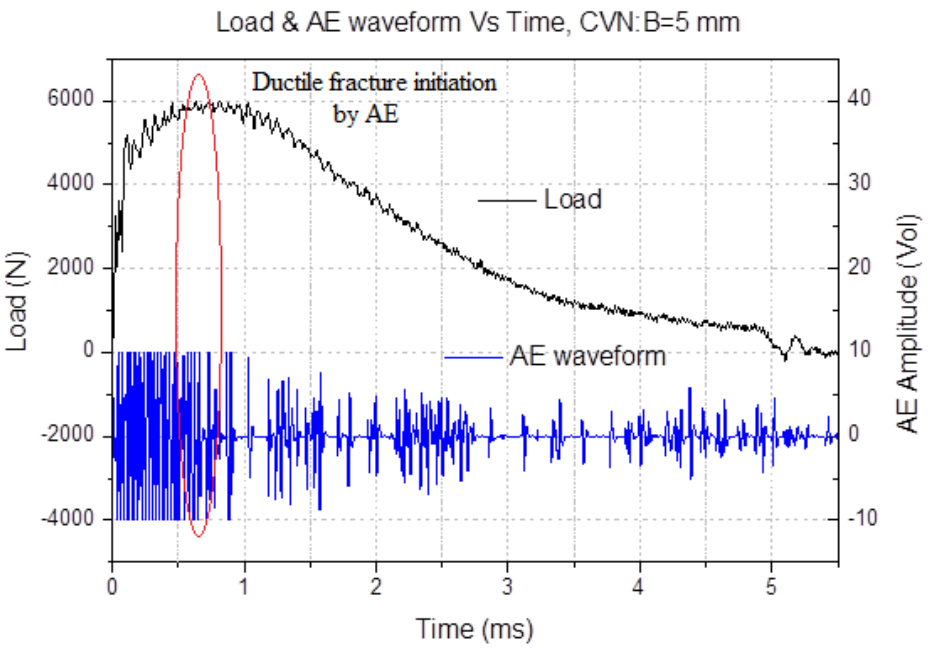

Fig.5.24 Load and AE waveform curves for CVN specimen tested at RT, B=5 mm.

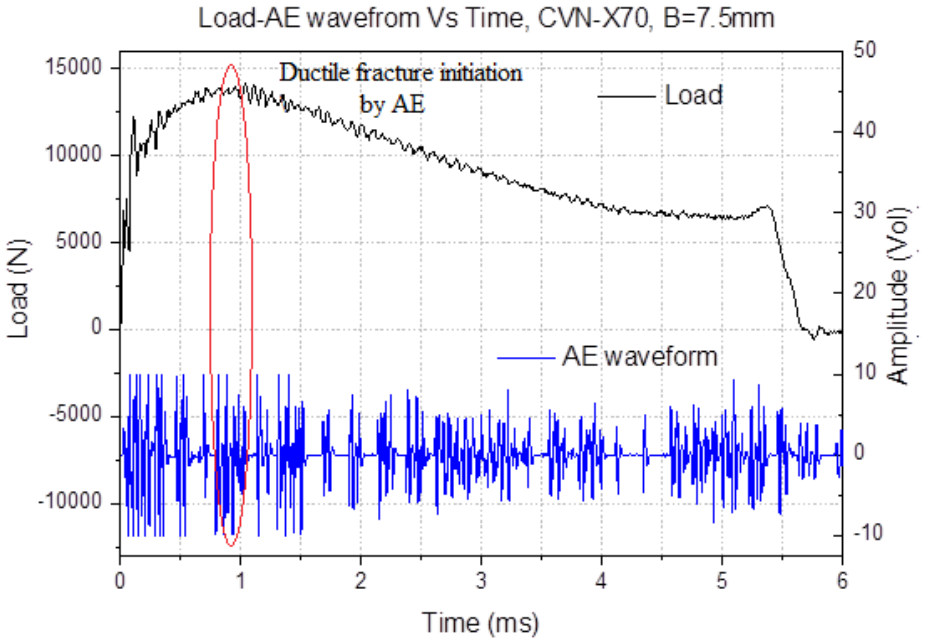

Fig.5.25 Load and AE waveform curves for CVN specimen tested at RT, B=7.5 mm.

5.5 Dependence of acoustic emission on fracture mode

The fracture modes during CVN testing can be predicted using the AE waveform and using the power spectrum analysis. Fig.5.26 shows the AE waves generated from ductile fracture initiation at room temperature had a frequency peak in the range of 80 kHz-150 kHz. This is due to the ductile fracture. In comparison, the AE waves generated at low temperature are of the frequency peaks in the range of 200 kHz-350 kHz (Fig.5.27). This can be explained by occurrence of brittle fracture.

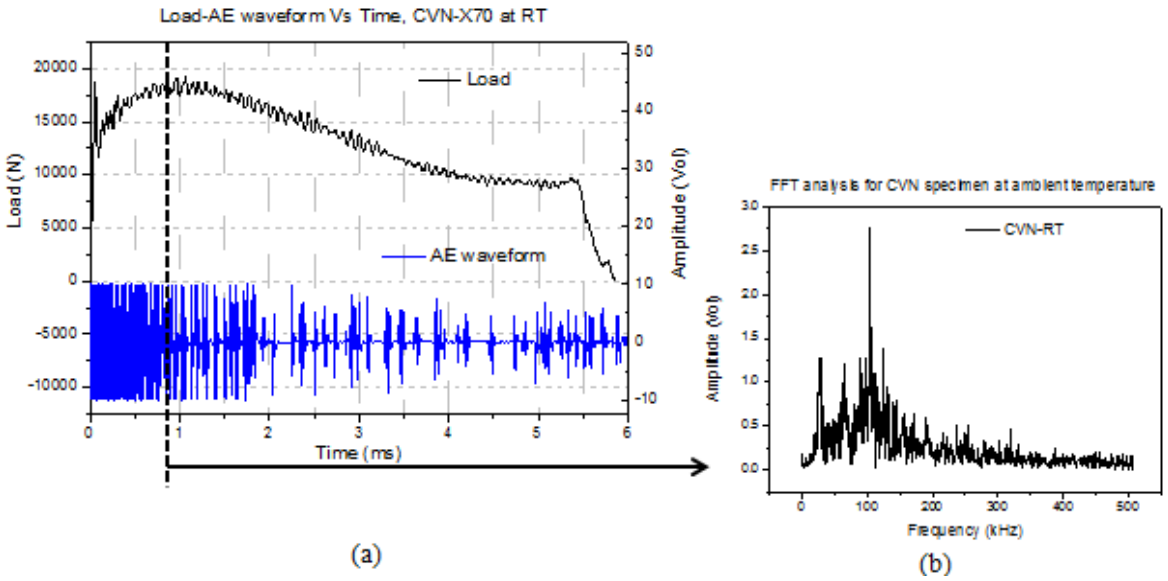

Fig.5.26 (a) Load and AE waveform curves for CVN specimen tested at Room Temperature (B=10 mm), (b) power spectrum obtained by FFT analysis for the time period after fracture initiation.

Thus, the fracture modes can be distinguished by the frequency peaks in the power spectrum. For all cases investigated, the frequency peaks in the range of 50 kHz-200 kHz for the ductile

fractures, and the frequency peaks in the range of 250 kHz-350 kHz are associated with brittle fracture. The specimen temperature vs AE average frequency for the studied X70 line pipe steel is shown in Fig.5.28.

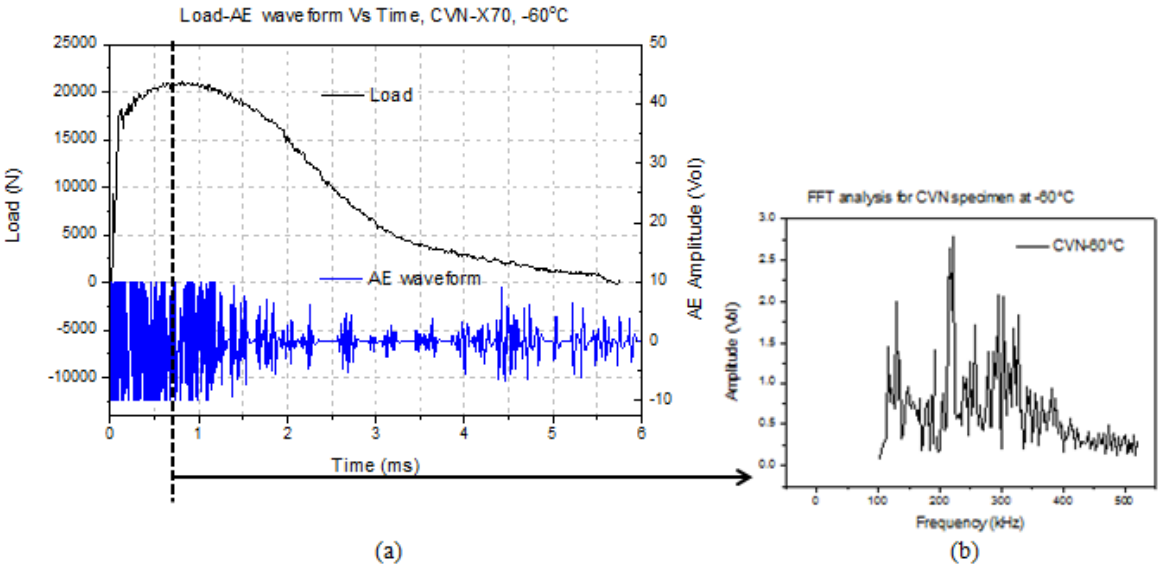

Fig.5.27 (a) Load and AE waveform curves for CVN specimen tested at -60°C (B=10 mm) (b) power spectrum obtained by FFT analysis for the time period after the fracture initiation.

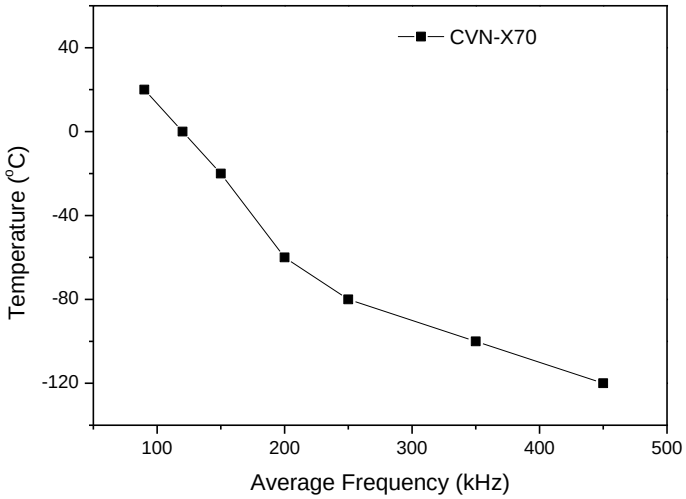

Fig.5.28 The specimen temperature vs AE average frequency for the studied X70 line pipe steel.

5.6 Summary

The research of this chapter can be summarized as follows:

1) The CVN tests of X70 line pipe steels have been conducted at various temperatures. The tests with different specimen thicknesses were also performed at room temperature. In order to analyse the results, the measured load-displacement curves are divided into three regions: Regions I, II and III.
2) In Region I, the AE signal amplitude is in the range of 8-10 Volts and the average frequency is in the range of 50-150 kHz due to the hammer impact and general yielding. In Region II, the burst AE signal average frequency increases from 100-200 kHz to 150-250 kHz as the temperature decreases from the room temperature to -120 ^{o}C. In Region III, the load drops as the fracture propagates. AE signal amplitude is in the range of 6-8 Volts and the average frequency increases form 50-150 to 250-350 kHz as the temperature decreases from room temperature to -120 ^{o}C.
3) As the specimen thickness decreases from 10 mm to 5 mm, in Region I, the AE signal amplitude decreases from 10 Volts to 8 Volts and the average frequency range is in the range of 50-100 kHz. In Region II, the AE signal average frequency decreases from 250 kHz to 100 kHz. In Region III, AE amplitude decreases from 8 Volts to 4 Volts and the average frequency decreases from 150 kHz to 50 kHz.
4) It is impossible to observe directly the fracture imitation in the CVN test. The quasi-static three point bending tests using the same CVN specimen have been carried out. It has been found that the fracture initiates before the peak load. In the CVN tests strong AE

signals were observed before the peak load. It is believed that these strong AE signals correspond to fracture initiation.

5) The fracture mode of Charpy tested specimen can be predicted using AE waveform and Power spectra methodology. It has been found that the fracture modes are characterised by the value of peak frequency. The range of 50 kHz-200 kHz corresponds to ductile fracture and the range of 250 kHz-350 kHz are indicative of the brittle fractures.

6 FEM SIMULATIONS OF PIPELINE FRACTURE TESTS

In this chapter, the FEM modellings are conducted to simulate the SENT and CVN tests. The Gurson-Tvergaard-Needleman (GTN) model is used to predict the nucleation, growth and coalescence of micro voids. The developed FEM models have been validated by comparison with the experimental results. The fracture initiation and propagation during tests are analyzed in details.

6.1 FEM simulation of CVN testing

6.1.1 Finite element model

In the present study, the commercial FEM software "ANSYS/LS-DYNA" with dynamic explicit scheme was used to simulate the CVN tests on the specimens with thicknesses 5 mm, 7.5mm and 10 mm. The Gurson-Tvergaard-Needleman (GTN) model, which has been described in Section 2.2.3, was used to simulate the ductile fracture behavior. The GTN model has been recognized as one of the best ductile fracture models. The stress-strain curve used in the simulation is shown in **Ошибка! Источник ссылки не найден.**. The simulation parameters are shown in Table 6.1.

Table 6.1 GTN parameters used in the simulation.

Simulation parameters	f	f_f	f_c	ε_n	s_n	q_1	q_2
Value	0.000125	0.125	0.015	0.3	0.1	1.5	1

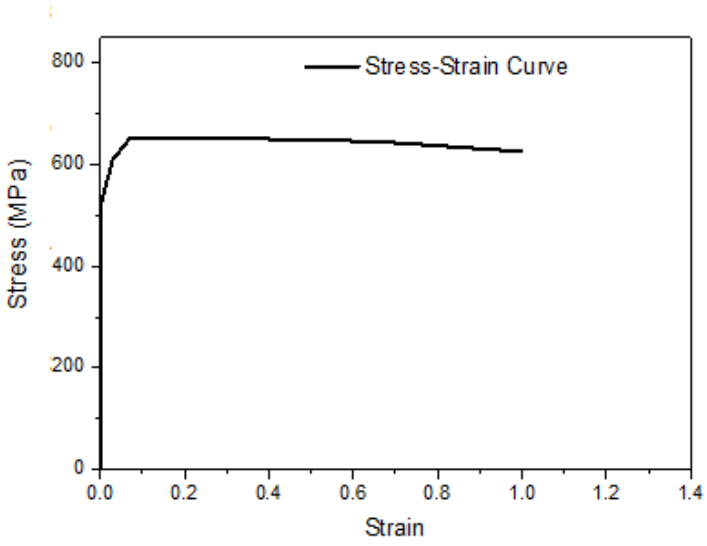

Fig.6.1 Stress-strain curve used in the simulation.

The FEM model utilizing eight-node hexahedral elements for the CVN tests is shown on Fig.6.2. The contact between the sample and the striker was modelled by Coulomb friction with a coefficient of friction equal to 0.1.The total number of elements and node in the simulations are listed in Table 6.2.

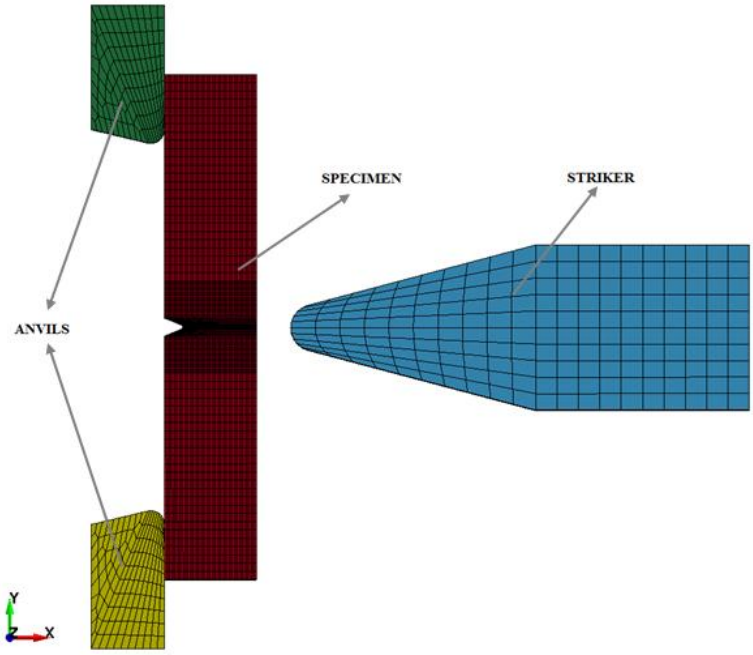

Fig.6.2 A scheme of Charpy V-Notch testing used in finite element simulation.

Table 6.2 Numbers of elements and nodes used in FEM.

Simulation of CVN test	Number of elements	Numbers of nodes
5 mm	146804	158091
7.5 mm	169880	181772
10 mm	175304	187416

6.1.1.1 Simulated Load-displacement/time curves

The FEM simulated and experimental load-displacement curves for CVN specimen with 5 mm thickness are compared in Fig.6.3. The simulated load-displacement curve follows the same trend of the experimental one. The load-time curves have been divided into three regions, namely Regions I, II and III. Region I is the period of elastic deformation. At the boundary between Regioin I and Region II (yeild point), the plastic deformation begins around the crack tip. After the yield point the load increases with the time until the maximum load, which is the boundary between Region II and Region III. In Region III the load decreases with the time.

It can be seen that the simulated yield and peak points are in very good agreement with the experimental results. The simulated curve reaches the maximum load at the same time as the experimental curve. After the peak load both the simulated experimental loads decrease with the time. However, the drop of the simulated load is faster than that of the experimental curve beyond the time of 1ms. As the final stage of the CVN test, the fracture has reached the impacted region between the striker and the specimen. The compressive stress may significantly contribute to the fracture behavior. However, the GTN only considers the effect of the tensile hydrostatic stress on the void growth. This is the reason why there is a difference between two curves in

Fig.6.3. The main focus of the present study is to determine the fracture initiation. The FEM model developed in the present study can give enough accuracy for this purpose.

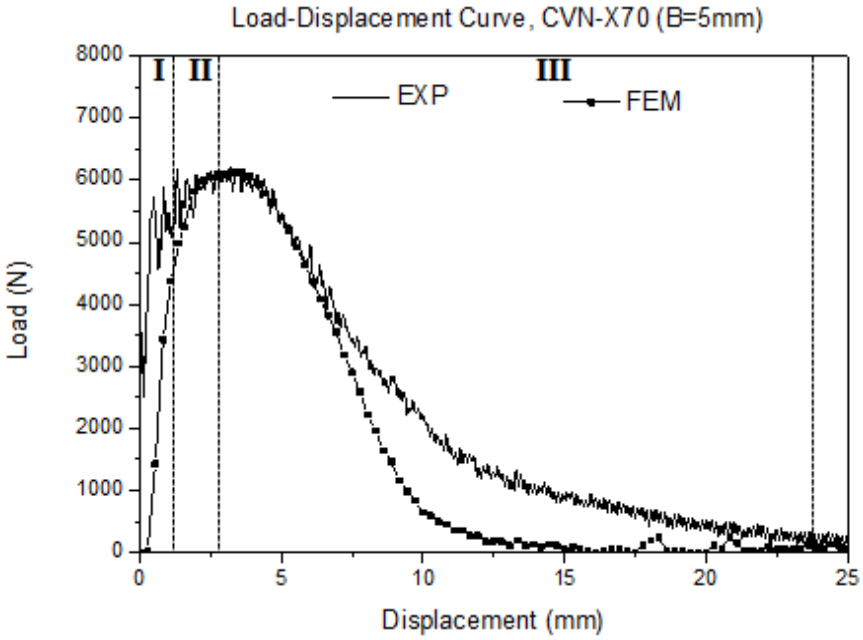

Fig.6.3 Experimental and simulated load-displacement curve at ambient temperature (B=5 mm).

Fig.6.4shows the contours of the effective von Mises stress on the side surface (Fig.6.4(a)) and the fracture surface (Fig.6.4 (b)) at the selected times. At t=0.25 ms, the stress concentrates around the crack tip and the contact area between the striker and the specimen, which correponds to the yield point. At t=0.7 ms, the fracture just initiates, as shown in Fig.6.4 (b). It can be seen in Fig.6.4 (b) that the fracture has propagated to a short distance at the peak load (t=1.65 ms). At t=2.85 ms, as shown in Fig.6.4 (b), the fracture reaches the region near the contact between the striker and the specimen. It is clear from the simulated results that the fracture initiates before the peak load, which is consistent with the prediction of the AE measurment.

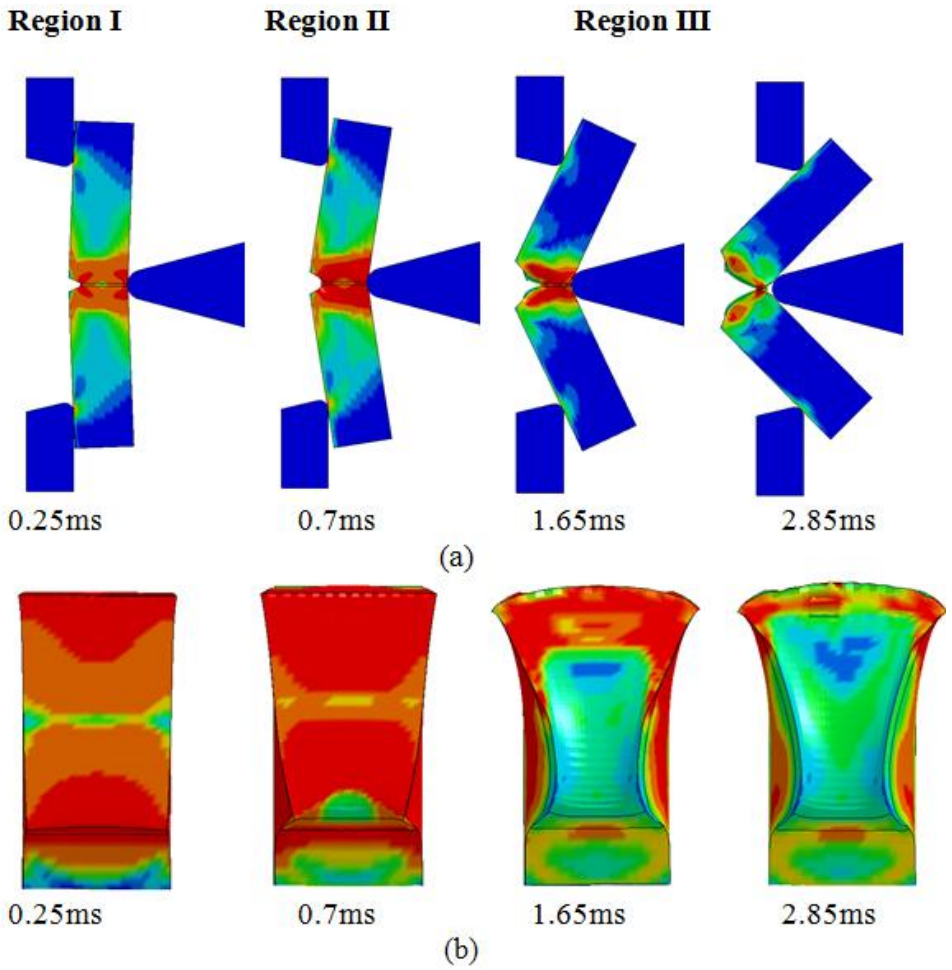

Fig.6.4 Effective stress distributions at a selected instant time for three regions: (a) stress distribution on Charpy specimen, (b) stress distribution on fracture surface.

Fig.6.5 shows simulated load-time curves for the three specimens with different thicknesses. As the thickness increases the load-time curve moves up. The CVN energy (Cv) can be calculated by integrating the load-time curve. The calculated CVN energy (Cv) is plotted in Fig.6.6 as a function of the specimen thickness (B). The best function to fit the calculated Cv-B relationship is $Cv \propto B^{1.45}$. The exponent of 1.45 obtained from the simulations is close to that determined by the experimental results.

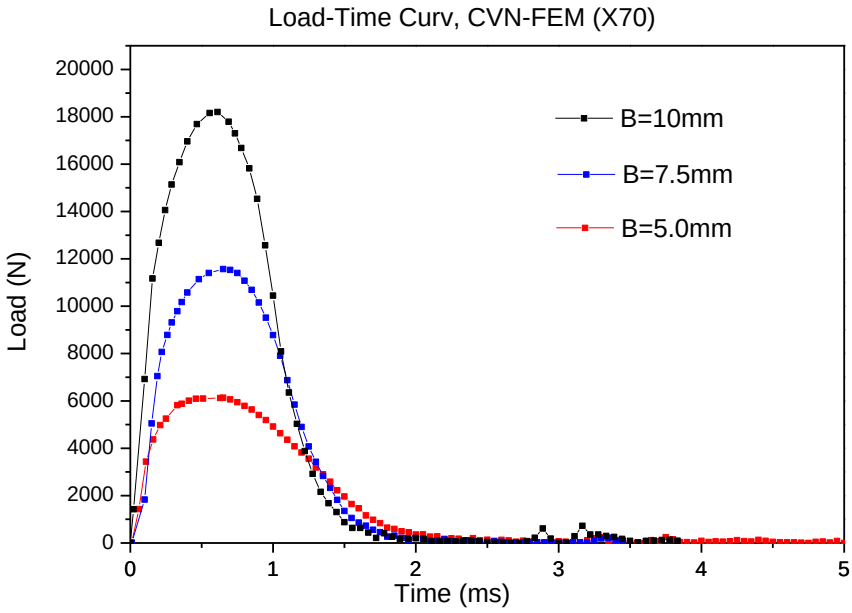

Fig.6.5 Simulation Load-Time Curve at ambient temperature for a various sample thicknesses.

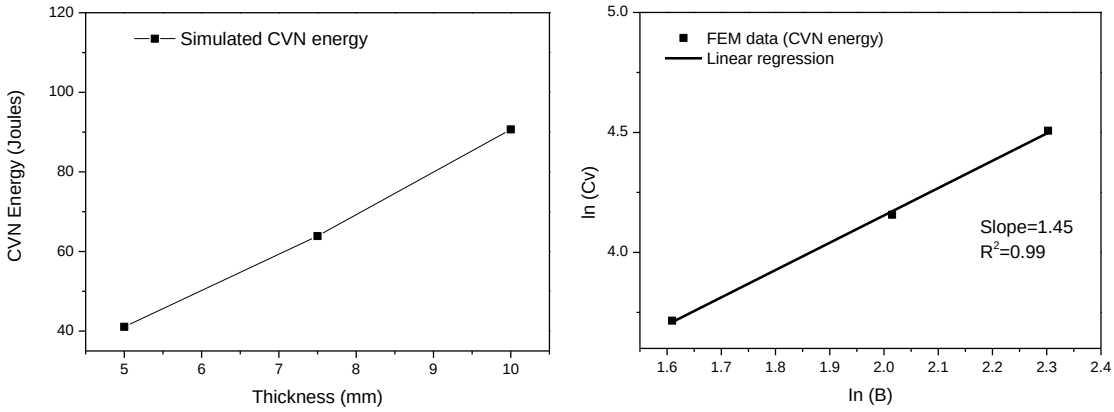

Fig.6.6 Simulated energy (C_v) as a function of the specimen thickness (B).

6.1.2 Analysis of crack initiation and propagation

The simulation result of 5 mm thickness specimen, as shown in Fig.6.7, indicates that the fracture initiates before the peak load. A black dot is marked for fracture initiation. The inset in Fig.6.7gives the contour of the von Mises stress on the A-A plane at the time indicated by the

black dot on the load-displacement curve. It is clear that the fracture has nucleated at this time, which is before the peak load. Fig.6.8 shows the load-displacement curve for the 7.5 mm specimen. Fig.6.9 shows the results of the 10 mm specimen. The same conclusion can be drawn that the fracture initiates before the peak load.

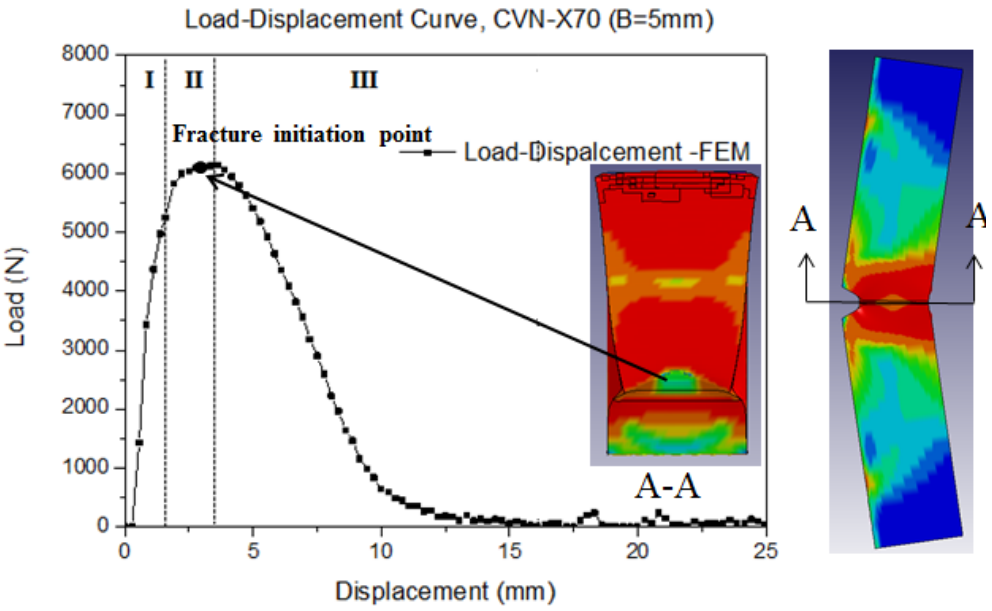

Fig.6.7 Fracture initiation point determination by FEM simulation for CVN specimen: 5 mm specimen.

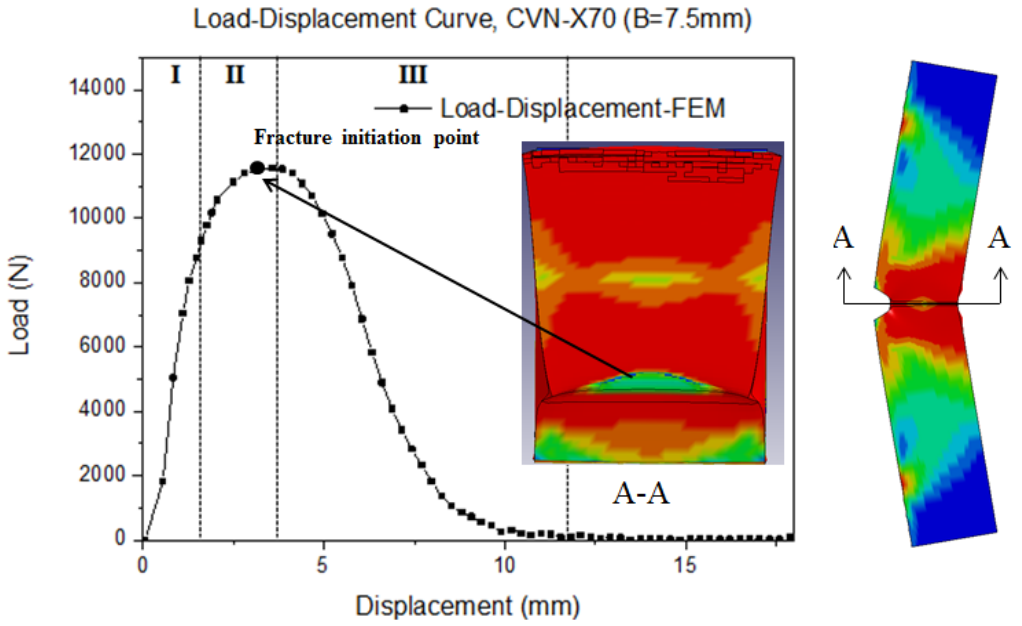

Fig.6.8 Fracture initiation point determination by FEM simulation for CVN specimen: 7.5 mm specimen.

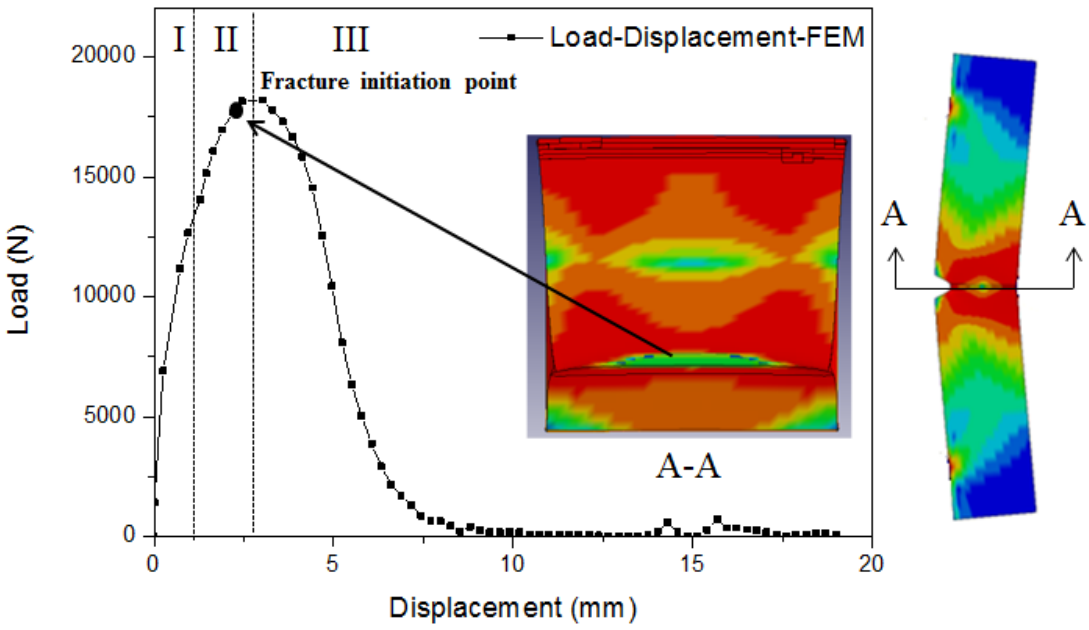

Fig.6.9 Fracture initiation point determination by FEM simulation for CVN specimen: 10 mm specimen.

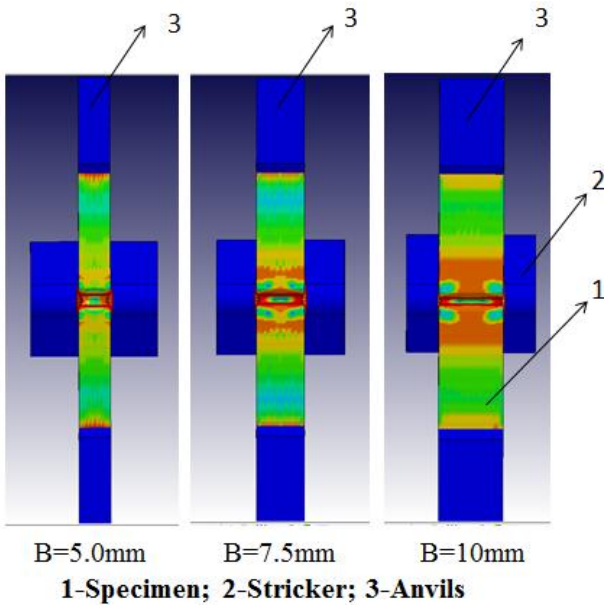

Fig.6.10 Fracture initiation at instant time for CVN specimen with a various thicknesses.

Fig.6.10 shows the distribution of the effective von Mises stress of the simulated specimens with the three different thicknesses observed from the bottom of the specimen at the time of the fracture initiation. It can be seen that the fracture initiates near the notch tip in the middle thickness of the specimen. Table 6.3 lists summary of load values for CVN simulation with a various thicknesses.

Table 6.3 Summary of simulation results for CVN specimen with a various thicknesses.

Specimen Thickness [mm]	Load at general yield P_{yield}[N]	Load at Crack initiation $P_{c.i}$[N]	Load at maximum P_{max}, [N]
5.0	4856	5876	6055
7.5	7848	13042	13952
10	16874	19055	20902

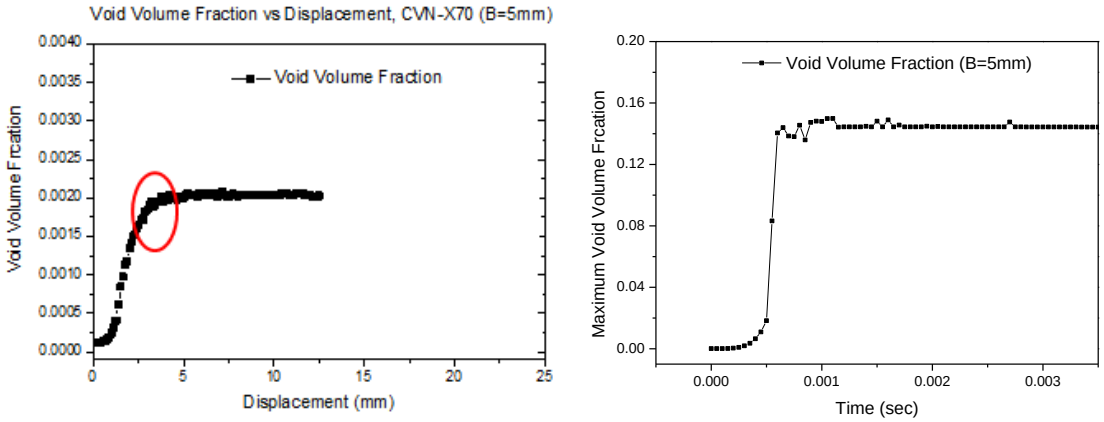

Fig.6.11 Void Volume Fraction as function of displacement for CVN specimen: B=5mm.

In the GTN model, the void nucleation and the void growth are described by the void volume fraction. The condition of ductile crack initiation is given by the critical void volume fraction [130]. As described in Eq.(2.5), f_c is the critical void volume fraction at which voids coalesce. Once the calculated void volume fraction exceeds f_c the material will quickly break. f_c is set to be 0.015. Fig.6.11 and Fig.6.12 show the average void volume fraction as a function of displacement for the CVN specimens of 5 mm thickness and 7.5 mm thickness, respectively. It can be seen from Fig.6.11 and Fig.6.12 that the average value of void volume fraction reaches at maximum point (as marked by a red circle) when the fracture is initiated.

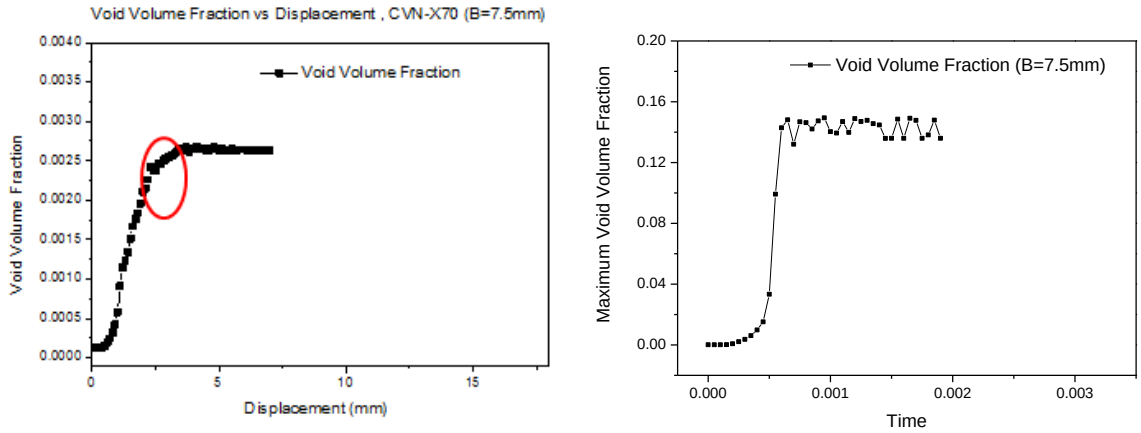

Fig.6.12 Void Volume Fraction as function of displacement for CVN specimen: B=7.5mm.

All the simulations of the CVN tests predict that the fracture initiation occurs before the peak load. This confirms the observations of the AE measurement conducted in Section 5.4. When the fracture initiates, the connected cross section area of the specimen is reduced and the load required to deform the material decreases. Therefore it is generally considered that the fracture initiation corresponds to the peak load. However, it should be noted that after the fracture initiation the material is still subjected to work-hardening. The work-hardening effect compensates the decrease of the load caused by the fracture initiation, and then delays the occurrence of the peak load.

Separation of the fracture initiation energy and fracture propagation energy plays an important role in research of the pipeline fracture control. From the present study, it has been found that using the peak load point to separate two energy components is not accurate. The AE analysis conducted in the present thesis depicts that there is a strong hit before the peak load, corresponding to the fracture initiation. Therefore, this thesis recommends that the AE

measurement can be used to identify the fracture initiation, rather than the peak load point, in the future pipeline research.

6.2 FEM simulation of SENT testing

The objective of this study is to carry out a three dimensional finite element fracture simulation that allows the investigation of fracture processes of the SENT tests with GNT micro-mechanical fracture models.

6.2.1 Finite element model

In the present study, the commercial FEM software "ANSYS/LS-DYNA" with dynamic explicit scheme was used to simulate the SENT test. FEM model utilizing eight-node hexahedral elements for the SENT test is employed. The simulation model is shown in Fig.6.13. The total number of elements and nodes in the simulations are listed in Table 6.4.

Table 6.4 The total number of elements and nodes.

	Number of elements	Numbers of nodes
Simulation of SENT test	129640	140794

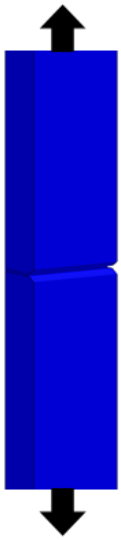

Fig.6.13 A scheme of SENT specimen used in finite element simulation.

The finite element analysis of the SENT specimen was performed using the mesh size of 0.2 mm around the notch area. A constant displacement rate of 20 mm/min was applied in the simulation. The simulation parameters are shown in Table 6.5. The constant parameters (q_1,q_2) in Gurson-Tvergaard yield function is presented by Tveergard have been applied by many studies for the ductile fracture.

Table 6.5 GTN parameters used in the simulation.

GTN parameters	f	f_f	f_c	ε_n	s_n	q_1	q_2
Value	0.000125	0.06	0.0055	0.3	0.1	1.5	1

6.2.1.1 Simulated Load-displacement/time curve

Typical load vs displacement/time curve obtained from the FEM simulation is shown in Fig.6.14.

Similar to the analysis of the experimental results, the load-displacement curve is divided into three regions: I-before the yield point, II-between the yield point and the peak point, and III-after the maximum point till the final fracture. Four points, Points A, B, C and D, are marked in Fig.6.14.

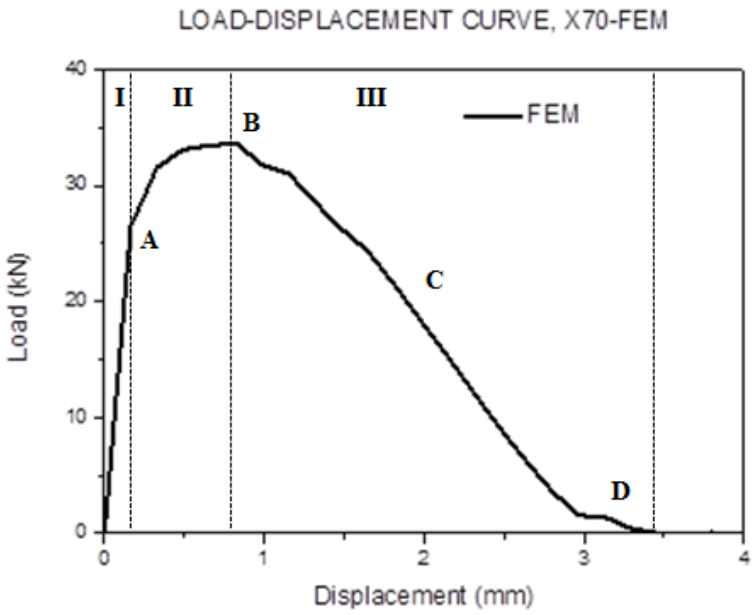

Fig.6.14 The simulated load-displacement curve, SENT-X70

It can be seen in Fig.6.14 that the load increases linearly with the displacement in Region I. At point A, which is the yield point, the material at the front of notch area starts to be deformed plastically.In Region II, from Point A to Point B, the load continuously increases with the displacement. In Region III, the load decreases slightly while the crack propagates and the microviod comfluence exists. In Region III the specimen area reduces and the necking is observed. At Point D, the final separation is observed. FEM simulated load valuesare summarised in Table 6.6.

Table 6.6 Summary of simulation results for the SENT specimen.

Load at yield $P_{yield,}$ [N]	Load at crack initiation point $P_{c.i,}$ [N]	Maximum load P_{max}, [N]
24855	33859	34058

Fig.6.15 compared the specimen geometries predicted in the simulation and recorded by high speed video camera for the four selected points. It can be seen that they are in reasonably good agreement.

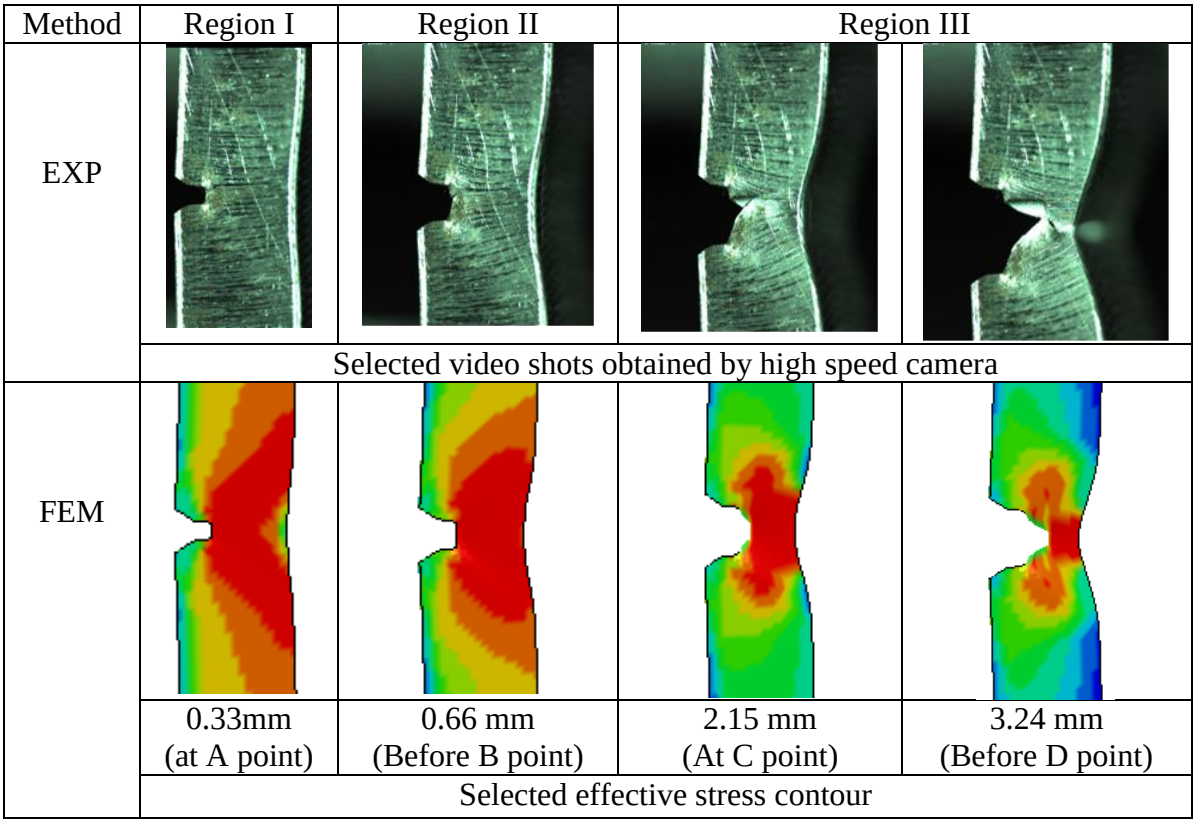

Fig.6.15 Fracture process of pipeline steel during SENT testing: Experiment and FEM simulation.

Fig.6.16 shows the simulated SENT fracture surface and the experimentally tested one. They are in very good agreement. The width extraction and shear fracture area can be observed in both pictures.

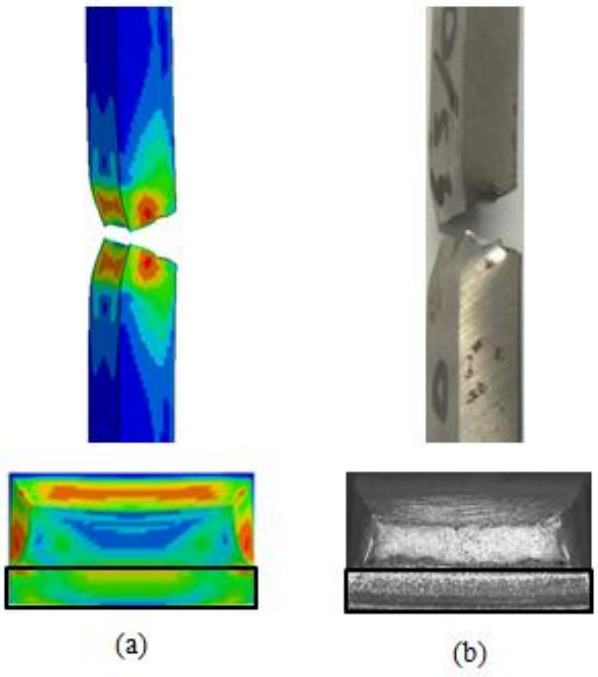

Fig.6.16 The fractured SENT specimen: Simulated specimen (a); tested specimen (b).

6.2.2 Analysis of crack initiation and propagation

The fracture simulation provides detailed information of the fracture initiation and propagation in a ductile SENT specimen. It has been found that the crack initiates at the displacement of 0.7 mm, which has been marked by a red circle in Fig.6.17. The effective von Mises stress distribution and fracture morphology corresponding to the crack initiation is also shown in Fig.6.17. It is clear that, at this displacement, a crack nucleates at the notch tip. This simulation result confirms the experimental observations that the fracture initiates prior to the peak load.

After the fracture initiation, the load still continues to increase. This is due to the work hardening effect induced by the plastic deformation.

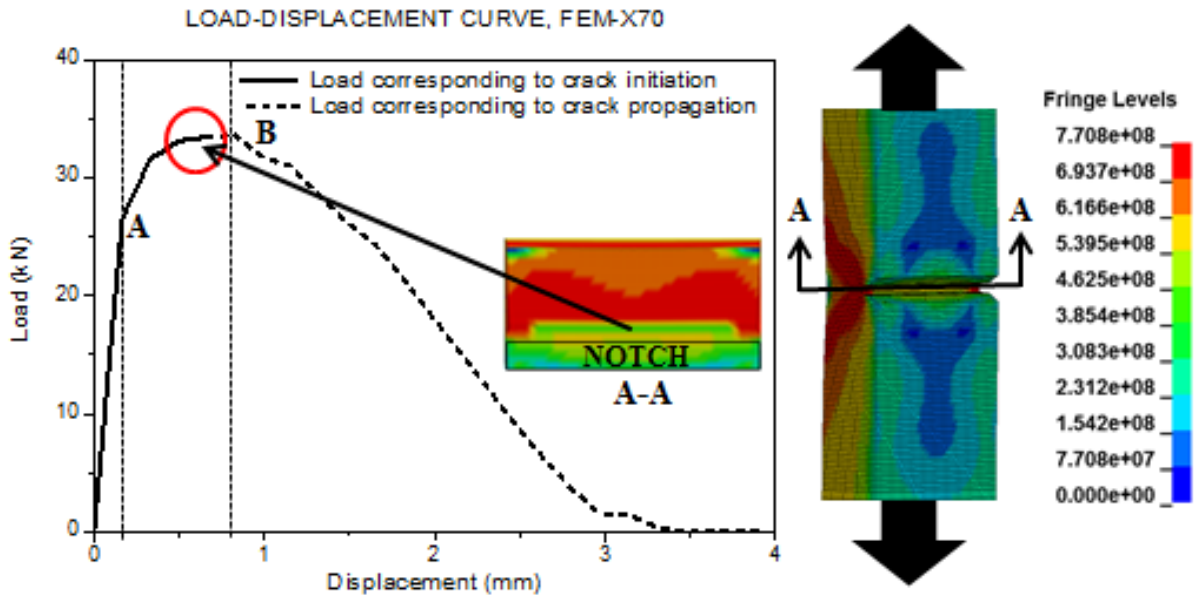

Fig.6.17 Fracture initiation point determination by FEM simulation for SENT specimen.

Fig.6.18 shows that the effective von Mises stress distribution and fracture morphology corresponding to the crack propagation from Point B to Point D. It can be seen in Fig.6.18 that once the fracture is initiated (before B point), the crack propagates rapidly. After Point B the load decreases slightly. At Point C the fracture area continuously increases and the specimen completely separates at Point D.

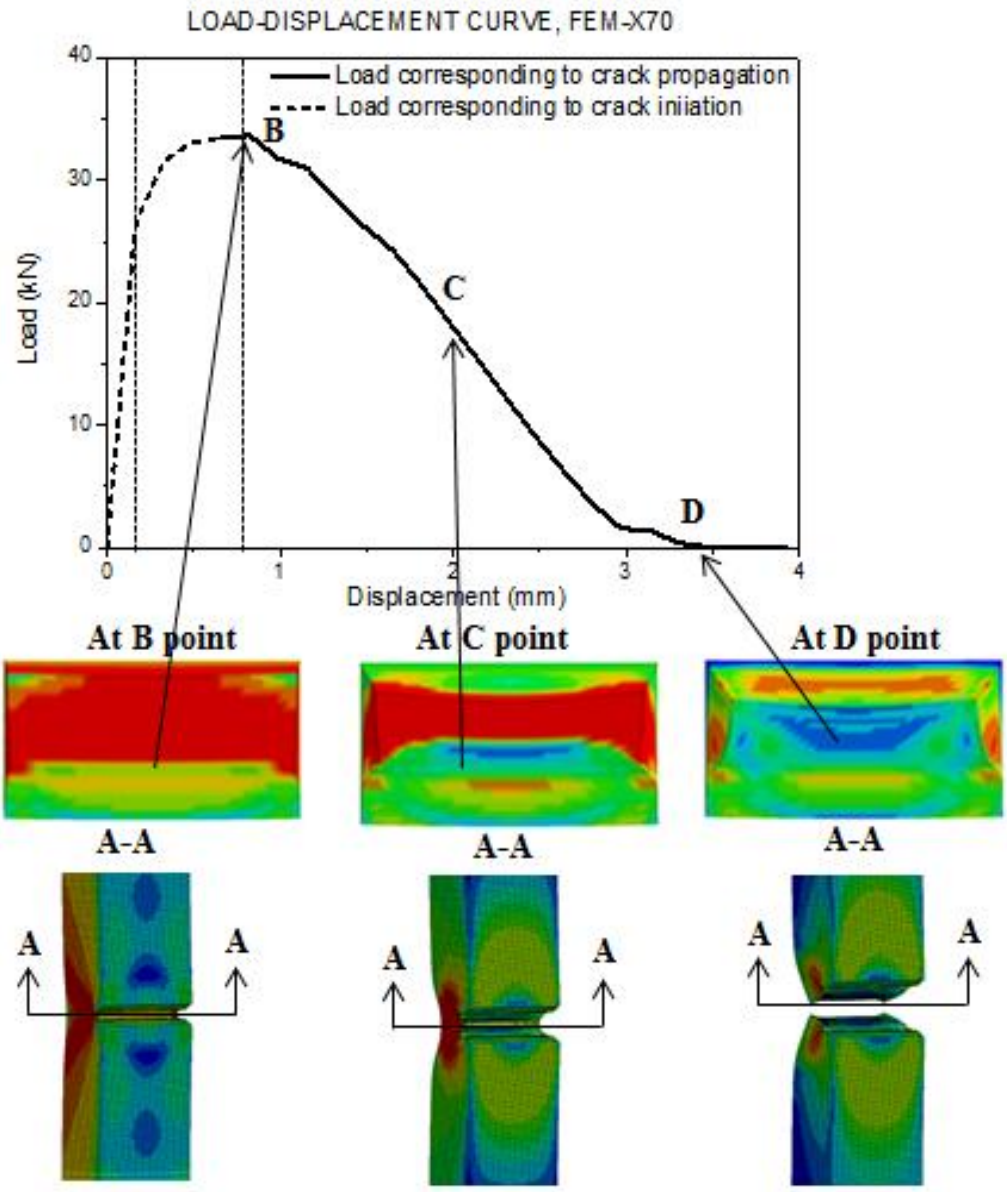

Fig.6.18 Fracture propagation by the FEM simulation for the SENT specimen.

6.2.3 Summary

The research of this chapter can be summarized as follows:

1) Three dimensional fracture models based on the finite element method have been developed to simulate the SENT and CVN tests of the line pipe steel using the Gursen-Tvergaard-Needleman fracture constitutive model.
2) The simulated results are in good agreement with the experimental results in terms of stress distribution and fracture morphology for both SENT and CVN tests. The simulated specimen is capable to identify the major characteristics of SENT and CVN specimen, such as the fracture tunneling and the shear lip
3) The fracture initiation can be predicted by the FEM simulation. It has been found that the fracture initiates before the maximum point on the load-displacement curve for both tests.

7 CONCLUSIONS AND RECOMMENDATIONS

7.1 Conclusions

In this thesis, the dynamic fracture behaviour of the line pipe steel was studied by CVN impact and SENT tests in conjunction with AE monitoring.Variations in AE features were analyzed using the Wave Form and Power Spectrum methodologies and correlated to fracture initiation and load-time/load-deflection curves for both tests. The fracture initiation point was identified by a sudden change in the AE activity, observed prior to the maximum load point on the load-displacement curve. FEM simulations of the CVN and SENT tests were carried out using the commercial software 'ANSYS/LS-DYNA' withthe Gurson-Tveergaard-Needleman (GTN) fracture model.

The major conclusions of the PhD study are summarised as follows:

For Single edge-notched tension test:

1) The AE monitoring technique was used for the first time during the SENT test of X70 and X80 line pipe steels.
2) It was found that the AE activity started before the yield point (Region I) due to stress concentration at the crack tip and increased suddenly before the maximum load is reached (Region II) due to the fracture initiation. Towards the end of test (Region III), the AE hit density increased again.

3) With an increase in the strain rate and a decrease in testing temperature, AE activity increased during SENT. A significant increase in AE hit density was observed in Region I and Region III at -20 ^{o}C. A continuous type of AE signal with an amplitude of 30-40 dB dominated in Region I for lower strain rate compared to the same region for higher strain rate. A strong burst signal with an amplitude of 50-70 dB was observed in Region II and at the final stage of Region III in all the tests.
4) The fracture initiation point can be detected by a sudden change in the acoustic emission activity. It was found that the fracture initiation in the studied steel resulted in a burst AE signal with a 65-75 dB amplitude and a 300-350 kHz average frequency prior to the maximum point of the load-displacement curve. The fracture initiation was also predicted by the FEM simulation of the SENT test. The FEM simulation showed a good agreement with the experimental results.
5) Crack growth rate was predicted using its relationship with the AE count rate. With an increase in the crack growth rate the AE count rate increased. The amount of small voids decreased and the amount of large voids increased with an increase in temperature and a decrease in the strain rate. The AE average frequency was observed decreasing with an increase in the void size.

For Charpy V-notch test:

1) CVN tests on X70 line pipe steels were conducted at various temperatures. The tests with different specimen thicknesses were also performed at room temperature. In order to

analyse the results, the measured load-displacement curves were divided into three regions: Regions I, II and III.

2) As the specimen temperature decreased from room temperature to -120 °C, the average frequency of the burst-type AE signals increased from 80 kHz to 150 kHz in Region I before the yield point, from 250 kHz to 350 kHz in Region II after the yield point and before the maximum load point, and from 150 kHz to 250 kHz in Region III after the maximum load point till the end of the test.
3) The ductile-to-brittle transition temperature (DBTT) was found to be in the range of -60 ^{o}C to -80 ^{o}C for the tested steel. Along with this transition in fracture behavior, the AE average frequency increased with a decrease in temperature. A sudden drop in the load was observed at -60 ^{o}C due to the occurrence of brittle fracture that generated a burst-type AE signal with an average frequency of 350 kHz.
4) Charpy specimens with various thicknesses such as 5 mm, 7.5 mm and 10 mm were tested for the first time using the AE monitoring technique. With a decrease in specimen thickness from 10 mm to 5 mm the AE average frequency decreased from 150 kHz to 50 kHz.
5) It is impossible to observe directly the fracture initiation in the CVN test. The quasi-static three-point bending tests using the same CVN specimen were carried out. It was found that the fracture initiated before the peak load. In the CVN tests strong AE signals were observed before the peak load. It is believed that these strong AE signals corresponded to fracture initiation.
6) The fracture mode of the Charpy-tested specimen can be predicted using AE waveform and Power spectra methodologies. It was found that the fracture modes were

characterized by the value of the peak frequency: 50 kHz-200 kHz range corresponded to the ductile fracture and the 250 kHz-350 kHz range corresponded to the brittle fracture.

7.2 Recommendations

Based on the conclusions of this work the following recommendations are made for future research:

1) The present study was mainly performed for X70 line pipe steels. More investigations should be carried out for other grades of steel.
2) The effect of low temperature (below -20^{o}C) on the fracture behaviour of the line pipe steels during SENT should be investigated numerically and compared to the experimental results obtained from this study.
3) AE streaming as a method of signal analysis for CVN testing should be considered.
4) 2D/3D modelling of AE wave propagation needs to be carried out. FEM simulation of the AE from the fracture initiation and propagation for both the SENT and CVN tests could be done to link the fracture mechanics to the AE signals.
5) From the present study, it has been found that using the peak load point to separate two energy /the fracture initiation and fracture propagation/ components is not accurate. The AE analysis conducted in the present thesis depicts that there is a strong hit before the peak load, corresponding to the fracture initiation. Therefore, this thesis recommends that the AE measurement can be used to identify the fracture initiation, rather than the peak load point, in the future pipeline research.

References

[1] G. D. Fearnehough, "Fracture propagation control in gas pipelines: A survey of relevant studies," *International Journal of Pressure Vessels and Piping,* vol. 2, pp. 257-282, 1974.

[2] L. E. Hood, "Fracture of steel pipelines," *International Journal of Pressure Vessels and Piping,* vol. 2, pp. 2086-2102, 1974.

[3] A. B. Rothwell, "Fracture propagation Control for gas pipeline-Past, Present and Future," *Pipeline Technology* vol. 01, pp. 387-405, 2000.

[4] D. J. Horsley, "Background to the use of CTOA for prediction of dynamic ductile fracture arrest in pipelines," *Engineering Fracture mechanics,* vol. 70, pp. 547-552, 2003a.

[5] W. L. Server, "Instrumented Charpy test review and application to structural integrity," pp. 205-212, 2002.

[6] S. Kawaguchi, *et al.*, "Modified equation to predict leak/rupture criteria for axially through-wall notched X80 and X100 linepipes having a higher Charpy energy," *Journal of Pressure Vessel Technology,* vol. 128, pp. 572-580, 2006.

[7] R. K. Miller, *Acoustic emission testiing*: The McGraw-Hill Companies, Inc, 2003.

[8] C. U. Grosse and M. Ohtsu, *Acoustic emission testing*. Heidelburg: Springer, 2008.

[9] A. G. Kostryzhev, *et al.*, "Acoustic emission monitoring of split formation during Charpy impact testing of high strength steel," *Materials Science and Technology,* vol. 28, pp. 240-242, 2012.

[10] K. Ono, "Current understanding of mechanisms of acoustic emission," *Journal of Strain Analysis for Engineering Design,* vol. 40, pp. 1-15, 2005.

[11] B. Muravin and M. F. Carlos, "Guide for development of acoustic emission application for examination of metal structure," *J. Acoustic Emission*, vol. 29, pp. 142-148, 2011.

[12] W. Sachse, *et al.*, *Acoustic emission: current practice and future directions*: ASTM, 1991.

[13] A. Cosham and R. J. Eiber, "Fracture control in carbon dioxide pipelines - the effect of impurities," in *Proceedings of the Biennial International Pipeline*, 2008, pp. 229-240.

[14] W. A. Maxey, "Fracture initiation, propagation and arrest," presented at the Applied Mechanics of Materials Section, Battelle's Columbus laboratories, 1973.

[15] D. L. Rudland, "Determination of Conditional Probability of Dynamic Ductile Axial Crack Arrest for Conventionally-Rolled, Lower-Toughness Linepipe Materials," *Journal of Pressure Vessel Technology*, vol. 127, pp. 143-150, 2005.

[16] B. Leis and R. J. Eiber, "Relationship Between Apparent Charpy V-Notch Toughness and the Corresponding Dynamic Crack-Propagation Resistance," presented at the International Pipeline Conference, Canada, 1998.

[17] A. Cosham and R. J. Eiber, "Fracture propagation in CO2 pipelines," *The Journal of Pipeline Engineering*, vol. 4, pp. 281-291, 2008.

[18] M. A. Cabral and M. J. Kimber, "Pipeline Fracture experiences in Australia and North America," *Pipeline Fracture Experience*, vol. 3, pp. 1-21, 1997.

[19] X. K. Zhu and B. N. Leis, "Ductile Fracture Arrest Methods for Gas Transmission Pipeline Using Charpy Impact Energy or DWTT Energy," *Journal of Pipeline Engineering*, vol. 12, 2013.

[20] A. B. Rothwell, "Fracture propagation control for gas pipelines—past, present and future," *In: Denys R, editor. Proceedings of the 3rd International Pipeline Technology Conference*, vol. 1, pp. 387–405, 2000.

[21] R. M. Andrews and A. D. Batte. Development in Fracture Control Technology for Gas Pipelines Utilising High Strength Steels [Online].

[22] A. Cosham and D. G. Jones, "Don't drop the drop weight tear test," *Pipeline Technology Conference*, pp. 1-18, 2009.

[23] A. B. Rothwell, *et al.*, "Requirements for control of ductile fracture propagation in large-diameter gas transmission pipelines," *Journal of Materials for Energy Systems*, vol. 2, pp. 30-40, 1980.

[24] R. O. Richie, *et al.*, "On the relationship between critical tensile stress and fracture toughness in mild steel," *Journal of the Mechanics and Physics of Solids*, vol. 97, pp. 1409-1416, 1973.

[25] G. Demofonti, *et al.*, "Transition temperature determination for thick wall line pipe," in *Proceedings of the International Pipeline Conference, IPC*, Calgary, Can, 1998, pp. 699-704.

[26] R. J. Eiber, "Correlation of full scale tests with laboratory tests," presented at the 3rd Symposium on Line Pipe research, 1965.

[27] D. L. Rudland, *et al.*, "First major improvement of the two curves ductile fracture model part I main body," U.S Departmnet of transportation research and special programs administration Washington DC and Pipeline research council international2007.

[28] G. Buzzichelli and L. Scopesi, "Fracture propagation control in very high strength gas pipelines," *Revue De Metallurgie-Cahiers D Informations Techniques*, vol. 97, pp. 1409-1416, 2000.

[29] A. B. Rothwell, "Fracture propagation control measures for gas pipelines," in *Proceedings of international seminar on fracture control in gas pipelines*, 1997.

[30] M. Di Biagio, *et al.*, "Full scale fracture propagation testing on dense phase CO2 pipeline," in *20th JTM*, Paris, 2015, pp. 1-12.

[31] X. K. Zhu and B. N. Leis, "CVN and DWTT energy methods for determining fracture arrest toughness of high strength pipeline steel," in *9th International pipeline conference*, 2012.

[32] X. K. Zhu, "Review of fracture control technology for gas transmission pipelines," in *Proceedings of the 2014 10th Internatinal Pipeline Conference*, Calgary, 2014.

[33] W. A. Maxey, *et al.*, "Ductile fracture arrest in gas pipelines," 1976.

[34] K. K. Botros, *et al.*, "Effects of pipe internal surface roughness on decompession wave speed in naatural gas mixtures," in *ASME Conference Proceedings*, 2010, pp. 907-922.

[35] Australian-Standard-1544.2, "Method for Impact tests on metals. Part2: Charpy V-notch," 2003.

[36] A. Cosham, *et al.*, "Not another Charpy V-Notch correction factor...?," presented at the 6th International Pipeline Technology Conference, Ostend, 2013.

[37] P. Thibaux and F. V. D. Abeele, "Determination of crack initiation and propagation energy in instrumented Charpy V-notch impact tests by finite element simulations," in *Pipeline Technology Conference*, Ostend, 2009.

[38] C. A. Folch and F. M. Burdekin, "Application of coupled brittle-ductile model to study correlation between Charpy energy and fracture toughness values," *Engineering Fracture mechanics*, vol. 63, pp. 57-80, 1999.

[39] F. Rivalin, *et al.*, "Ductile tearing of pipeline steel wide plates I. Dynamic and quasi-static experiments," *Engineering Fracture mechanics*, vol. 68, 2001.

[40] T. L. Anderson, *Fracture mechanics: Fundamentals and Applications*. FL: CRC Press, 2005.

[41] S. Cravero and C. Ruggieri, "Correlation of fracture behavior in high pressure pipelines with axial flaws using constraint designed test specimens-Part I: Plane-strain analyses," *Engineering Fracture mechanics*, vol. 72, pp. 1344-1360, 2005.

[42] DNV-OS-F101, "Offshore standard-submarine pipeline systems," ed. Norway: Det Norske Veritas, 2000.

[43] DNV-P-F108, "Fracture control for pipeline installation methods: Introducing cyclic plastic strain," ed. Norway: Det Norske Veritas, 2006.

[44] A. L. Gurson, "Continuum theory of ductile rupture by void nucleation and growth. Part I. Yeild croteria and flow rules for porous ductile media," *Journal of Engineering Materials and Technology,* pp. 2-15, 1997.

[45] V. Tveergaard, "Influence of voids on shear band instabilities under plane strain conditions," *Acta Materialia,* vol. 32, pp. 157-169, 1981.

[46] V. Tveergaard, "Analysis of the cup-cone fracture in a round tensile bar," *Acta Metallurgica,* vol. 32, pp. 157-169, 1984.

[47] B. Tanguy, Besson, J, Piques,R, & Pineau, A, "Ductile to brittle transition of an A508 steel characterized by Charpy impact test," *Engineering Fracture mechanics,* vol. 72, pp. 49-72, 2005.

[48] L. E. Schubert, *et al.*, "Effect of specimen size on the impact properties of neutron irradiated A533B steel," *Jounal of Nuclear Materials,* vol. 225, pp. 231-237, 1995.

[49] P. Thibaux, *et al.*, *Ductile facture characterization of an X70 steel: Re-interpretation of classical tests using the finite element technique*. Calgary, 2009.

[50] H. Baaser and D. Gross, "Crack analysis in ductile cylindrical sheels using Gurson's model," *International Journal of Solids and Structures,* vol. 37, pp. 7093-7104, 2000.

[51] J. Besson, *et al.*, "Modelling of crack growth in round bars and plane strain specimens," *International Journal of Solids and Structures,* vol. 37, pp. 8259-8284, 2001.

[52] Y. Chen and S. Lambert, "Analysis of ductile tearing of pipeline -steel in single edge notch tension specimens," *International Journal of Fracture,* vol. 124, pp. 179-199, 2003.

[53] K. Kofiani, *et al.*, "New calibration method for high and low triaxiality and validation on SENT specimens of API X70," *International Journal of Pressure Vessels and Piping,* vol. 111-112, pp. 187-201, 2013.

[54] C. K. Oh, *et al.*, "A phenomenological model of ductile fracture for API X65 steel," *International Journal of Mechanical Sciences,* vol. 49, pp. 1399-1412, 2007.

[55] Y. Chen and C. Ruggieri, "Structural integrity assessments of high pressure pipelines with axial flaws using a micromechanics model," *International Journal of Pressure Vessels and Piping,* vol. 81, pp. 761-770, 2004.

[56] N. Nourpanah and F. Taheri, "Ductile crack growth and constraint in pipeline subject to combined loadings," *Engineering Fracture mechanics,* vol. 78, pp. 2010-2018, 2011.

[57] A. G. Kostryzhev, *et al.*, "Detection of crack growth in rail steel using acoustic emission," *Ironmaking and Steelmaking,* pp. 1-6, 2012.

[58] M. Wevers, "Listening to the sound of materials: Acoustic emission for the analysis of material behaviour," *NDT and E International,* vol. 30, pp. 99-106, 1997.

[59] H. Vallen, *Acoustic Emission Testing Findamentals, Equipment, Applications,* 2004.

[60] H. L. Dunegan, "Factors affecting acoustic Emission Response from materials," *Acoustic emission, ASTM,* pp. 100-113, 1972.

[61] T. Ingham, *et al.*, "Acoustic emission characteristics of steels part 1: Acoustic measurements from tensile tests," *International Journal of Pressure Vessels and Piping,* vol. 2, pp. 31-50, 1974.

[62] B. Muravin, "Acosutic Emission Science and Technology," *Journal of Building and Infrastructure Engineering of the Isreali Association of engineering and Architects,* 2009.

[63] J. K. Burnett, Ed., *Theory and Uses of Acoustic Emissions* (Materials Science and Technologied. 2012, p.^pp. Pages.

[64] T. F. Drouillard, "A history of acoustic emission," *Journal of Acoustic Emission,* vol. 14, pp. 1-34, 1996.

[65] H. M. Tensi, "The Kaiser-Effect and its Scientific Background," in *26th European Conference on Acoustic Emission Tetsing*, Berlin, 2004, pp. 31-42.

[66] D. R. James and S. H. Carpender, "Relationship between acoustic emission and dislocation kinetics in crystalline solids," *Journal of Applied Physics,* vol. 42, pp. 4685-4697, 1971.

[67] F. Tonolini, *et al.*, "General review of developments in Acoustic Emission methods," *International Journal of Pressure Vessels and Piping*, vol. 28, pp. 179-201, 1987.

[68] S. Crutzen, *et al.*, "Developments in fracture mechanics and non-destructive examination," *Nuclear Engineering and Design*, vol. 134, pp. 59-86, 1992.

[69] R. Fernando, "Health Monitoring of FRP using acoustic emission and fibre optic techniques," 2004.

[70] A. Pollock, "Acoustic Emission Inspection," 1989.

[71] K. Ono, "Acoustic emission in materials research - a review," *J. Acoustic Emission*, vol. 29, pp. 284-308, 2011.

[72] M. R. Horne, "Rayleigh Wave Acoustic Emission during crack propagation in steel," 2003.

[73] A. A. Pollock, "Material brittleness and the energetics of acoustic emission," in *Society for Experimental Mechanics - SEM Annual Conference and Exposition on Experimental and Applied Mechanics 2010*, 2010, pp. 1082-1088.

[74] C. Hellier, *Handbook of Non-descructive Evaluation*. New York; London: McGraw-Hill, 2001.

[75] D. G. Eitzen and H. N. G. Wadley, "Acoustic emission: Establishing the fundamentals," *Journal of research of the national bureau of standards*, vol. 89, pp. 75-100, 1984.

[76] J. R. Frederick and D. K. Felbeck, "Dislocation motion as a source of acoustic emission," *Acoustic emission, ASTM*, pp. 129-139, 1972.

[77] S. H. Carpenter and F. P. Higgins, "Sources of acoustic emission generated during the plastic deformation of 7075 aluminum alloy," *Matellurgical Transactions A*, vol. 8, pp. 1629-1632, 1977.

[78] K. Barat, *et al.*, "Low tempearture tensile deformation and acoustic emission signal characteristics of AISI 304LN stainless steel," *Materials Science and Engineering A*, vol. 597, pp. 37-45, 2013.

[79] T. M. Roberts, "Acoustic emission monitoring of fatigue crack propagation," *Construction steel research*, vol. 59, pp. 695-712, 2003.

[80] A. Suman, *et al.*, "Amplification of acoustic emission signals during tensile deformation of aluminium," *Journal of Non Destructive Testing & Evaluation*, pp. 19-22, 2009.

[81] ASNT, *Nondestructive Testing Handbook: Acoustic Emission Testing*, Third edition ed. vol. 6: ASNT.

[82] Z. Kral, *et al.*, "Crack Propagation Analysis Using Acoustic Emission Sensors for Structural Health Monitoring Systems," *Scientific World Journal*, 2013.

[83] T. Chuluunbat, *et al.*, "Influence of Loading Conditions during Tensile Testing on Acoustic Emission," *Key Engineering Materials,* vol. 626, pp. 121-126, 2014.

[84] C. K. Mukhopadhyay, *et al.*, "The influence of notch on the acoustic emission generated during tensile testing of nuclear grade AISI type 304 stainless steel," *Materials Science and Engineering: A,* vol. 276, pp. 83-90, 2000.

[85] Z. Han, *et al.*, "Effects of strain rate and notch on acoustic emission during the tensile deformation of a discontinuous yielding material," *Materials Science and Engineering: A,* vol. 528, pp. 4372-4380, 2011.

[86] H. L. Dunegan, *et al.*, "Fracture analysis by use of acoustic emission," *Engineering Fracture Mechanics,* vol. 1, pp. 105-122, 1968.

[87] I. G. Palmer and P. T. Heald, "The application of acoustic emission measurements to fracture mechanics," *Materials Science and Engineering,* vol. 11, pp. 181-184, 1973.

[88] D. Dilipkumar and W. E. Wood, "Acoustic Emission analysis of fracture toughness tests," *Experimental Mechanics,* vol. 19, pp. 416-420, 1979.

[89] I. G. Palmer, *et al.*, "The relationship between acoustic emission and crack opening displacement measurements," *Materials Science and Engineering,* vol. 14, pp. 3-6, 1974.

[90] Y. Blanchette, *et al.*, "The use of acoustic emission to evaluate critical values of K and J in 7075-T651 aluminum alloy," *Engineering Fracture Mechanics,* vol. 20, pp. 359-371, 1984.

[91] Y. Blanchette and J. I. Dickson, "Acoustic emission behaviour during crack growth of 7075-T651 AI alloy," *Engineering Fracture mechanics,* vol. 24, pp. 647-656, 1986.

[92] M. V. Lysak, "Development of the theory of acoustic emission by propagating cracks in terms of fracture mechanics," *Engineering Fracture Mechanics,* vol. 55, pp. 443-452, 1996.

[93] C. K. Mukhopadhyay, *et al.*, "Study of tensile deformation behaviour of M250 grade maraging steel using acoustic emission," *Journal of Materials Science,* vol. 45, pp. 1371-1384, 2010.

[94] A. Fallahi, *et al.*, "Monitoring of the deformation and fracture process of dual phase steels employing acoustic emission techniques," *Materials Science and Engineering: A,* vol. 548, pp. 183-188, 2012.

[95] M. Ohtsu and K. Ono, "AE Source Location and Orientation Determination of Tensile Cracks from Surface Observation," *Ndt International,* vol. 21, pp. 143-150, Jun 1988.

[96] H. Roy, *et al.*, "Acoustic emissions during fracture toughness tests of steels exhibiting varying ductility," *Materials Science and Engineering: A,* vol. 486, pp. 562-571, 2008.

[97] H. N. G. Wadley, *et al.*, "Acoustic emission for physical examination of metals," *International Metals Reviews,* vol. 2, pp. 41-64, 1980.

[98] M. Kotoul and Z. BÃ-lek, "Acoustic emission during deformation and crack loading in structural steels," *International Journal of Pressure Vessels and Piping,* vol. 44, pp. 291-307, 1990.

[99] M. Lugo, *et al.*, "Quantification of damage evolution in a 7075 aluminum alloy using an acoustic emission technique," *Materials Science and Engineering: A,* vol. 528, pp. 6708-6714, 2011.

[100] G. Clark and J. F. Knott, "Acoustic emission and ductile crack growth in pressure-vessel steels," *Metal Science,* vol. 6, pp. 531-536, 1977.

[101] S. Mostafavi, *et al.*, "Acoustic emission methodology to evaluate the fracture toughness in heat treated AISI D2 tool steel," *Journal of Materials Engineering and Performance,* vol. 21, pp. 2103-2116, 2011.

[102] C. K. Mukhopadhyay, *et al.*, "Acoustic emission during fracture toughness tests of SA333 Gr.6 steel," *Engineering Fracture mechanics,* vol. 96, pp. 294-306, Dec 2012.

[103] M. F. M. Yusof, *et al.*, "Acoustic emission behavior during fatigue crack of API5LX70 gas pipeline steel," *Applied Mechanics and Materials,* vol. 80-81, pp. 148-152, 2011.

[104] B. Raj, *et al.*, "Frequency spectrum analysis of acoustic emission signal obtained during tensile deformation and fracture of an AISI 316 type stainless steel," *Acta metallurgica,* vol. 37, pp. 2211-2215, 1989.

[105] D. Huang, *et al.*, "Using Acoustic Emission in fatigue and Fracture materials Research (Overview)," *The Minerals, Metals & Materials Society,* vol. 50, pp. 1-13, 1998.

[106] B. Z. Weiss, *et al.*, "Static and Dynamic crack toughness of brazed joints of inconel 718 nickel-base alloy," *Welding research supplement,* vol. 10, pp. 287-295, 1979.

[107] S. I. Ochiai, *et al.*, "Acoustic emission detection of crack initiation during dynamic fracture testing of high strength materials," *Journal of Acoustic Emission,* vol. 2, pp. 289-291, 1983.

[108] H. Richter, *et al.*, "The use of acoustic emission to determine characteristic dynamic strength and toughness properties of steel," *Nuclear Engineering and Design,* vol. 188, pp. 241-254, 1999.

[109] T. A. Seiwert and M. P. Manahan, Eds., *Pendulum impact testing: A century of progress* (Use of Instrumented Charpy Test for Determination of Crack Initiation Toughness. Pennsylvania: Baltimore, MD, 2000, p.^pp. Pages.

[110] J. P. Tronskar, *et al.*, "Application of acoustic emission for measuring crack initiation toughness in instrumented Charpy impact testing," *Journal of Testing and Evaluation,* vol. 31, pp. 222-233, May 2003.

[111] A. Mostafapour and S. Davoudi, "Analysis of leakege in high pressure pipe using acoustic emission methods," *Applied Acoustics,* vol. 74, pp. 335-342, 2013.

[112] G. Giunta, *et al.*, "Fracture mechanisms evaluation in gas transporataion pipes by acouctic emission analysis," 2011.

[113] M. W. Drew, *et al.*, "Acoustic emission during the deformation and crack initiation of pipeline steels," *Journal of Acoustic Emission,* vol. 6, pp. 239-248, 1987.

[114] T. Ohiro and Y. H. Pao, "Microcrack initiation and acoustic emission during fracture toughness tests of A533B steel," *Metallurgical transactions A,* vol. 17A, pp. 843-852, 1986.

[115] S. Budano, *et al.* Acoustic Emission data analysis to evaluate damage mechanisms in pipeline carbon steels [Online].

[116] S. Budano, *et al.* Damage mechanism evaluation in pipeline steels using acoustic emission analysis [Online].

[117] T. Ingham, *et al.*, "Acoustic emission characteristics from steels Part 2: Acoustic measurements from fracture toughness tests," *International Journal of Pressure Vessels and Piping,* vol. 3, pp. 267-293, 1975.

[118] E. Ostby, *et al.*, "Quantitative relation between acoustic emission signal amplitude and arrested cleavage microcrack size," *International journal of fracture,* vol. 177, pp. 73-80, 2012.

[119] J. Capelle, *et al.*, "The effect of hydrogen concentration on fracture of pipeline steels in presence of a notch," *Engineering Fracture mechanics,* vol. 78, pp. 364-373, 2011.

[120] D. M. Almeida, *et al.*, "Characterization of steel pipeline damage using acoustic emission technique," *Soldagem & Inspecao,* vol. 12, pp. 55-62, Jan-Mar 2007.

[121] Australian-Standard, "AS-1391-2007," in *Metallic material-tensile testing at ambient temperature*, ed.

[122] Mistras-PAC, "USB-AE Node & AE win for USB Software User's Manual 1283-1000," 2012.

[123] Dantec-Dynamics, "Manual for Digital Image Correlation System," 2014.

[124] JEOL, "User's guide for JSM-6490 Scanning Electron Microscope," 2011.

[125] LSTC, *LS-DYNA keyword user's manual (updated manually)*, 2013.

[126] T. Chuluunbat, *et al.*, "Investigation of API-X70 line pipe steel fracture during single edge-nothced tensile testing using acoustic emission monitoring," *Materials Sceince and Engineering A*, vol. 640, pp. 471-479, 2015.

[127] R. Khamedi, *et al.*, "The influence of morphology and volume fraction of martensite on AE signals during tensile loading of dual-phase steels," *International journal of recent trends in Engineering*, vol. 1, pp. 30-34, 2009.

[128] A. Venkert, *et al.*, "Effect of loading rate on fracture morphology in high strength ductile steel," *Journal of Engineering Materials and Technology*, vol. 123, pp. 261-267, 2001.

[129] M. Akbari and M. Ahmadi, "The application of acoustic emission technique to plastic deformation of low carbon steel," *Physics Procedia*, vol. 3, pp. 795-801, 2010.

[130] A. Otsuka, *et al.*, "Relationship between ductile crack initiation and void volume fraction," *Nuclear Engineering and Design*, vol. 105, pp. 121-129, 1986.

List of Publications

1) T. Chuluunbat, C. Lu, A.K. Kostryzhev and K.Tieu, "Influence of Loading Conditions during Tensile Testing on Acoustic Emission," *Key Engineering Materials*, vol. 626, pp. 121-126, 2014.

2) T. Chuluunbat, C. Lu, A.K. Kostryzhev and K.Tieu "Investigation of API-X70 line pipe steel fracture during single edge-nothced tensile testing using acoustic emission monitoring" *Materials Sceince and Engineering A*, vol.640, pp.471-479, 2015.

3) T. Chuluunbat, C. Lu, A.K. Kostryzhev and K.Tieu, "Influence of Loading Conditions during Tensile Testing using Acoustic Emission monitoring," *12thAEPA conference, Taiwan,* September, 2014.

4) T. Chuluunbat, C. Lu, A.K. Kostryzhev and K.Tieu "Fracture behavoiur of line pipe steel during Charpy V-Notch impact testing: Acoustic emission technique and FEM simulation" *Engineering Fracture Mechanics*, 2015 (submitted to the journal under revision).